

Title goes here

Bálint Balázs



Pázmány Péter Catholic University
Faculty of Information Technology



European Molecular Biology Laboratory

Supervisors: Lars Hufnagel, *PhD*, Balázs Rózsa, *MD, PhD*

A thesis submitted for the degree of
Doctor of Philosophy
2017

Abstract

Abstract in English.

Tartalmi kivonat

Absztrakt magyarul.

Contents

Abstract	iii
Tartalmi kivonat	v
List of Figures	x
List of Tables	xi
Introduction	1
1 Live imaging in three dimensions	3
1.1 Wide-field fluorescence microscopy	4
1.2 Point scanning methods	10
1.3 Light-sheet microscopy	14
1.4 Light-sheet microscopy for mouse imaging	22
2 Dual Mouse-SPIM	29
2.1 Microscope design principles	29
2.2 Optical layout	33
2.3 Optical alignment	39
2.4 Control unit	43
2.5 Results	45
2.6 Methods	51
3 Image processing for multi-view microscopy	55
3.1 Multi-view image fusion	56
3.2 Image compression	56
3.3 Noise in light microscopy images	66
4 Real-time, GPU accelerated image processing pipeline	67
4.1 GPU architecture	67
4.2 Live fusion	67

CONTENTS

4.3 B ³ D image compression	67
4.4 Noise dependent lossy compression	68
4.5 Methods	68
5 Discussion	77
5.1 New scientific results	77
Acknowledgements	79
Appendix A Bill of materials	81
Appendix B Appendix B	83
References	87

List of Figures

1.1	Tradeoffs in fluorescence microscopy for live imaging	4
1.2	Excitation and emission spectrum of enhanced green fluorescent protein (EGFP)	5
1.3	Wide-field fluorescence microscope	6
1.4	Axial cross section of the PSF and OTF of a wide-field microscope	8
1.5	Airy pattern	9
1.6	Resolution of a wide-field microscope	11
1.7	Basic optical components of a confocal laser scanning and confocal-theta microscope	13
1.8	Axial cross section of the PSF and OTF of a confocal laser scanning microscope	14
1.9	Basic concept of single-plane illumination microscopy	15
1.10	Different optical arrangements for light-sheet microscopy	16
1.11	Basic optical components of a SPIM	18
1.12	Light-sheet dimensions	19
1.13	DSLM illumination	21
1.14	Inverted light-sheet microscope for multiple early mouse embryo imaging.	24
1.15	Imaging mouse post-implantation development	25
1.16	Imaging adult mouse brain with light-sheet microscopy.	27
2.1	Light collection efficiency of an objective	31
2.2	Lateral and axial resolution of a multi-view optical system.	32
2.3	Dual view concept with high NA objectives	33
2.4	The core unit of the microscope	34
2.5	Dual Mouse SPIM optical layout	36
2.6	Illumination branch splitting unit	37
2.7	Detection branch switching unit	39
2.8	Microscope control hardware and software architecture	44
2.9	Digital and analog control signals	44

LIST OF FIGURES

2.10 Completed DualMouse-SPIM	46
2.11 Stability measurements of view switcher unit	47
2.12 Illumination beam profile	48
2.13 Simulated and measured PSF of Dual Mouse-SPIM	49
2.14 Combined PSF of 2 views	50
2.15 Maximum intensity projection of a <i>Drosophila melanogaster</i> embryo recording	51
2.16 Multi-view recording of a mouse zygote	52
3.1 Building the binary Huffman tree	59
3.2 Arithmetic coding scheme in practice with the alphabet from Table 3.4 on the sequence a_1, a_2, a_3	61
3.3 Basis functions of the 8×8 2D DCT, computed as the outer product of the 1D basis vectors.	63
3.4 Multi-resolution wavelet decomposition, using the Haar wavelets as an example	65
4.1 Experiment sizes and data rate of different imaging modalities	68
4.2 B ³ D algorithm schematics	69
4.3 Lossless compression performance	70
4.4 Options for noise dependent lossy compression	71
4.5 Within noise level compression performance	72
4.6 Image quality of a WNL compressed dataset	72
4.7 Compression error compared to image noise	73
4.8 Influence of noise dependent lossy compression on 3D nucleus segmentation	73
4.9 Influence of noise dependent lossy compression on 3D membrane segmentation	74
4.10 Influence of noise dependent lossy compression on single-molecule localization	74
4.11 Change in localization error only depends on selected quantization step .	75

List of Tables

3.1	Examples of a random binary code (#1) and a prefix-free binary code (#2)	58
3.2	Huffman code table	59
3.3	Huffman code table	60
3.4	Example alphabet for arithmetic coding	61
B1	Data sizes in microscopy	84
B2	Lossless compression performance	84
B3	Datasets used for benchmarking compression performance	85

LIST OF TABLES

Introduction

Coming soon.

INTRODUCTION

Chapter 1

Live imaging in three dimensions

Unraveling the secrets of mammalian development has been a long standing challenge for developmental biologists and medical professionals alike. This phase of early life is an incredibly complex and dynamic process spanning through large scales in space and time. Subcellular processes at the nanoscale are happening in the range of milliseconds or faster, while whole embryo reorganizations and tissue migration events take place over the course of hours [1]. Resolving these processes presents a true challenge, since to understand the underlying mechanisms, molecular specificity is just as crucial as high spatial and temporal resolution.

Light microscopy is one of the oldest methods that is still widely used today to investigate the inner workings of microscopic life. A particularly important branch is fluorescence microscopy [2], that relies on using fluorescent labels to mark specific regions inside the specimens. Light-sheet microscopy is a relatively new addition to the arsenal of tools that comprise light microscopy methods, and is especially suitable for live imaging of embryonic samples over extended periods of time [3–6]. It is also easily adapted to the sample, allowing to image a large variety of specimens, from entire organs, such as cleared mouse brains [7], to the subcellular processes occurring inside cultured cells [8].

In an ideal setting, the ultimate microscope would be able to record a continuous, 3D, and multicolor dataset of any biological process of interest with the highest possible resolution. Unfortunately this is not possible; due to several limitations in physics and biology, a compromise is necessary. The diffractive nature of light, the lifetime of fluorescent probes and the photosensitivity of biological specimens all require microscopy to be able to adapt to answer the question at hand. In order to acquire useful data one has to choose a tradeoff between spatial and temporal resolution, and signal contrast, while making sure the biology is not affected by the imaging process itself (Fig. 1.1) [9].

1. LIVE IMAGING IN THREE DIMENSIONS

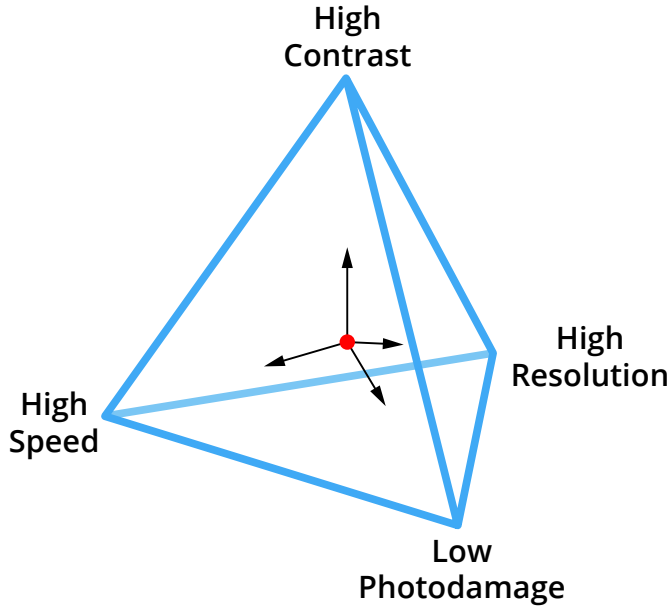


Figure 1.1: Tradeoffs in fluorescence microscopy for live imaging. Also called the “pyramid of frustration”. When optimizing the imaging conditions (red dot), a tradeoff has to be made between resolution, contrast, and imaging speed, while avoiding photodamage. One can only be improved at the expense of the others due to the limited photon budget of the fluorescent molecules. Adapted from [9].

1.1 Wide-field fluorescence microscopy

Fluorescence microscopy [2, 10], as a subset of light microscopy is one of the few methods that allows subcellular imaging of live specimens. The first use of the term fluorescence is credited to George Gabriel Stokes [11], and it refers to the phenomenon when a molecule emits light after absorbing light or other electromagnetic radiation. As the name of the technique suggests, this method collects fluorescent light from the specimens which has numerous advantages, but also some drawbacks. Since biological tissue is usually not fluorescent, except for some autofluorescence at shorter wavelengths, fluorescent dyes or proteins have to be introduced to the system in order to be able to collect the necessary information. The advantage of this is that the signal of the labeled structures will be of very high ratio compared to the background.

A fluorescent molecule is capable of absorbing photons in a given range (excitation spectrum) and temporarily store its energy by having an electron in a higher energy orbital, *i.e.* in an excited state. This excited state, however is not stable, and the electron quickly jumps back to the ground state while emitting a photon with equal energy to the energy difference between the excited and ground states. The energy of the absorbed and emitted photons are not the same, as energy loss occurs due to internal relaxation events, and the emitted photon has lower energy than the absorbed photon. This phenomenon is called the Stokes shift, or red shift, and can be exploited in microscopy to drastically increase the signal to noise ratio by filtering out the illumination light (Fig. 1.2).



Figure 1.2: Excitation and emission spectrum of enhanced green fluorescent protein (EGFP). Excitation spectrum in blue, emission spectrum in yellow. The separation between the two spectra is due to the Stokes shift, which is 19 nm for EGFP. Emitted and excitation light can be separated by a long-pass filter at 500 nm. Data from [12].

1.1.1 Fluorescent proteins

Traditionally synthetic fluorescent dyes were used to label certain structures in the specimens. Some of these directly bind to their target, and others can be used when conjugated to an antibody specific to the structure of interest. The drawback of these methods is that the fluorescent label has to be added to the sample from an external source, and, in many cases, this also necessitates sample preparation techniques incompatible with live imaging, such as fixation [13].

The discovery of fluorescent proteins have revolutionized fluorescence microscopy. Since these molecules are proteins, they can be produced directly by the organism if the proper genetic modifications are performed. Even though this was a hurdle at the time of discovering the green fluorescent protein (GFP) [14], the first of its kind, genetic engineering techniques evolved since then [15], and not only has it been successfully integrated in the genome of nematodes [16], zebrafish [17], and mice [18], but many variants have been also engineered by introducing mutations to increase fluorescence intensity, and to change the fluorescence spectrum to allow multicolor imaging [18–21]. The usefulness and impact of these proteins are so profound, that in 2008 the Nobel Prize in chemistry was awarded to Osamu Shimomura, Martin Chalfie, and Roger Tsien “for the discovery and development of the green fluorescent protein, GFP” [22].

1.1.2 Wide-field image formation

By imaging fluorescently labelled specimens, a wide-field fluorescence microscope has the capability of discriminating illumination light from fluorescent emitted light due to the Stokes shift described in the previous section. The microscope’s operating principle is

1. LIVE IMAGING IN THREE DIMENSIONS

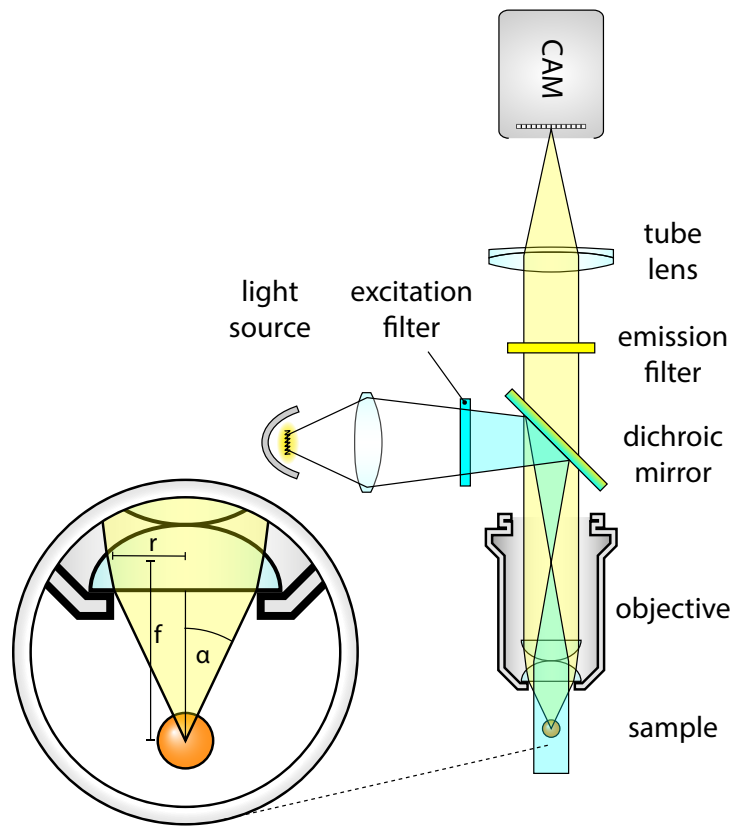


Figure 1.3: Wide-field fluorescence microscope. (a) The light source is focused on the back focal plane of the objective to provide an even illumination to the sample. Emitted photons are collected by the objective, and are separated from the illumination light by a dichroic mirror. (b), α

depicted in Figure 1.3.

A light source, typically a mercury lamp is focused on the back focal plane of the objective to create even illumination at the sample. Before entering the objective, the light is filtered, so only the wavelengths that correspond to the excitation properties of the observed fluorophores are transmitted. Since the same objective is used for both illumination and detection, a dichroic mirror is utilized to decouple the illumination and detection paths. The emitted light is filtered again to make sure any reflected and scattered light from the illumination source is blocked to increase signal to noise ratio.

Finally, the light is focused by a tube lens to create a magnified image in the camera sensor. This type of imaging is called infinity corrected optics, since the back focal point of the objective is in “infinity”, meaning that the light exiting the back aperture is parallel. This is achieved by placing the sample exactly at the focal point of the objective. Infinity corrected optics has the advantage that it allows placing various additional optical elements in the infinity space (*i.e.* the space between the objective and the tube lens) without affecting the image quality. In this example such elements are the dichroic mirror and the emission filter.

The combination of the objective and tube lens together will determine the magnification of the system, it will be the ratio of the focal lengths of these lenses:

$$M = \frac{f_{TL}}{f_{OBJ}}. \quad (1.1)$$

The final field of view (FOV) of the microscope will depend on the magnification, and also on the size of the imaging sensor:

$$FOV = \frac{A}{M}, \quad (1.2)$$

where A is the area of the sensor.

Apart from magnification, the most important property of the objective is the half-angle of the light acceptance cone, α . This not only determines the amount of collected light, but also the achievable resolution of the system (see next section). This angle depends on the size of the lens relative to its focal length. In other words depends on the aperture of the lens, which is why the expression *numerical aperture* (NA) is more commonly used to express this property of the objective:

$$NA = n \cdot \sin \alpha. \quad (1.3)$$

For small α angles, the following approximation holds true: $\sin \alpha \approx \tan \alpha \approx \alpha$. Thus, the numerical aperture can also be expressed as a ratio of the radius of the lens and the focal length:

$$NA \approx n \frac{r}{f}, \quad \text{when } \alpha \ll 1. \quad (1.4)$$

1.1.3 Resolution of a wide-field microscope

The resolution of an optical systems is defined by the size of the smallest distinguishable feature on the image. Practically this means the minimum distance between two point-like objects so that the two objects can still be resolved. This mainly depends on two factors: the NA of the objective, and the pixel size of the imaging sensor.

Even if the imaging sensor would have infinitely fine resolution, it is not possible to reach arbitrary high resolutions due to the wave nature of light and diffraction effects that occur at the aperture of the objective. This means that depending on the wavelength of the light, any point source will have a finite size on the image, it will be spread out, that will limit the resolution. The shape of this image is called the *point spread function*, or PSF (Fig. 1.4), as this function describes the behavior of the optical system when imaging a point like source. This property of lenses was already discovered by Abbe in

1. LIVE IMAGING IN THREE DIMENSIONS



Figure 1.4: Axial cross section of the PSF and OTF of a wide-field microscope. Simulated PSF and OTF for a wide-field microscope with a water immersion objective ($n = 1.33$). $NA = 1.1$, $\lambda = 510\text{ nm}$

1873 [23], when he constructed his famous formula for resolution:

$$\delta = \frac{\lambda}{2 \cdot NA}. \quad (1.5)$$

where d is the smallest distance between two distinguishable features.

Another representation of the optical performance, is the *optical transfer function*, or OTF (Fig. 1.4), which is the Fourier transform of the PSF:

$$\text{OTF} = F(\text{PSF}). \quad (1.6)$$

As this function operates in the frequency space, it describes how the different frequencies are affected by the system. The resolution can also be defined as the support of the OTF, since this describes the highest frequency that is still transmitted through the optical system. Any pattern with higher frequency will be lost, thus beyond the resolution limit. For circularly symmetric PSFs, the OTF will be real valued, however if this is not the case, the Fourier transform also introduces complex components.

Abbe's formula can be derived from the scalar theory of diffraction using a paraxial approximation (Fraunhofer diffraction, [24]) that describes the intensity of the electric field in the focus of a lens [25]:

$$H(u, v) = C_0 \left| \int_0^1 J_0(vr) e^{-i\frac{1}{2} \cdot ur^2} r dr \right|^2, \quad (1.7)$$

where C_0 is a normalization constant, and J_0 is the zero order Bessel function of the first kind. Furthermore, instead of the commonly used Cartesian coordinates x , y and z , the



Figure 1.5: Airy pattern. Airy pattern calculated in Matlab based on Eq. 1.9

following optical coordinates are defined:

$$v = \frac{2\pi nr}{\lambda_0} \sin \alpha, \quad u = \frac{8\pi nz}{\lambda_0} \sin^2 \frac{\alpha}{2} \quad (1.8)$$

where $r = \sqrt{x^2 + y^2}$ is the distance from the optical axis, and α is the light collection angle as shown on Fig. 1.3.

To determine the lateral resolution of the system, let's substitute $u = 0$ as the axial optical coordinate, and evaluate Eq. 1.7 which will give the intensity distribution in the focal plane:

$$H(0, v) = C_0 \left| \int_0^1 J_0(vr) r dr \right|^2 = \left(2 \frac{J_1(v)}{v} \right)^2, \quad (1.9)$$

where J_1 is the first order Bessel function of the first kind. This equation describes the famous Airy pattern (Fig. 1.5) which will be the shape of the PSF in the focal plane. The width of this pattern is the resolution, and although there are multiple definitions for this, the most commonly accepted is the Rayleigh criterion [24, 26] which defines the resolution as the distance between the central peak and the first local minimum. As this lies at $v = 3.83$, the resolution can be expressed by substituting this value to Eq. 1.8 and calculating the real distance (r):

$$\delta_{xy} = \frac{3.83}{2\pi} \frac{\lambda_0}{n \cdot \sin \alpha} \approx 0.61 \frac{\lambda_0}{NA}, \quad (1.10)$$

which is equivalent to Abbe's original formula (Eq. 1.5). The only difference is the scaling factor which is due to the slightly different interpretations of width of the Airy disk as mentioned earlier.

1. LIVE IMAGING IN THREE DIMENSIONS

Similarly, to calculate the intensity distribution along the axial direction, let's substitute $v = 0$ to Eq. 1.7:

$$H(u, 0) = C_0 \left(\frac{\sin \frac{u}{4}}{\frac{u}{4}} \right)^2. \quad (1.11)$$

For this expression the first minimum lies at $u = 4\pi$. Converting back to Cartesian coordinates, the axial resolution can be expressed as:

$$\delta_z = \frac{2n\lambda_0}{NA^2}. \quad (1.12)$$

So far we only considered a single, point-like emitter. As the intensity function describes how an optical system “spreads out” the image of a point, it is also called the Point Spread Function (PSF, Fig. 1.4). In a more realistic scenario, however the emitters are neither point-like, nor single. Effectively, however, for every emitter the PSF would be imaged on the sensor, and this creates the final image. In mathematical terms, this can be expressed as a convolution operation between the underlying fluorophore distribution of the object (O) and the PSF (H):

$$I(u, v) = O(u, v) * H(u, v). \quad (1.13)$$

The effective result of this kind of diffraction limited image formation is a blurred image with a finite resolution of δ_{xy} in the lateral direction, and δ_z in the axial direction.

The PSF is further affected by the illumination pattern as well. Since the number of emitted fluorescent photons are roughly proportional to the illumination intensity, if the illumination has any structure at the order of the detection resolution, it will have an effect on the overall PSF of the system, which can be expressed as:

$$H_{sys} = H_{ill} \cdot H_{det}, \quad (1.14)$$

where H_{ill} is the point spread function of the illumination, and H_{det} is the point spread function of the detection.

1.2 Point scanning methods

In most cases, a wide-field microscope is used to image a section of a tissue, thus axial resolution is not a concern. Imaging live specimens, however is not so straightforward, as these samples are usually much thicker than a typical section. For these samples 3-dimensional (3D) imaging is highly beneficial, which necessitates some kind of optical sectioning technique to be able to discriminate the features at different depths.

Due to the design of the wide-field microscope, any photons emitted from outside the focal plane will also be detected by the sensor, however as these are not originating from

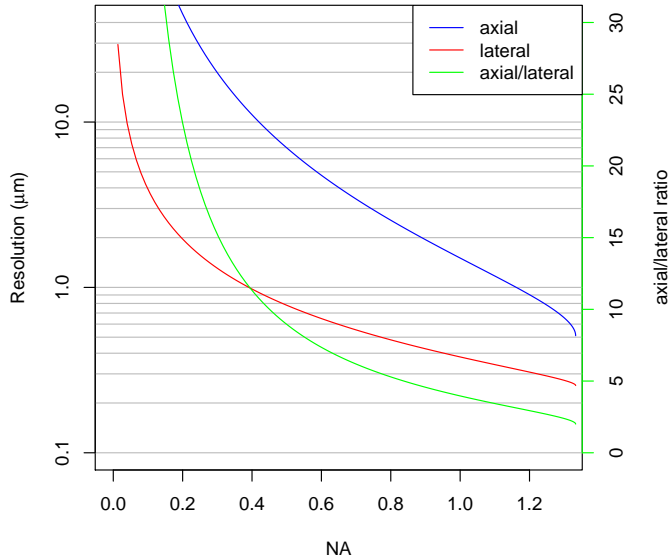


Figure 1.6: Resolution of a wide-field microscope. Axial (blue) and lateral (red) resolutions of a wide-field microscope are shown with respect to the numerical aperture (NA). Resolutions are calculated with $\lambda = 510\text{nm}$, the emission maximum of GFP and $n = 1.33$, the refractive index of water, for water dipping objectives.

the focus, only a blur will be visible. This blur potentially degrades image quality and signal-to-noise ratio to such extent that makes imaging thick sample very difficult if not impossible in a wide-field microscope.

Evaluating Equations 1.10 and 1.12 for a range of possible numerical apertures reveals the significant differences in lateral and axial resolution for any objective (Fig. 1.6). Especially for low NAs, this can be significant, a factor of ~ 20 difference. For higher (>0.8) NAs the axial resolution increases faster than the lateral, however they will only be equal when $\alpha = 180^\circ$. This means that isotropic resolution with a single lens is only possible if the lens is collecting all light emitting from the sample, which seems hardly possible, and would be highly impractical. For commonly used high NA objectives the lateral to axial ratio will still be around 3–6.

Instead of using a single lens to achieve isotropic resolution, it is more practical to image the sample from multiple directions to complement the missing information from different views. When rotating the sample 90° for example, the lateral direction of the second view will correspond to the axial direction of the first view. If rotation is not possible, using multiple objectives can also achieve similar result, such as in the case of Multi-Imaging Axis Microscopy (MIAM) [27, 28]. This microscope consisted of 4 identical objectives arranged in a tetrahedral fashion to collect as much light as possible from multiple directions, and provide isotropic 3D resolution, albeit at the expense of

1. LIVE IMAGING IN THREE DIMENSIONS

extremely difficult sample handling, since the sample was completely surrounded by objectives from all directions.

1.2.1 Confocal laser scanning microscopy

Confocal laser scanning microscopy (CLSM) [29, 30] addresses most of the problems of wide-field microscopy we mentioned in the previous section. It is capable of optical sectioning by rejecting out of focus light, which makes it a true 3D imaging technique. Furthermore, the light rejection also massively reduces out of focus background, and increases contrast.

This is achieved by two significant modifications compared to the wide-field optical path. To be able to reject the out of focus light, an adjustable pinhole is placed at the focus of the tube lens. Light rays originating from the focal point will meet at this position, and are able to pass through the pinhole, however out-of-focus light will converge either before or after the aperture, and thus the aperture blocks these rays. To maximize the fluorescence readout efficiency for the single focal point, a photomultiplier tube is used instead of an area sensor (Fig. 1.7a).

To maximize the signal from the focal point, the illumination light is also focused here by coupling an expanded laser beam through the back aperture of the objective. This not only increases illumination efficiency (since other, not detected points are not illuminated), but has the added benefit of increasing the resolution as well. This is due to the combined effect of illumination and detection PSFs as described in Eq. 1.14 (Fig. 1.8). For Gaussian-like PSFs, the final resolution (along a single direction) can be calculated in the following way:

$$\frac{1}{\delta_{sys}^2} = \frac{1}{\delta_{ill}^2} + \frac{1}{\delta_{det}^2}, \quad (1.15)$$

where δ_{ill} and δ_{det} are the resolutions for the illumination and detection, respectively. Since the same objective is used for both illumination and detection, and the difference in wavelength is almost negligible, $\delta_{ill} = \delta_{det} = \delta$, the final system resolution will be:

$$\delta_{sys} = \frac{1}{\sqrt{2}}\delta. \quad (1.16)$$

This means that the distinguishable features in a confocal microscope are ~ 0.7 times smaller than in a wide-field microscope using the same objective.

Because of the different detection method in a confocal microscope, direct image formation on an area sensor is not possible, since at any given time, only a single point is interrogated in the sample. Instead, it is necessary to move the illumination and detection point in synchrony (or in a simpler, albeit slower solution, to move the sample) to scan the entire field of view. The image can be later computationally reconstructed by a



Figure 1.7: Basic optical components of a confocal laser scanning and confocal-theta microscope. Both type of microscopes use confocal images detection, which means that a pinhole is used to exclude light coming from out of focus points. Light intensity is measured by a photomultiplier for every voxel in the region of interest. The final image is generated on a computer using the positions and recorded intensity values. A regular confocal microscope (1.7a) uses the same objective for illumination and detection, while a confocal-theta microscope (1.7b) uses a second objective that is rotated by ϑ around the focus. In this case, $\vartheta = 90^\circ$.

computer program that records the fluorescence intensity of every point of the field of view, and displays these values as a raster image.

1.2.2 Confocal-theta microscopy

Although confocal microscopy already has 3D capabilities, its axial resolution is still limited compared to the lateral, since it uses only one objective. An alternative realization of the confocal microscope, the confocal theta microscope [31] introduces a second objective to the system, that is used to illuminate the sample (Fig. 1.7b). Since this decouples the illumination and detection, using a filter cube is no longer necessary. The second objective is rotated by θ around the focus, this is where the name of this setup originates from.

As in the case of standard confocal microscopy, the system PSF is improved by the illumination pattern. Here, however, the axial direction of the detection coincides with the lateral direction of the illumination, which results in a dramatic improvement of

1. LIVE IMAGING IN THREE DIMENSIONS

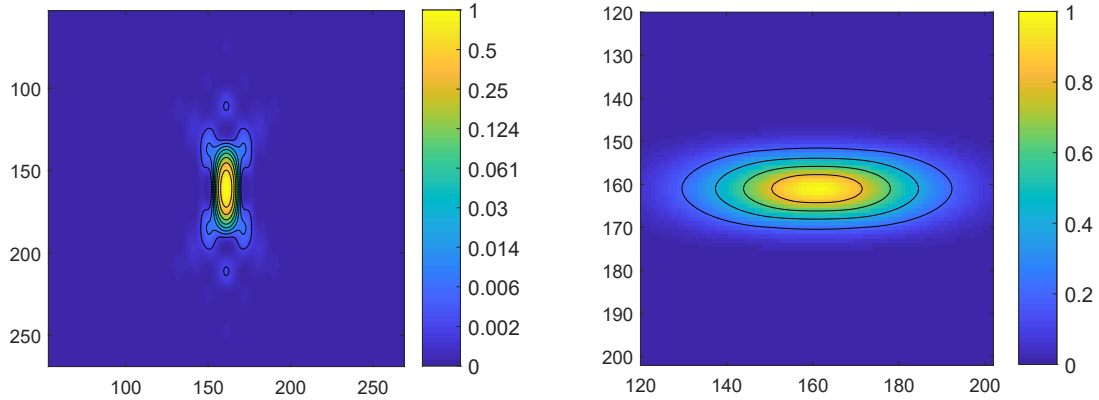


Figure 1.8: Axial cross section of the PSF and OTF of a confocal laser scanning microscope. Simulated PSF and OTF for a laser scanning confocal microscope with a water immersion objective ($n = 1.33$). $NA = 1.1$, $\lambda = 510\text{ nm}$

axial resolution compared to standard confocal microscopy. Lateral resolution will also be increased, but by a smaller extent, resulting in an almost isotropic PSF, and equal axial and lateral resolutions (Fig. ??).

Although this is a big improvement to confocal microscopy in terms of resolution, this technique did not reach a widespread adoption as it complicates sample handling, while still suffering from two big drawbacks of confocal microscopy techniques that limits its live imaging capabilities.

Imaging live specimens for an extended period of time with confocal microscopy although possible [32, 33], is not ideal. For each voxel imaged, a large portion of the specimen has to be illuminated, which results in a very high dose of radiation on the samples. This can be as much as 30–100 times larger, than the dose used for the actual imaging [34]. Illumination with high power of laser for an extended time frame can result in bleaching the fluorophores, which in turn will lower the signal at later times. Furthermore, any absorbed photon has the possibility to disrupt the chemical bonds inside the specimen, which can lead to phototoxic effects. Moreover, the usage of the pinhole although increases resolution, also decreases the detectable signal intensity, thus has a negative impact on image contrast [35].

1.3 Light-sheet microscopy

A selective-plane illumination microscope (SPIM) uses a light-sheet to illuminate only a thin section of the sample (Fig. 1.9). This illumination plane is perpendicular to the imaging axis of the detection objective and coincides with the focal plane. This way, only the section in focus will be illuminated, thus providing much better signal to noise ratio.

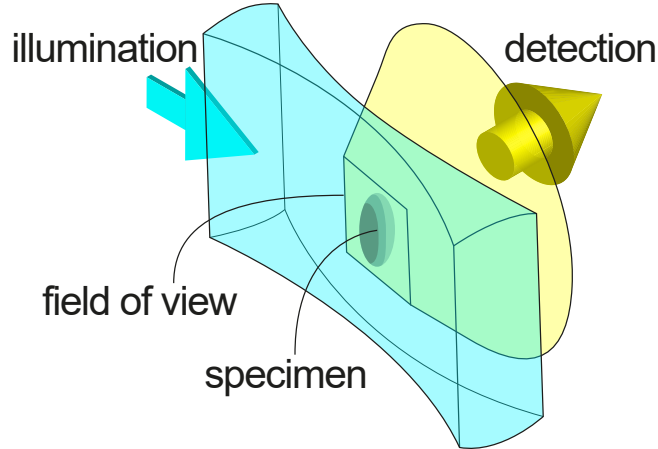


Figure 1.9: Basic concept of single-plane illumination microscopy. The sample is illuminated from the side by laser light shaped to a light-sheet (blue). This illuminates the focal plane of the detection lens, that collects light in a wide-field mode (yellow). The image is recorded, and the sample is translated through the light-sheet to acquire an entire 3D stack.

In case of conventional wide-field fluorescence microscopy, where the whole specimen is illuminated, light scattering from different regions contributes to a significant background noise. With selective-plane illumination, this problem is intrinsically solved, and it also provides a true sectioning capability. This makes SPIM especially suitable for 3D imaging.

The main principle behind single plane illumination microscopy, that is illuminating the sample from the side by a very thin light-sheet, dates back to the early 20th century, when Siedentopf and Zsigmondy first described the ultramicroscope [36]. This microscope used sunlight as an illumination source, that was guided through a precision slit to generate a thin light-sheet. This allowed Zsigmondy to visualize gold nanoparticles floating in and out of the light-sheet. Since these particles are much smaller than the wavelength of the light, the device was called an ultramicroscope. His studies with colloids, and the development of the ultramicroscope led Zsigmondy to win the Nobel Prize in 1925.

After Zsigmondy, this method was forgotten until rediscovered in the 1990s, when Voie *et al.* constructed their Orthogonal-plane Fluorescent Optical Sectioning (OPFOS) microscope [37]. They used it to image a fixed, optically cleared and fluorescently labelled guinea pig cochlea. In order to acquire a 3D dataset, the sample was illuminated from the side with a light-sheet generated by a cylindrical lens, then rotated around the center axis to obtain multiple views. Although they only reached a lateral resolution around 10 µm and axial resolution of 26 µm, this method allowed them to generate a 3D reconstruction of the cochlea [38].

Later, in 2002, Fuchs et al. developed Thin Light-Sheet Microscopy (TLSM) [39] and used this technique to investigate the microbial life in seawater samples without disturbing their natural environment (by e.g. placing them on a coverslip). Their light-

1. LIVE IMAGING IN THREE DIMENSIONS

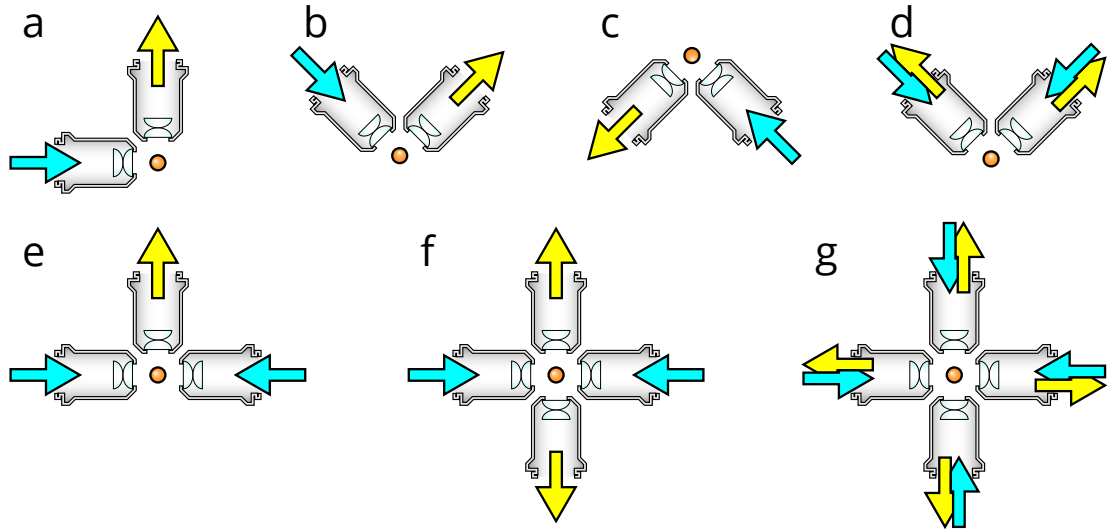


Figure 1.10: Different optical arrangements for light-sheet microscopy. (a) Original SPIM design with a single lens for detection and illumination. [40] (b) Upright SPIM to allow for easier sample mounting such as using a petri dish (iSPIM, [41, 42, J1]). (c) Inverted SPIM, where the objectives are below the sample, which is held by a thin foil [J2]. (d) Dual-view version of the upright configuration, where both objective can be used for illumination and detection (disSPIM, [43]). (e) Multidirectional-SPIM (mSPIM) for even illumination of the sample with two objectives for illumination [44]. (f) Multi-view SPIM with two illumination and detection objectives for *in toto* imaging of whole embryos (MuVi-SPIM [45], SimView [46], Four-lens SPIM [47]). (g) A combination of (d) and (f), using four identical objectives, where both can illuminate and detect in a sequential manner, to achieve isotropic resolution without sample rotation (IsoView [48]).

sheet was similar to the one utilized in OPFOS, being $23\text{ }\mu\text{m}$ thin, and providing a $1\text{ mm} \times 1\text{ mm}$ field of view.

Despite these early efforts, the method did not gain larger momentum. The real breakthrough in light-sheet imaging happened at EMBL in 2004, where Huisken *et al.* [40] combined the advantages of endogenous fluorescent proteins and the optical sectioning capability of light-sheet illumination to image Medaka fish embryos, and the complete embryonic development of a *Drosophila melanogaster* embryo. They called this Selective-Plane Illumination Microscopy (SPIM), and it quickly became popular to investigate developmental biological questions.

Since then, light-sheet based imaging has gained more and more popularity, as it can be adapted and applied to a wide variety of problems. Although sample mounting can be challenging because of the objective arrangement, this can also be an advantage, since new microscopes can be designed with the sample in mind [4, J3] (Fig. 1.10). This made it possible to adapt the technique for numerous other specimens, such as zebrafish larvae [49], *C. elegans* embryos [42], mouse brain [7], and even mouse embryos [J2, 50, 51].

As many of these specimens require very different conditions and mounting techniques, these microscopes have been adapted to best accommodate them. An upright objective arrangement for example (Fig 1.10b) allows imaging samples on a coverslip,

while its inverted version is well suited for mouse embryos, where a foil is separating them from the immersion medium (Fig. 1.10c). A modified version of the upright arrangement allows for multi-view imaging using both objectives for illumination and detection in a sequential manner (Fig. 1.10d) [52].

For larger samples, to achieve a more even illumination, two objectives can be used from opposing directions to generate two light-sheets (Fig. 1.10e) [44]. This arrangement can further be complemented by a second detection objective, to achieve parallelized multi-view imaging (Fig. 1.10f) [45–47]. For ultimate speed, 4 identical objectives can be used to achieve almost instantaneous views from 4 different directions by using all objectives for illumination and detection (Fig. 1.10g) [48].

Furthermore, because of the wide-field detection scheme it is possible to combine SPIM with many superresolution techniques, such as single molecule localization [53], STED [54], RESOLFT [J1], or structured illumination [8, 55, 56].

1.3.1 Optics of light-sheet microscopy

Since illumination and detection for light-sheet microscopy are decoupled, two independent optical paths are implemented.

The detection unit of a SPIM is basically equivalent to a detection unit of a wide-field microscope, without a dichroic mirror (Fig. 1.11). The most important components are the objective together with the tube lens, filter wheel, and a sensor, typically a CCD or sCMOS camera.

One of the most important aspects that determines the resolution of the microscope is the detection objective. Since imaging biological specimens usually requires a water-based solution, the objectives also need to be directly submerged in the medium to minimize spherical aberrations. Since the refraction index of water ($n = 1.33$) is greater than the refraction index of air, these objectives tend to have a higher NA, which results in higher resolution. The final resolution, however, also depends on the pixel size of the sensor which determines the spatial sampling rate of the image.

Although image quality and resolution greatly depends on the detection optics, the real strength of light-sheet microscopy, the inherent optical sectioning is due to the specially designed illumination pattern, that confines light to the vicinity of the detection focal plane.

There are two most commonly used options to generate a light-sheet: either by using a cylindrical lens, to illuminate the whole field of view with a static light-sheet, as in the original SPIM concept [40]; or by quickly scanning a thin laser beam through the focal plane, thus resulting in a virtual light-sheet [49].

1. LIVE IMAGING IN THREE DIMENSIONS

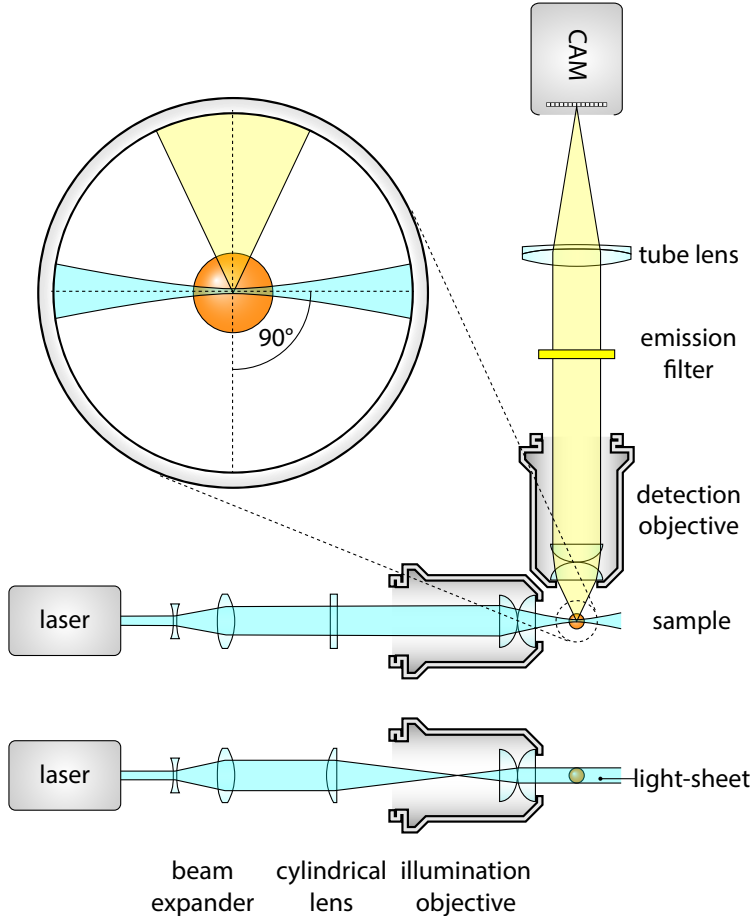


Figure 1.11: Basic optical components of a SPIM. A dedicated illumination objective is used to generate the light sheet, which is an astigmatic Gaussian beam, focuses along one direction. Astigmatism is introduced by placing a cylindrical lens focusing on the back focal plane of the objective. Detection is performed at a right angle, with a second, detection objective. Scattered laser light is filtered, and a tube lens forms the image on an area sensor, such as an sCMOS camera.

1.3.2 Static light-sheet illumination

For a static light-sheet, the normally circular Gaussian laser beam needs to be shaped in an astigmatic manner, i.e. either expanded or squeezed along one direction, to shape it into a sheet instead of a beam. This effect can be achieved by using a cylindrical lens, which as the name suggests has a curvature in one direction, but is flat in the other, thus focusing a circular beam to a sheet.

However, to achieve light-sheets that are thin enough, one would need to use cylindrical lenses with a very short focal length, and these are hardly accessible in well corrected formats. For this reason, it is more common to use a longer focal length cylindrical lens in conjunction with a microscope objective, which is well corrected for chromatic and spherical aberrations [57]. This way, the light-sheet length, thickness and width can be



Figure 1.12: Light-sheet dimensions. 1.12a The width and thickness of the field of view depends on the Rayleigh length of the beam ($z_{R,y}$) and the beam waist (W_0). 1.12b Height of the field of view is determined by the Gaussian profile of the astigmatic beam. 1.12c shows a light sheet, with the field of view indicated. Since the light-sheet intensity is uneven, the field of view has to be confined to a smaller region.

adjusted for the specific imaging tasks.

Light-sheet dimensions

The shape of the illumination light determines the optical sectioning capability and the field of view of the microscope, so it is important to be able to quantify these measures. The most commonly used illumination source is a laser beam coupled to a single mode fiber, thus its properties can be described by Gaussian beam optics.

For paraxial waves, i.e. waves with nearly parallel wave front normals, a general wave equation can be approximated with the paraxial Helmholtz equation [58]

$$\nabla_T^2 U + i2k \frac{\partial U}{\partial z} = 0 \quad (1.17)$$

where $\nabla_T^2 = \frac{\partial^2}{\partial x^2} + \frac{\partial^2}{\partial y^2}$, $U(\vec{r})$ is the wave function, $k = \frac{2\pi}{\lambda}$ is the wavenumber and z is in the direction of the light propagation.

A simple solution to this differential equation is the Gaussian beam:

$$U(r, z) = A_0 \cdot \frac{W_0}{W(z)} \cdot e^{-\frac{r^2}{W^2(z)}} \cdot e^{-i \cdot \phi(r, z)} \quad (1.18)$$

where A_0 is the amplitude of the wave, W_0 is the radius of the beam waist (the thinnest location on the beam), $r = \sqrt{x^2 + y^2}$ is the distance from the center of the beam, $W(z)$ is the radius of the beam z distance from the waist, and $\phi(r, z)$ is the combined phase part of the wave-function (Fig. 1.12a). Furthermore:

$$W(z) = W_0 \sqrt{1 + \left(\frac{z}{z_R}\right)^2} \quad (1.19)$$

1. LIVE IMAGING IN THREE DIMENSIONS

where the parameter z_R is called the Rayleigh-range, and is defined the following way:

$$z_R = \frac{\pi W_0^2}{\lambda}. \quad (1.20)$$

Apart from the circular Gaussian beam, the elliptical Gaussian beam is also an eigenfunction of Helmholtz equation (1.17) which describes the beam shape after a cylindrical lens:

$$U(x, y, z) = A_0 \cdot \sqrt{\frac{W_{0,x}}{W_x(z - z_{0,x})}} \sqrt{\frac{W_{0,y}}{W_y(z - z_{0,y})}} \cdot e^{-\frac{x^2}{W_x^2(z - z_{0,x})}} \cdot e^{-\frac{y^2}{W_y^2(z - z_{0,y})}} \cdot e^{-i \cdot \phi(x, y, z)} \quad (1.21)$$

This beam still has a Gaussian profile along the x and y axes, but the radii ($W_{0,x}$ and $W_{0,y}$), and the beam waist positions ($z_{0,x}$ and $z_{0,y}$) are uncoupled, which results in an elliptical and astigmatic beam. The beam width can be now described by two independent equations for the two orthogonal directions:

$$W_x(z) = W_{0,x} \sqrt{1 + \left(\frac{z}{z_{R,x}}\right)^2} \quad \text{and} \quad W_y(z) = W_{0,y} \sqrt{1 + \left(\frac{z}{z_{R,y}}\right)^2}. \quad (1.22)$$

Since the beam waist is different along the two axes, the Rayleigh range is also different:

$$z_{R,x} = \frac{\pi W_{x,0}^2}{\lambda}, \quad z_{R,y} = \frac{\pi W_{y,0}^2}{\lambda}. \quad (1.23)$$

Based on these equations, the light-sheet dimensions and usable field of view (fov) can be specified (Fig. 1.12c). The light-sheet thickness will depend on the beam waist, $W_{0,y}$ (if we assume the cylindrical lens is focusing along y), and the length of the light-sheet can be defined as twice the Rayleigh range, $2 \cdot z_{R,y}$. As these are coupled (see Eq. 1.23), having a thin light-sheet for better sectioning also means the length of it will be relatively short. Fortunately, because of the quadratic relation, to increase the field of view by a factor of two, the light-sheet thickness only needs to increase by a factor of $\sqrt{2}$.

Light-sheet height is determined by the intensity profile of the beam along the vertical axis (Fig. 1.12b). Since this is a Gaussian function (see Eq. 1.18), only a small part in the middle can be used for imaging, because towards the sides the intensity dramatically drops. To allow a maximum 20% drop of intensity at the edges, the light-sheet height is $h_{fov} = 2 \cdot 0.472 \cdot W_{x,0}$.

1.3.3 Digitally scanned light-sheet illumination

Although generating a static light-sheet is relatively straightforward, with the simple addition of a cylindrical lens to the light path, it has some drawbacks. As already men-

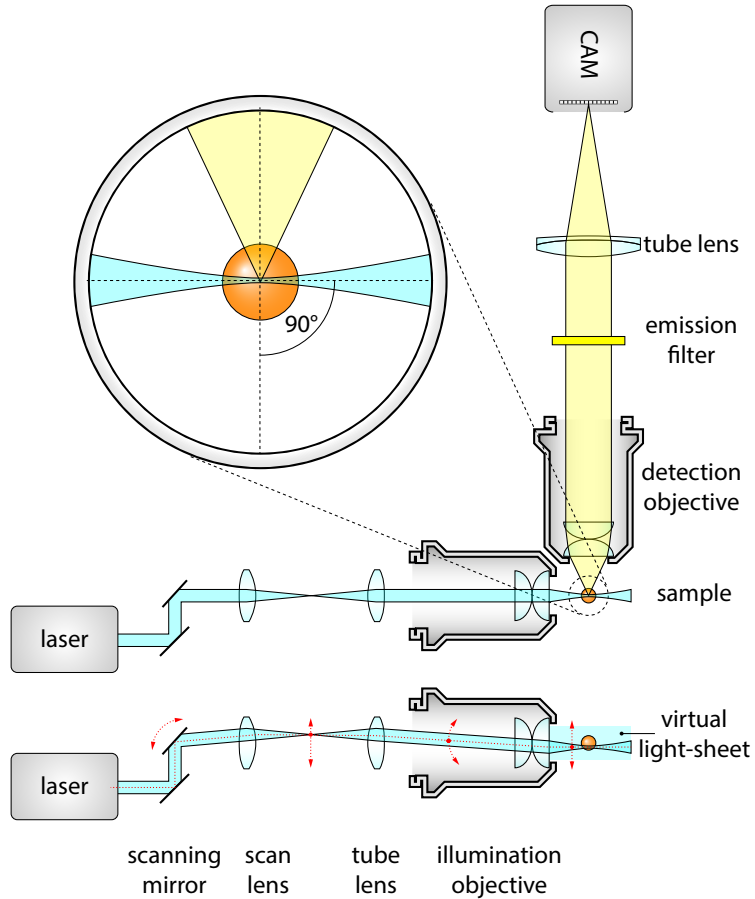


Figure 1.13: DSLM illumination. DSLM illuminates a specimen by a circularly-symmetric beam that is scanned over the field of view. This creates a virtual light-sheet, which illuminates a section of a specimen just like the SPIM. Light-sheet in DSLM is uniform over the whole field of view and its height can be dynamically altered by changing the beam scan range.

tioned in the previous section, the light intensity distribution along the field of view is not constant, as the light-sheet is shaped from a Gaussian beam. Furthermore, along the lateral direction of the light-sheet the illumination NA is extremely low, resulting in effectively collimated light. Because of this, shadowing artifacts can deteriorate the image quality [44].

A more flexible way of creating a light-sheet is by scanning a focused beam in the focal plane to generate a virtual light-sheet (digital scanned light-sheet microscopy, DSLM [49]). Although this method might require higher peak intensities, it solves both drawbacks of the cylindrical lens illumination. By scanning the beam, the light-sheet height can be freely chosen, and a homogenous illumination will be provided. Focusing the beam in all directions evenly introduces more angles in the lateral direction as well, which shortens the length of the shadows.

The basic optical layout of a DSLM is shown on Fig. 1.13. A galvanometer controlled

1. LIVE IMAGING IN THREE DIMENSIONS

mirror is used to alter the beam path that can quickly turn around its axis which will result in an angular sweep of the laser beam. To change the angular movement to translation, a scan lens is used to generate an intermediate scanning plane. This plane is then imaged to the specimen by the tube lens and the illumination objective, resulting in a scanned focused beam at the detection focal plane. The detection unit is identical to the wide-field detection scheme, similarly to the static light-sheet illumination. By scanning the beam at a high frequency, a virtual light-sheet is generated, and the fluorescent signal is captured by a single exposure on the camera, resulting in an evenly illuminated field of view.

1.4 Light-sheet microscopy for mouse imaging

Because of its optical sectioning capabilities, combined with the high specificity of fluorescent labels, confocal microscopy had an immense influence on biological research, and has been the go-to technique for decades for many discoveries [59–61]. Live imaging capabilities of confocal microscopy are, however, limited. This is mostly due to the illumination scheme: to collect information from a single point, almost the whole embryo has to be illuminated. This unwanted illumination can easily lead to bleaching of the fluorophores, and also to phototoxic effects that can prevent further embryonic development. The point scanning nature of image acquisition also implies an inherent constraint to the maximum imaging speed, as it can be only increased at the expense of reducing signal intensity (Fig. 1.1).

One improvement to address both of these drawbacks is the use of a spinning disk with a specific pattern (also called Nipkow disk) of holes to generate multiple confocal spots at the same time [60]. If these spots are far enough from each other, confocal rejection of out-of-focus light can still occur. As the disk is spinning, the hole pattern will sweep the entire field of view, eventually covering all points [62]. The image is recorded by an area detector, such as a CCD or EM-CCD, which speeds up image acquisition [63].

Although out-of-focus illumination is still an issue, spinning disk confocal microscopy was successfully used to investigate the mechanisms of symmetry breaking in early mouse embryonic development [64], and the mechanisms leading to the first cell fate specification that will differentiate extraembryonic tissue from the embryo proper [33, 65, 66]. Even though these studies were carried out with live embryos, only a few hours of continuous imaging is possible before the accumulation of phototoxic effects arrests development [67]. Compared to this, just the pre-implantation phase of mouse embryonic development spans 3 days, and the full development is 18 days [68].

1.4.1 Imaging pre-implantation

Pre-implantation is the first phase of mouse embryonic development, that starts right after fertilization. The embryo in this phase is still in the oviduct, travelling towards the uterus, where it will implant to the uterine wall. The developmental stage between fertilization and the implantation is called the pre-implantation stage. Here the embryo divides, and already the first cell fate specifications start when forming the trophoectoderm (TE) and the inner cell mass (ICM) at the blastocyst stage. ICM cells will form the embryo proper, while TE cell will contribute to the formation of the extraembryonic tissues.

During this process the embryo is still self-sufficient, which makes it possible to image this stage in an *ex vivo* embryo culture by providing the proper conditions [69]. Long term imaging, however, is extremely challenging due to the very high light sensitivity of the specimens. Imaging these embryos in a confocal microscope will lead to incomplete development, even if the imaging frequency is minimized to every 15 mins [J2].

Imaging for just a few hours is already enough to investigate important processes, such as cell fate patterning [70]. Other approaches aim to lower the phototoxicity by either using 2-photon illumination which operates at longer wavelengths [71–73], or by lowering imaging frequency as a compromise [74]. These approaches, however either require highly specialized equipment, such as an ultra short pulsed laser, or is compromising on the time resolution.

Light-sheet microscopy, on the other hand, drastically lowers phototoxic effect by using a much more efficient illumination scheme (see Sec. 1.3), and thus makes a better use of the photon budget. Using this technique, it is possible to image the full pre-implantation development at high spatial and temporal resolution without any negative impact on the developmental process. Such a microscope was developed by Strnad *et al.* at EMBL [J2], who used it to understand when exactly is the first cell fate specification decided in the embryonic cells.

As a mouse embryo culture is not compatible with the standard agarose-based sample mounting techniques, a completely new approach was taken, which resulted in a microscope designed around the sample. The sample holder forming a V-shape was built with a bottom window, and it is lined with a thin FEP (fluorinated ethylene propylene) foil that supports the embryos (Fig. 1.14A, i). This arrangement allows the utilization of the standard microdrop embryo culture, while providing proper viewing access for the objectives. As the embryos are relatively small (100 µm) and transparent, a single illumination and single detection objective arrangement is enough for high quality imaging. A low resolution (NA=0.3) objective is used to generate the scanned light-sheet, and a high resolution (NA=1.1) objective is detecting the fluorescence at 50×magnification (Fig 1.14A, ii). As the foil is curved, it allows unrestricted access to the embryo, while

1. LIVE IMAGING IN THREE DIMENSIONS



Figure 1.14: Inverted light-sheet microscope for multiple early mouse embryo imaging.. (i) A sample holder (SH), containing a transparent FEP membrane (M) allows multiple embryo samples (S) to be placed in line for multisample imaging. (ii) Inverted objective orientation with side view of the sample holder. One possible configuration is to use a 10×0.3 NA illumination objective (IL) and another 100×1.1 NA detection objective placed at a right angle to the illumination. (iii) Close up on side view of sample on FEP membrane with both objectives. Since the FEP membrane is transparent on water, it provides no hindrance to the illumination beam in penetrating the sample or for the emitted fluorescence on reaching the detection objective. (B) Still images of one particular timelapse experiment, and (C) corresponding segmented nuclei. The star depicts the polar body. Adapted from Strnad *et al.* [J2]

separating the imaging medium from the immersion liquid (Fig. 1.14A, iii). Furthermore, its refractive index is matching the refractive index of water, so optical aberrations are minimized.

Using this setup, Strnad *et al.* were able to pinpoint the exact timing of the first cell fate decision that leads either to ICM or TE cells. More than 100 embryos expressing nuclear (H2B-mCherry) and membrane (mG) markers were imaged for the entire 3 days of pre-implantation development (Fig. 1.14B). The image quality was good enough to segment all nuclei in the embryos (Fig. 1.14C), and track them from 1 to 64 cell stage, building the complete lineage tree. Based on the lineage trees, and the final cell fate assignments, it was determined that at the 16 cell stage the final specification is already decided, while earlier than this it is still random.

1.4.2 Imaging post-implantation development

After the initial 3 days of pre-implantation, the embryo undergoes the implantation process, during which it is inaccessible to microscopical investigations. Although a new method was recently developed that allows *in vitro* culturing of the embryos embedded in a 3D gel [76], this has not reached wider adoption yet. Because of this, developmental processes during implantation have only been investigated in fixed embryos.

Following the implantation process, at the post-implantation phase, *ex vivo* embryo

1.4 Light-sheet microscopy for mouse imaging

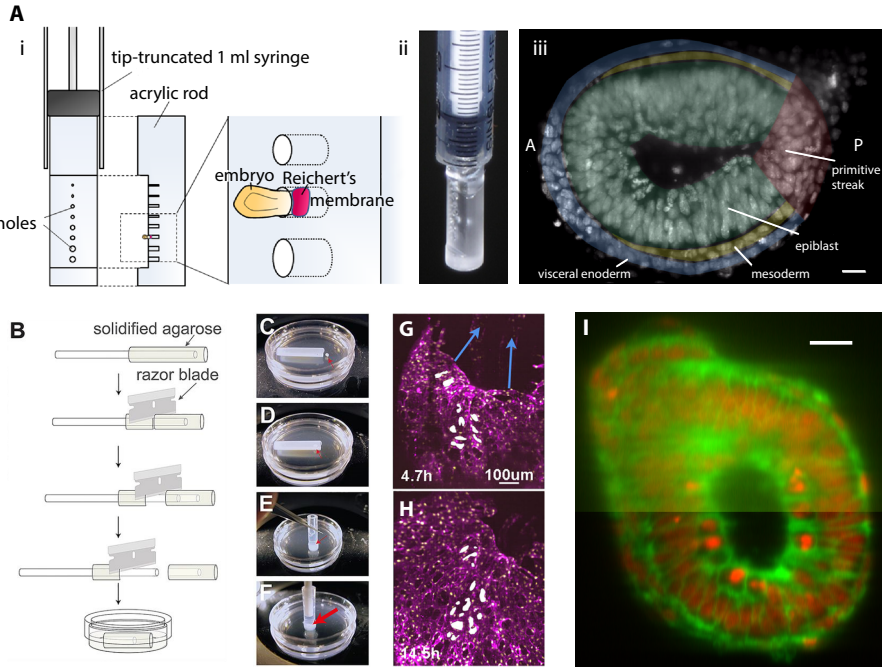


Figure 1.15: Imaging mouse post-implantation development. (A) (i, ii) Mounting technique for E5.5 to E6.5 embryos. A tip-truncated 1 mL syringe holds an acrylic rod, cut and drilled with holes of different size in order to best fit the mouse embryo by its Reichert's membrane, leaving the embryo free inside the medium. (iii) Maximum intensity projection of a 13 μm slice at 78 μm from distal end of an E6.5 mouse embryo. The different tissues corresponding to the rudimentary body plan are annotated. Scale bar: 20 μm . (B) For stages ranging between E6.5 and E8.5, mounting using a hollow agarose cylinder has also successfully been proposed. Optimal sizes for the corresponding embryonic stage to be imaged can be produced, so that the embryo can grow with least hindrance. (C–F) Steps for mounting the mouse embryo inside the agarose cylinder. The inner volume of the cylinder can be filled with optimal medium, allowing the much larger chamber volume to have less expensive medium. (G–H) Example images of a 9.8 h timelapse with the mounting shown in (B) where the expansion of the yolk sac can be observed in direction of the blue arrows. (I) In order to aid multiview light-sheet setups in overcoming the higher scattering properties of embryos at this stage, and to allow faster and easier data recording, electronic confocal slit detection allows better quality images to be taken at shorter acquisition times. Scale bar: 20 μm . Adapted from Ichikawa *et al.* [50], Udan *et al.* [51] and de Medeiros and Norlin *et al.* [75].

culturing becomes possible again [77, 78], and these embryos can be kept alive for several days in an artificial environment. During this process especially interesting stages are the late blastocyst (\sim E4.5), gastrulation (\sim E6.5), and somite formation (\sim E8.5). Before live imaging techniques became available, these stages were mostly investigated using *in situ* visualization techniques to shed light on several developmental processes [79]. Many pathways playing important roles have been identified this way, however live imaging is still necessary to validate these results, and ensure continuity in the same specimen [80].

Light-sheet microscopy is a good choice for imaging these stages, just like in the case of pre-implantation embryos. These embryos, however, present new challenges for sample handling and culturing. Owing to their extreme sensitivity, dissection can be difficult, especially for earlier stages (E4.5). Furthermore, since the embryo is also growing during development, gel embedding is not an option, as this might constrain proper development. Thus, special handling and mounting techniques had to be developed in order to allow

1. LIVE IMAGING IN THREE DIMENSIONS

live 3D imaging of these specimens.

Ichikawa *et al.* [50] designed a custom mounting apparatus manufactured from acrylic in the shape of a rod that fits in a standard 1 mL syringe with its tip truncated (Fig. 1.15A, i). In the rod several holes were drilled with different sizes that can accommodate different sized embryos, which are held by an extraembryonic tissue, the Reichert's membrane (Fig. 1.15A, ii). Mounting this way doesn't disturb the embryo itself, and it can freely develop in the culturing medium, while it is also stationary for the purpose of imaging. Using this technique, Ichikawa *et al.* were able to image through several stages of development, including interkinetic nuclear migration at stages E5.5–6.5 (Fig. 1.15A, iii).

A second method of sample mounting for light-sheet imaging was developed by Udan *et al.* who were able to record a full 24 h time-lapse of living embryos focusing on the gastrulation and yolk sac formation processes (Fig. 1.15G–I). Their mounting technique comprised of producing a hollow agarose container shaped like a cylinder that could support the embryo from below without constraining its growth (Fig. 1.15B–F).

Another consideration to keep in mind, is the growing size of the embryo. As it gets bigger, illumination is less efficient, and scattering can dominate at larger depths. As mentioned in earlier (Sec. 1.3) this can be alleviated by multi-view imaging: illuminating and detecting from multiple directions. Electronic confocal slit detection can further improve the signal to noise ratio by rejecting unwanted scattered light, which allows deeper imaging in large specimens, even up to E7.5 (Fig. 1.15I) [75].

1.4.3 Imaging adult mice

Imaging adult mice is especially interesting for answering neurobiological questions. Since development is over at this stage, the use of an environmental chamber is no longer necessary. The biggest challenge for imaging these samples is their size, as they are centimeters in size instead of less than a millimeter in the embryonic stage. Furthermore, the tissues of adult mice are much more opaque which severely limits imaging depth. Light-sheet microscopy can already deal with large specimens, however to achieve (sub)cellular resolution for an entire brain for example, multiple recordings have to be stitched together after acquisition [81].

Light scattering and absorption depends on the tissue composition, and also imaging depth. Especially the brain with the high concentration of lipids in the myelinated fibers pose a real challenge for imaging. Live imaging is usually performed with 2-photon microscopy which can penetrate the tissue up to 800 μm [82]. Using fixed samples, however, the scattering problem can be eliminated by the use of tissue clearing methods.

Tissue clearing is a process that removes and/or substitutes scattering and absorbing molecules by a chemical process while keeping the tissue structure intact and preserving

1.4 Light-sheet microscopy for mouse imaging

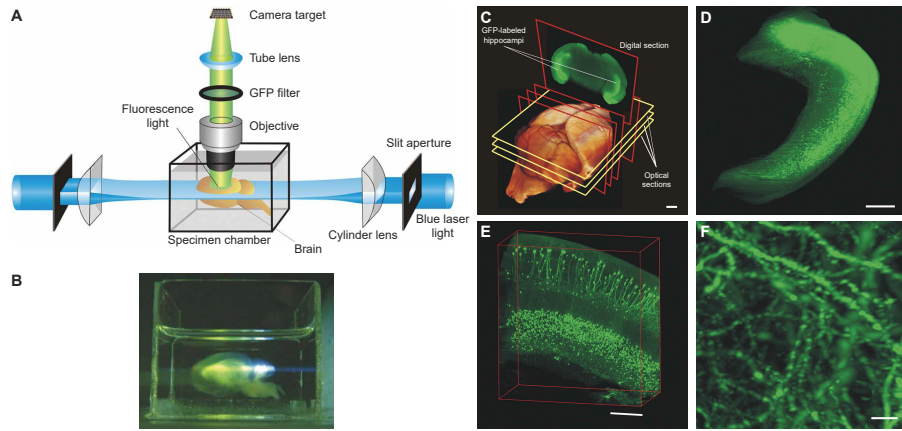


Figure 1.16: Imaging adult mouse brain with light-sheet microscopy.. (A) Schematics of the ultramicroscope for brain imaging. The specimen is embedded in clearing medium to ensure necessary imaging depth. Illumination is applied from two sides to achieve even illumination for the whole field of view. Light-sheet is generated by a slit aperture flowed by a cylindrical lens. The specimen is imaged from the top using wide-field detection method. (B) Photograph of the imaging chamber with a mounted cleared specimen and light-sheet illumination. (C) Surface rendering of a whole mouse brain, reconstructed from 550 optical sections. GFP and autofluorescence signal was imaged. Hippocampal pyramidal and granule cell layers are visible in the digital section. Scale bar: 1 mm. Objective: Planapoachromat 0.5×. (D) Reconstruction of an excised hippocampus from 410 sections. Note that single cell bodies are visible. Scale bar: 500 µm. Objective: Fluar 2.5×. (E) 3D reconstruction of a smaller region of an excised hippocampus from 132 sections. Scale bar: 200 µm. Objective: Fluar 5×. (F) 3D reconstruction of CA1 pyramidal cells imaged with a higher resolution objective (LD-Plan Neofluar 20× NA 0.4) in a whole hippocampus (430 sections). Dendritic spines are also visible, even though usually a higher NA objective (>1.2) is required to visualize these. Scale bar: 5 µm. Adapted from Dodt *et al.* [7].

fluorescence. The most dominant contributors to these effects are the proteins and lipids. Proteins in the cells locally change the refractive index of the tissue which leads to scattering, while lipids absorb the light. Clearing methods tackle these problems by chemically removing and substituting lipids by certain types of gel, and immersing the whole sample in a medium with higher refractive index to match the optical properties of proteins. Numerous methods have been developed for tissue clearing, such as ScaleA2 [83], 3DISCO [84, 85], ClearT2 [86], SeeDB [87], CLARITY [88, 89], CUBIC [90] and iDISCO [91].

The first combination of optical clearing and light-sheet microscopy for whole brain imaging was performed by Dodt *et al.* using a custom ultramicroscope consisting of two opposing illumination arms and a single detection with an objective from above (Fig. 1.16A). The light-sheets were positioned horizontally, and the cleared samples could be placed in a transparent imaging chamber filled with the clearing medium (Fig. 1.16B). Imaging was performed from both top and bottom after rotating the sample 180°. By changing the detection lens, it is possible to adapt the system to different samples: low magnification is capable of imaging the whole brain (Fig. 1.16C), while for smaller, dissected parts, such as the hippocampus, higher magnification with higher resolution is more appropriate (Fig. 1.16D). With this configuration individual cell-cell contacts can be recognized (Fig. 1.16E), and even dendritic spines can be visualized (Fig. 1.16F).

1. LIVE IMAGING IN THREE DIMENSIONS

Although light-sheet microscopy is highly suitable for imaging cleared specimens, even entire mice [92], brain imaging in live animals is more challenging due to the standard two-objective setup of a conventional SPIM microscope. Two light-sheet based methods, however offer a solution for this, axial plane optical microscopy (APOM) [93] and swept confocally-aligned planar excitation (SCAPE) [94] both use only a single objective to generate a light-sheet and detect the fluorescence as well. This is done by rotating the detection plane at an intermediate image (APOM), or by rotating both the light-sheet and detection plane simultaneously (SCAPE).

Chapter 2

Dual Mouse-SPIM

mammalian development chromosome segregation cell specification symmetry breaking
signaling pathways human infertility congenital diseases

current mouse-SPIM [J2] already is very good for answering many of these questions
resolution from beads: diSPIM [43] combine these two plus also [95]

advantages: immersion liquid and culture medium separated open-top sample holder
allow standard microdrop *in vitro* embryo culture row of embryos - high throughput dual
color imaging environmental chamber allows live imaging for 3 days, every

follow chromosomes by tracking kinetochores

from lattice paper: “because photodamage mechanisms that scale supralinearly with
peak intensity have been identified for both visible [96] and two-photon [97] excitation.”

2.1 Microscope design principles

In order to address the challenges outlined in the previous section, we propose a new light-sheet microscope design for imaging pre-implantation development at high resolution. The design is guided by the following requirements:

1. subcellular, isotropic resolution
2. high light collection efficiency
3. live embryo compatible

design principles: highest isotropic resolution, highest light collection efficiency possible
2x0.8 NA water dipping in 90° multi-view deconvolve Gaussian fit $\sigma_{xyz} = 135$ 2x1.1
NA water dipping in 120° multi-view deconvolved Gaussian fit $\sigma_z = 135$, and $\sigma_{xy} = 82.2$
simulations from PSF generator! put here

2. DUAL MOUSE-SPIM

2.1.1 Light collection efficiency of an objective

Resolution is not the only parameter of concern when designing a new microscope setup. We also have to consider light collection efficiency, since many application, especially live imaging applications require a tight photon budget. This means a single fluorophore can only emit so many times before it undergoes an irreversible chemical reaction, i.e. it bleaches. The more we can collect of these photons, the more information we gain, and altogether the efficiency is higher.

Photon collection efficiency also defines single molecule localization accuracy, since the signal to noise ratio will depend on the square of the number of collected photons. This is why it's important to also maximize light collection efficiency.

Let's define light collection efficiency η as the ratio of collected photons and all emitted photons:

$$\eta = \frac{N_{\text{collected}}}{N_{\text{emitted}}}$$

Since we can assume that the direction of photons emitted from a fluorescent molecule are random, the light collection efficiency will correspond to the solid angle subtended by the objective front lens at the focal point. To calculate this, let's consider the unit sphere centered at the focal point, and calculate the surface area of the spherical cap corresponding to the objective acceptance angle α (Fig. 2.1a). The area of the cap can be expressed as a function of the angle:

$$A_{\text{cap}} = 2\pi r^2(1 - \cos \alpha)$$

The surface area of the full sphere is calculated as:

$$A_{\text{sph}} = 4\pi r^2$$

For both equations r is the radius of the sphere. From here, the light collection efficiency can be calculated as:

$$\eta = \frac{N_{\text{collected}}}{N_{\text{emitted}}} = \frac{A_{\text{cap}}}{A_{\text{sph}}} = \frac{1 - \cos \alpha}{2}$$

Some more calculations: (Fig. 2.1b).

2.1.2 Multi-view resolution

here a figure with rotating 2 psfs

In order to maximize light-collection efficiency and resolution, we opted for a high-NA water dipping objective, the Nikon CFI75 Apo LWD 25x/1.1w model. Two of these arranged in 120° allows for twice improved light collection efficiency compared to the 0.8 NA configuration in 90° alignment, with further improved lateral resolution along

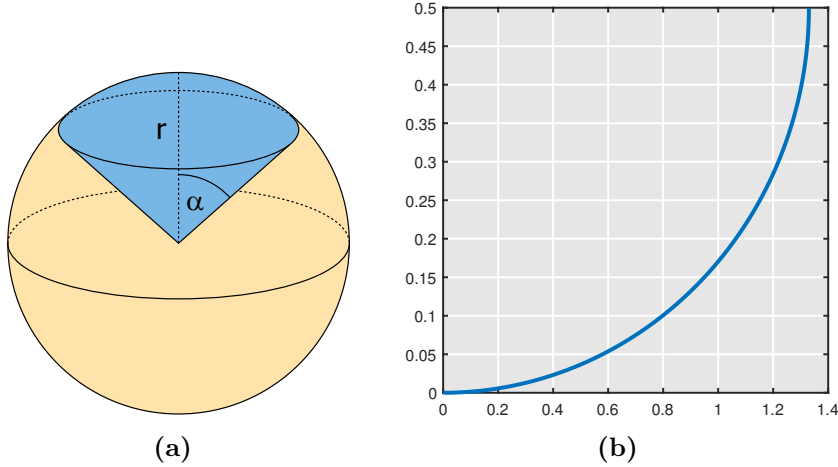


Figure 2.1: Light collection efficiency of an objective. (a) Light collection efficiency is the ratio of photons collected by the objective and all emitted photons. If the fluorophores are emitted randomly in all directions, it will be the surface ratio of the conical section (blue) to the whole sphere. (b) Light collection efficiency (η) as a function of the numerical aperture (NA)

2 axes (Figure 2.2). In the next section we will describe the design considerations for illumination and detection optics to achieve optimal sample illumination.

2.1.3 Light-sheet design

To allow for flexibility in the field of view height, even illumination, reduced stripes, and potential for confocal line detection, we opted to use the beam scanning technique to generate a virtual light-sheet. The effective focal length of the Nikon 25x objective, given the 200 mm focal length tube lens is

$$f_o = \frac{f_{tl}}{M} = \frac{200 \text{ mm}}{25} = 8 \text{ mm}, \quad (2.1)$$

and the back aperture diameter is 17.6 mm.

To generate the tilted light-sheet as shown on Fig. 2.3, the illumination beam will need to be displaced by

$$\delta = f_o \cdot \tan 30^\circ = 4.62 \text{ mm} \quad (2.2)$$

Since the Gaussian beam is not uniform, only a smaller portion of it can be used to maintain even illumination (Figure 1.12c). Because the size of an early mouse embryo is around 80 μm , we require the length and the height of the light-sheet to be at least 100 μm .

2. DUAL MOUSE-SPIM

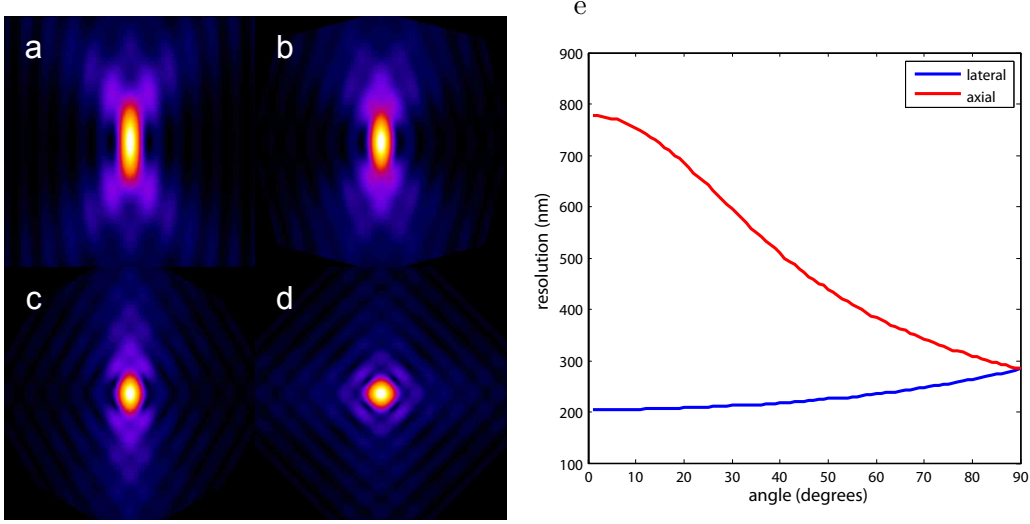


Figure 2.2: Lateral and axial resolution of a multi-view optical system. a) Simulated PSF for a single view. b)-d) Simulated compound PSF of two views aligned in b) 30, c) 60 and d) 90 degrees to each other. e) Axial and lateral resolution of a dual-view setup depending on the rotation angle of the two objectives. Parameters used for calculations: NA=1.1, $\lambda_{ex} = 488\text{nm}$, $\lambda_{det} = 510\text{nm}$, $n = 1.333$ for water immersion.

The length and thickness of the light-sheet

As we saw in section 1.3.2, the length of the light-sheet is determined by the Rayleigh-range of the beam in the zy plane. Since $l_{fov} = 2 \cdot z_R = 100\text{ }\mu\text{m}$

$$z_R = 50\text{ }\mu\text{m} \quad (2.3)$$

Since the Rayleigh range and the diameter of the beam waist are coupled, the light-sheet thickness can be calculated after rearranging Equation 1.20

$$2 \cdot W_0 = 2 \cdot \sqrt{\frac{z_R \cdot \lambda}{\pi}} = 5.57\text{ }\mu\text{m} \quad (2.4)$$

when $\lambda = 488\text{ nm}$ for GFP excitation. As the beam width for these calculations is defined as $1/e^2$ of the peak intensity, we also calculate the more commonly used FWHM:

$$\text{FWHM} = W_0 \cdot \sqrt{2 \ln 2} = 3.28\text{ }\mu\text{m.} \quad (2.5)$$

From this, the divergence angle of the beam is

$$\theta_0 = \frac{\lambda}{\pi W_0, y} = 55.74\text{ mrad} = 3.196^\circ \quad (2.6)$$

This means, the numerical aperture needed to produce this light-sheet is:

$$\text{NA}_{ls} = n \cdot \sin(\theta_0) = 0.0743 \quad (2.7)$$

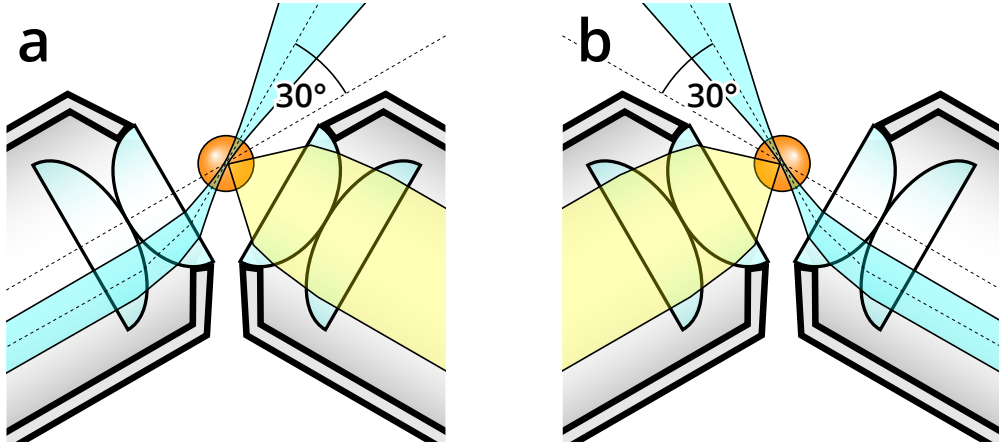


Figure 2.3: Dual view concept with high NA objectives. To achieve multi-view detection while maximizing resolution and light collection efficiency, two high NA objectives are placed in 120° arrangement. To be able to overlap the light-sheet with the focal plane, the light-sheet is tilted 30°. Because of the high NA objectives, this tilt does not effect the illumination quality. The objectives are used in an alternating sequence for illumination and detection.

Since $\text{NA} = 1.1$, and the diameter of the back aperture is $d = 17.6 \text{ mm}$ and the divergence angle $\theta_0 \ll 1$, using paraxial approximation, the necessary beam width at the back focal plane in the y direction is

$$b_y = d \cdot \frac{\text{NA}_{ls}}{\text{NA}} = 1.19 \text{ mm} \quad (2.8)$$

Thus, to generate a light-sheet with appropriate length to cover a whole mouse pre-implantation embryo, the laser beam diameter should be $b = 1.19 \text{ mm}$. Larger than this will result in a more focused beam, and a shorter light-sheet, while a smaller diameter beam will have worse optical sectioning capabilities.

The height of the light-sheet

The height can be adjusted by changing the beam scanning amplitude with the galvo mirror. To scan the entire field of view of $h_{fov} 270 \mu\text{m}$, the scanning angle range at the back focal plane of the objective will need to be $\theta = \tan^{-1}(h_{fov}/2/f_o) = \pm 0.967^\circ$.

2.2 Optical layout

Based on the requirements and other considerations layed out in the previous section, the microscope was designed based on three main parts: 1) the core unit, 2) illumination and 3) detection branches. The aim when integrating everything together was to allow for high level of flexibility with robust operation, while keeping efficiency at a high level. After finalizing the concept, the optical layout of the microscope was designed in SolidWorks.

2. DUAL MOUSE-SPIM

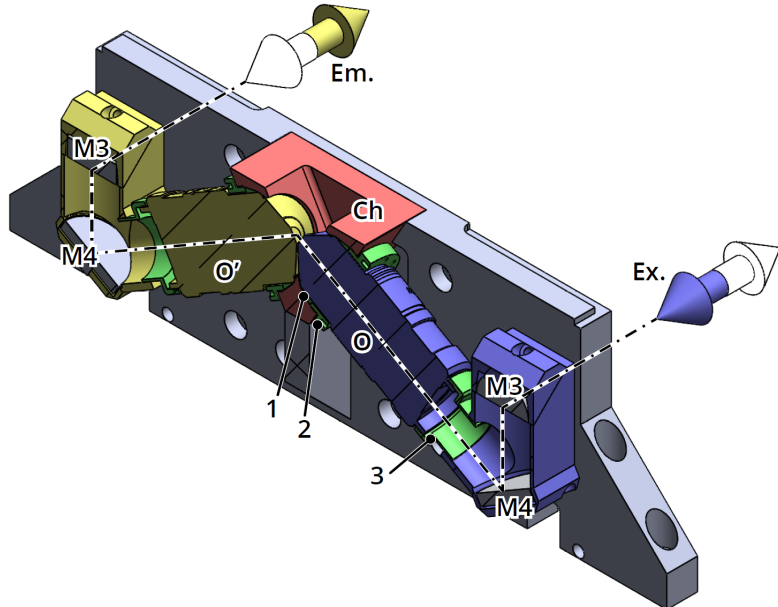


Figure 2.4: The core unit of the microscope. The two objectives (O and O') are mounted on a solid 15 mm thick aluminium plate. Fitting on the objectives, a custom chamber (Ch) is holding the immersion medium for imaging. The mirror block with mirrors $M3$ and $M4$ directs the light to 65 mm optical rails. Excitation (Ex.) and emission (Em.) light paths are indicated by the dash-dot line. Due to the symmetric arrangement, the excitation and illumination paths can be switched around. Objectives are secured with rings 1–3 (green, see main text for details).

2.2.1 Core unit

As the most important part of the microscope is actually the sample, the design is based around a core consisting of the imaging chamber and the objectives (Figure 2.4). Also part of the core are two mirror blocks placed at the back of the objectives, and three custom designed rings to hold the objectives in place. The objectives are pointing slightly up, closing a 60° angle with the horizontal plane, and 120° angle with each other.

Chamber

The chamber serves two purposes: it holds the immersion liquid necessary for imaging, and it also keeps the objectives in the 120° position. The objectives are held by their necks as opposed to the standard mounting method from the back by the threads. The advantage of this is that any axial movements due to thermal expansion are greatly reduced, thus the focal plane position is more stable even when changing the imaging conditions.

The chamber is machined from a high performance plastic, poly(ether-ether-ketone) (PEEK). This material has many beneficial properties: it is food safe, and chemically extremely inert, resisting to most solvents used in a biology laboratory. It can also be autoclaved. Compared to other plastics its mechanical properties are also superior. It has

high tensile and compressive strength, comparable to aluminium, low thermal expansion and low thermal conductivity. This can be beneficial when implementing temperature control, as thermal loss is reduced.

The objectives are kept in place by two custom designed rings (Figure 2.4 1, 2). The first ring has a cross sectional shape of a wedge, and sits tightly against both the objective and the wall of the chamber. The second ring can freely slide on the objective, and has threads matching the chamber. When turned in, the threaded ring pushes the wedge ring further in, which in turn presses against the objective and the chamber wall uniformly, thus preventing the objective from moving, and sealing the chamber at the same time. As the wedge ring is made from a soft plastic (delrin), it will press evenly against the objective preventing any damage. Because of the conical shape of the ring, it will also automatically center the objective, ensuring correct positioning.

To relieve any rotational stresses from the objective, the back of the objective is also supported by the mirror block, this is not fixed, however. A third ring, made of PEEK is screwed on the thread of the objective, and slides in the opening of the mirror block. This reduces the torque on the objectives, while still allowing for some movements that might occur due to thermal expansion.

Mirror blocks

Apart from supporting the objectives from the back, the mirror blocks are housing two broadband dielectric mirrors (Thorlabs, BBE1-E03 and OptoSigma, TFMS-30C05-4/11) to direct the light in and out from the objectives on a standard 65 mm height, compatible with the Owis SYS65 rail system. The combination of two mirrors have two benefits compared to using just one. With a single mirror directly reflecting the light to the back, the entire assembly would need to be much higher to reach the desired 65 mm height. This could result in stability problems. Furthermore, due to the 60° rotation angle of the objective, the image of the objective would also be rotated if using only a single mirror. With two mirrors the reflection planes can be kept orthogonal to the optical table, which will result in a straight image after the mirror block. This is not only beneficial when recording the images, but also when aligning the illumination arm. With the use of two mirrors, a convenient vertical scanning is required to produce the light-sheet; with a single mirror, the scanning direction would need to be rotated by 60°.

2.2.2 Illumination

The illumination arm of the microscope directs and shapes the laser beam to generate the proper light-sheet dimension at the sample. As was calculated in subsection 2.1.3, a beam diameter of 1.2 mm is ideal for this setup.

The illumination arm has 3 main roles:

2. DUAL MOUSE-SPIM

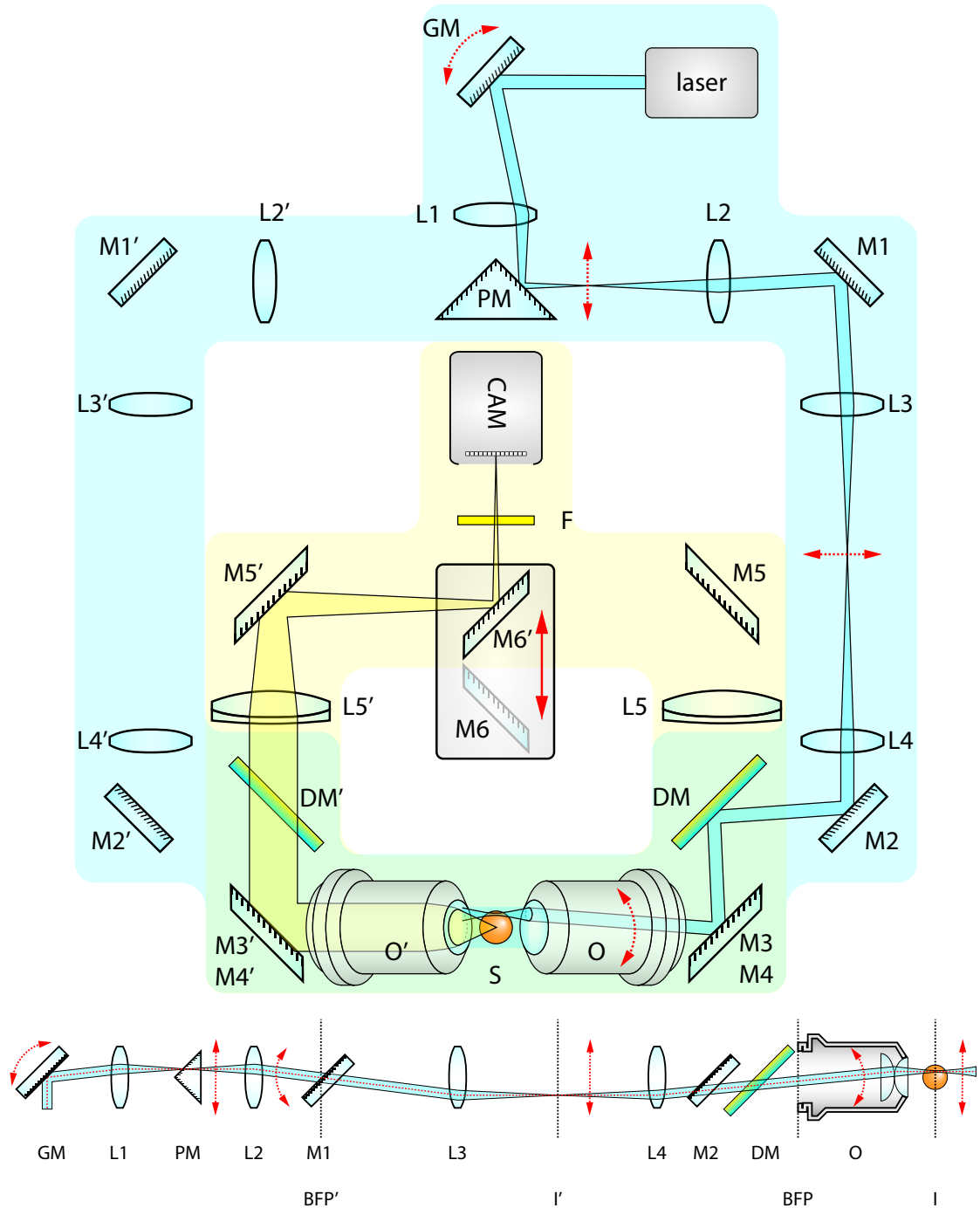


Figure 2.5: Dual Mouse SPIM optical layout. The microscope consists of two main parts, the illumination branches (blue) and detection branches (yellow). For both illumination and detection there are two identical paths implemented. Illumination direction can be changed by applying a different offset to the galvo mirror, which in turn will direct the beam to the opposite face of the prism mirror. L1 and L2 will then image the galvo on M1. Using L3 as a scan lens, and L4 as a tube lens, the scanned beam is coupled to the objective path by quad band dichroic mirror (DM) CAM – camera, DM – dichroic mirror, F – filter wheel, L – lens, M – mirror, O – objective, PM – prism mirror, S – sample

1. expands the laser beam to the calculated 1.2 mm size.
2. images the galvo scanner to the back focal plane of the objective
3. switches the laser light between the two objectives during imaging

To achieve the desired beam diameter, a 1:2 beam expander (Sill Optics, 112751) is used in the reversed direction. As the output of the laser fiber produces a 3 mm diameter beam, this will reduce it to 1.5 mm. As this is already the required beam diameter, the lenses further in the illumination path will not introduce any magnification.

Switching between the two illumination arms is performed by a custom designed beam splitter unit (Figure 2.6). Instead of utilizing a 50/50 beam splitter cube and mechanical shutters, we exploit the fact that a galvo scanner is needed to generate the light-sheet. As this galvo scanner (Cambridge Technology, 6210B) has a relatively large movement range ($\pm 20^\circ$) it is also suitable for diverting the beam from one illumination arm to the other.

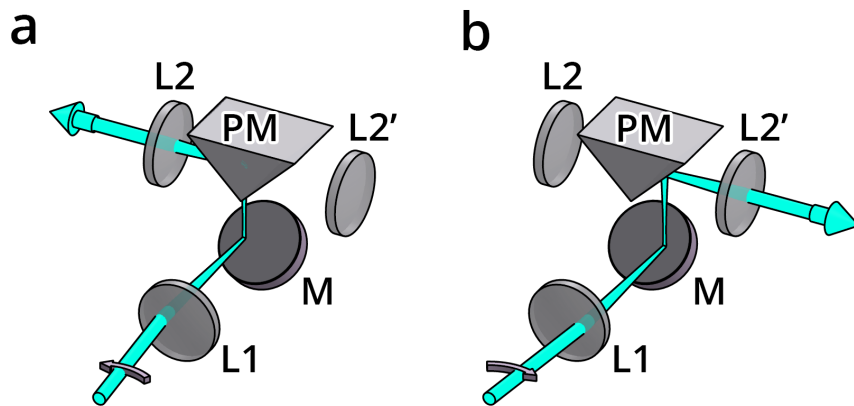


Figure 2.6: Illumination branch splitting unit. To divert the beam to either side, a right angle prism mirror is used in conjunction with a galvanometric scanning mirror. L1 acts as a scan lens, thus the beam is translated on mirror M. Depending on the galvo angle, the beam will be reflected either to the left (a) or to the right (b). L2 and L2' act as relay lenses, and will image the galvo movement to intermediate planes.

Switching illumination side is done the following way. As the galvo is positioned at the focus of the first lens (L1, $f_1 = 75$ mm, Edmunds Optics, #47-639), the rotational movement will result in a linear scanning movement on mirror M and the prism mirror PM (Thorlabs, MRAK25-E02). Depending on the lateral position of the beam, it will hit either the left or the right leg of the prism, and will be reflected to either direction. As the galvo mirror can be precisely controlled through our custom software, we can set and save the position when the beam is centered on the left lens L2 ($f_2 = 75$ mm, Edmunds Optics, #47-639) (Figure 2.6a) and the position when the beam is centered on the right lens L2' (Figure 2.6b). Lenses L1 and L2(L2') form a 4f system, and are imaging the galvo scanner on mirror M1(M1') (Figure 2.5). This way we can use the same galvo to generate the light-sheet for both directions, depending on the initial offset position. This

2. DUAL MOUSE-SPIM

not only has the advantage of being able to electronically switch the illumination arms, but only requires a single galvo scanner instead of one for each arm.

Due to the arrangement of the bottom mirror and the prism mirror, the scanning direction will be rotated by 90°. This will result in a vertical scanning plane, which is exactly what we need to generate the light-sheet on the sample (see section 2.2.1).

Further following the illumination path, two achromatic lenses L3 and L4 ($f_3 = f_4 = 200\text{ mm}$), in a 4f configuration relay the scanning axis to the back focal plane (BFP) of the objective. To couple in the laser with the imaging path, a quad-band dichroic mirror (DM, Semrock, Di03-R405/488/561/635-t3-25x36) is used, matching the wavelengths of the laser combiner.

2.2.3 Detection

As the emitted light exits the objective and the mirror block, it is decoupled from the illumination path by the dichroic mirror. The light is then focused by a 400 mm achromatic lens (L5, Edmunds Optics, #49-281) onto the camera sensor (Andor Zyla 4.2 sCMOS). Just before the camera, a motorized filter wheel (F, LEP 96A361) is placed to filter out any unwanted wavelength from the emission light. Although this is not in the infinity space, due to the very small angles after the 400 mm tube lens, the maximum axial focal shift is $\sim 50\text{ nm}$ only, which is negligible compared to the axial resolution of $\sim 1.1\text{ }\mu\text{m}$.

Similarly to the common galvo in the illumination path, the two detection arms share the same camera. Although two cameras could also be used, due to the operating principle of the microscope, the two objective are not used for imaging at the same time. This means a single camera is capable of acquiring all the images, however, the two distinct detection arms need to be merged to be able to use a single camera.

Our solution to this problem is a custom designed view switching unit comprised of two broadband dielectric elliptical mirrors (Thorlabs,BBE1-E03) facing opposite directions, mounted on a high precision linear rail (OptoSigma, IPWS-F3090). Depending on the rail position, either the left (Figure 2.7a) or the right (Figure 2.7b) detection path will be reflected up, towards the camera.

Moving the switcher unit is performed by a small, 10 mm diameter pneumatic cylinder (Airtac, HM-10-040) that is actuated by an electronically switchable 5/2 way solenoid valve (Airtac, M-20-510-HN). This solution offers a very fast switching between views, up to 5 Hz, depending on the pressure, and it is extremely simple to control, as only a digital signal is necessary to switch the valve.

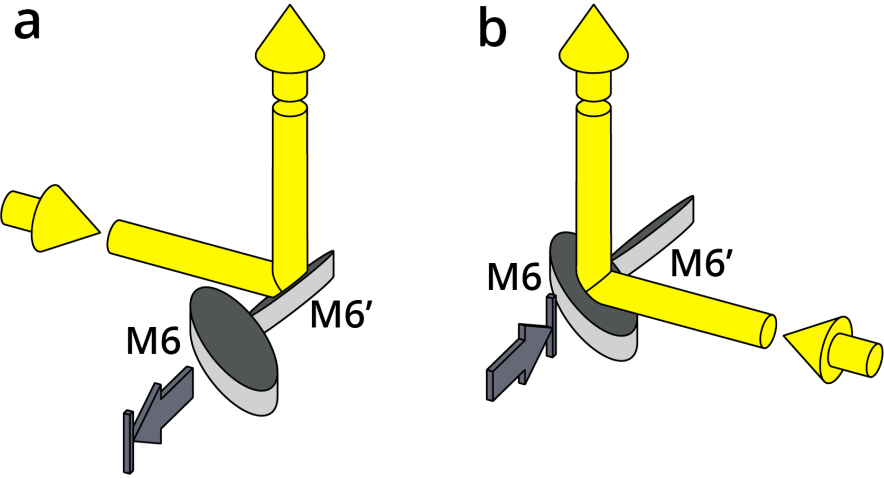


Figure 2.7: Detection branch switching unit. To be able to image both views on the same camera, a moveable mirror unit is introduced. Depending on the imaging direction, the mirror block is either moved backward (a) or forward (b) to reflect the light up to the camera. Since the movement is parallel to the mirrors' surface, the image position on the sensor is not dependent on the exact position of the mirrors.

2.3 Optical alignment

Precise alignment of the illumination and detection paths are crucial for high quality imaging, and has a pronounced importance for high magnification and high resolution optical systems. The DualMouse SPIM contains two illumination and detection paths. Due to the symmetrical setup of the microscope, we will only describe the alignment of one side, as the same procedure is also applicable to the other side.

2.3.1 Alignment of illumination branches

The two illumination branches start with a common light source, a single mode fiber coupled to laser combiner, and they also share a galvanometric mirror that performs the beam scanning to generate the virtual light-sheet. Likewise shared is a scan lens focusing on the galvo mirror (GM), and the illumination splitter unit (PM, see Section 2.2.2).

Alignment for the illumination arms are done in three steps. First the laser beam is aligned on the first rail that holds the galvo, lens L1, and the splitter unit PM. This is performed by two kinematic mirrors placed between the fiber output and the galvo mirror (not shown on figure). Using these two mirrors it's possible to freely align the beam along all 4 degrees of freedom: translation in two orthogonal directions, and rotation around two orthogonal axes. Beam alignment on the rail is tested by two irises at the two ends of the rail, if the beam passes through both of them we consider it centered and straight on the optical axis.

After the beam is aligned on the first rail, lens L1 and the splitter unit PM are placed in the measured positions to image the galvo mirror on mirror M1 using lenses L1 and

2. DUAL MOUSE-SPIM

L2. Correct positioning of the splitter unit along the rail is crucial, since this will affect the lateral position and tilt of the beam exiting the unit. To some extent, this can also be compensated by adjusting the two mirrors before the galvo mirror, but is avoided if possible as this will also displace the beam from the center of the galvo mirror.

After rough alignment of the illumination arms, when the laser is already coupled in the objective, the fine adjustments are performed based on the image of the beam through the other objective. The beam is visualized by filling the chamber with a 0.1% methylene blue solution. As this solution is fluorescent, and can be excited in a very large range, it is well suited to visualize the beam during adjustment.

Adjusting beam position

Beam position can be adjusted by either translating the beam in a conjugated image plane (I'), or by rotating the beam in a conjugated back focal plane (BFP'). The setup was designed in a way, that BFP' coincides with mirror M1. This mirror is mounted in a gimbal mirror mount, allowing to rotate the mirror exactly around its center, which avoids unwanted translational movements, and results in pure rotation of the beam. Lens L3 is positioned exactly 1 focal length from the mirror, thus acting as a scan lens, and transforming the rotational movements to translation. This translation is further imaged and demagnified by the tube lens L4 and the objective O onto the sample.

Adjusting beam tilt Beam tilt can be adjusted by either rotating the beam in an intermediate image plane (I'), or translating it at the back focal plane (BFP). As mirror M2 is relatively far from the back focal plane, adjusting this will mostly result in translation that will rotate the beam. This movement, however will also introduce translations, and has to be compensated by adjusting mirror M1. The light-sheet, however needs to be tilted by 30° to coincide with the focal plane of the other objective, and this degree of adjustment is not possible with M2. In order to allow for a pure rotation of the light-sheet, we mounted the dichroic mirrors on a linear stage (OptoSigma, TSDH-251C). By translating the dichroic mirror, the illumination laser beam gets translated at the back focal plane, which will result in a pure rotational movement at the sample. Rough alignment of the light-sheet is performed by adjusting the dichroic position while inspecting the light-sheet through a glass window in the chamber. Precise alignment is then done based on the image of the beam visualized in a fluorescent medium.

Adjusting scanning plane angle. After the beam is properly aligned, i.e. it is in focus, and in the center of field of view, it is still necessary to check if the scanning direction is parallel to the imaging plane. It is possible that the beam is in focus in the center position, but when moved up or down it drifts out of focus due to a tilted scanning

angle. This tilt can be compensated by mirror M1, that is placed at the conjugated back focal plane BFP'. Between lenses L3 and L4 a magnified version of the light-sheet will be visible, and the tilt can be checked by placing an alignment target in the optical path while scanning the beam. By tilting mirror M1 up or down, the scanning pattern not only moves up or down, but is also rotated if the mirror surface is not exactly vertical. Since M1 and GM are in conjugated planes, the tilt and offset can be performed independently. The tilt is first fixed by M1 while inspecting the target, and the beam is re-centered by changing the offset on the galvo mirror. Moving the galvo mirror will not introduce tilt, since in this case rotation axis is perpendicular to the reflection plane.

2.3.2 Alignment of detection branches

Since the detection path is equivalent to a wide-field detection scheme, its alignment is much simpler than that of the illumination branches. The only difference is the detection branch merging unit (see subsection 2.2.3.) that features two moving mirrors. This, however doesn't effect the alignment procedure, since the movement direction is parallel to both mirror's surface, meaning that the exact position of the mirrors will not affect the image quality, as long as the mirrors are not clipping the image itself. Stability test were performed to confirm the consistent switching performance of the mirror unit before the final alignment took place (see Sec. 2.5.1).

The final alignment procedure

Positioning the tube lens. The position of the tube lens determines the focal plane the is being imaged on the camera sensor. Ideally, the tube lens' distance from the camera sensor is exactly the tube lens focal length, which will ensure the best imaging performance. If the tube lens distance is not correct, the focal plane will be slightly shifted in the axial direction. Although small shifts will not necessarily have detrimental effect on the image quality, because the light sheet can also be shifted accordingly. Because of the shifted focal and image planes, however, the magnification of the system will be affected, and will change depending on the amount of defocus. For this reason we aim for positioning the tube lens as close to the theoretical position as possible.

Our tube lens is a compound, achromatic lens with a center thickness of 12.5 mm, and edge thickness of 11.3 mm. Its effective focal length is 400 mm which will produce a 50x magnified image. Back focal length is 394.33 mm which we measured form the camera chip, and the lens was positioned at this theoretically optimal position.

Adjusting correction collar. The Nikon 25x objectives used for this setup have a built in correction ring that can be used to correct spherical aberrations resulting from refractive index differences when imaging samples behind a coverslip. This can

2. DUAL MOUSE-SPIM

be also effectively used to correct for any spherical aberrations occurring from imaging through the FEP foil. Although these aberrations are expected to be extremely low, due to the relatively thin, 50 µm foil thickness, and the close matching of refractive index ($n_{FEP} = 1.344$, $n_{H_2O} = 1.333$), for optimal, aberration free image quality it can't be neglected.

The correction collars are adjusted by inspecting a gel suspended fluorescent bead specimen with the microscope, where the beads can act as a reporter of the point spread function of the microscope. The alignment can be performed “live” by inspecting the bead image quality for any aberrations. By gradually changing the correction collar, the ring are minimized on out of focus beads, and the peak intensity is maximized for in focus beads. By moving the correction ring, the focal plane is also slightly shifted, which has to be compensated by shifting the light-sheet correspondingly to coincide with the correct imaging plane.

Adjusting field of view. To allow for proper sampling of the image, we use 50x magnification, which, combined with the 6.5 µm pixel pitch of our sCMOS camera will result in a 0.13 µm pixel size. The full field of view with this magnification is $2048 \times 0.13 = 266.24$ µm. The full field of view the objective provide, are larger than this, at 800 µm. To ensure the best image quality, we align the center of the objective field of view on the camera sensor, since this region has the best optical properties in term of numerical aperture, aberration correction and field flatness.

Field of view alignment can be performed using mirror M4 just before the detection merging unit. To identify the center region of the field of view, diffuse white light is used to illuminate the entire sample chamber, and is imaged on the camera. Then, mirror M4 is adjusted until the top edge of the field of view becomes visible, *i.e.* where the illumination from the chamber is clipped. This will have a circular shape. Then, adjusting the mirror in the orthogonal direction, the left-right position of the field of view can be adjusted, by centering the visible arc on the camera sensor.

After the horizontal direction is centered, vertical centering is performed. This, however can't be centered the same way as the horizontal direction, since for that we would have to misalign the already aligned horizontal position. To determine the center, we move the field of view from the topmost position to the bottom. During this process the number of turns of the adjustment screw is counted (this can be done accurately by using a hex key). After reaching the far end of the field of view, the mirror movement is reversed, and the screw is turned halfway to reach the middle.

2.4 Control unit

The microscope's control and automation is performed by an in-house designed modular microscope control system developed in LabVIEW [95]. The core of the system is a National Instruments cRIO-9068 embedded system that features an ARM Cortex A9 processor, and a Xilinx Zynq 7020 FPGA. Having both chips in the same device is a great advantage, since the main processor can be used to run most of the microscope control software, while the FPGA can be used to generate the necessary output signals in real time and with high precision.

The embedded system is complemented by a high performance workstation that is used to display the user interface of the microscope, and to record the images of the high-speed scientific complementary metal-oxide-semiconductor (sCMOS) camera.

2.4.1 Hardware

Various components need to be synchronized with high precision to operate the microscope: a laser combiner to illuminate the sample; a galvo scanner to generate the light-sheet; stages to move the samples; filter wheel to select the imaging wavelengths; and a camera to detect the fluorescence. For high speed image acquisition, all of these devices have to be precisely synchronized in the millisecond range, and some even in the microsecond range. Although they require different signals to control them, we can split them into three main categories:

digital input	analog input	serial communication
camera exposure	galvo position	filter wheel
laser on/off ($\times 3$)	laser intensity ($\times 3$)	stages ($\times 2$)

All devices are connected to the NI cRIO 9068 embedded system, either to the built in RS232 serial port, or to the digital and analog outputs implemented by C-series expansion modules (NI 9401, NI 9263, NI 9264). The workstation with the user interface is communicating with the embedded system through the network. The only device with a connection to both systems is the camera: the embedded system triggers the image acquisition, while the images are piped to the workstation through a dual CameraLink interface, capable of a sustained 800 MB/s data transfer rate (Figure 2.8).

2.4.2 Software

Being able to precisely control all of the instruments not only relies on the selected hardware, but just as much on the software. Our custom software is developed in LabVIEW, using an object oriented approach with the Actor Framework. The embedded system is responsible for the low level hardware control, for keeping track of the state of all devices,

2. DUAL MOUSE-SPIM

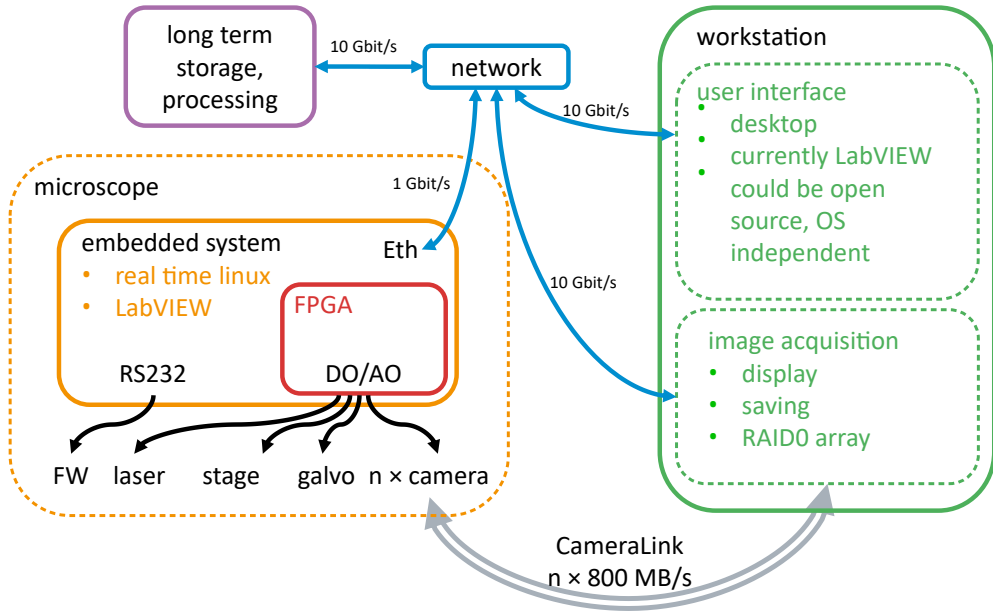


Figure 2.8: Microscope control hardware and software architecture. The embedded system responsible for the hardware control and the workstation are communicating through the network using the WebSocket protocol. The electronic devices of the microscope are either controlled through digital/analog signals, or through serial communication. The camera

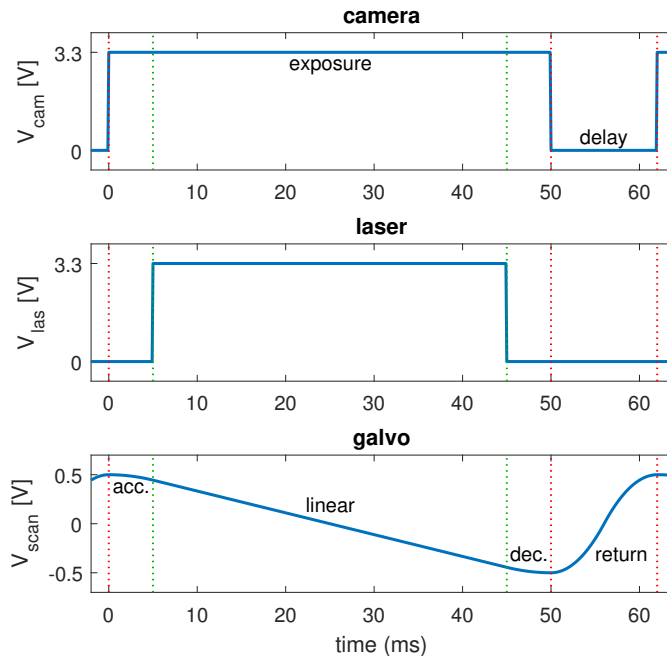


Figure 2.9: Digital and analog control signals. Example traces for recording a single plane with 50 ms exposure time and 12 ms delay. During the exposure of the camera the galvo has 3 sections: acceleration (acc.), linear, and deceleration (dec.). The laser line is synchronized with the galvo linear section to ensure even illumination.

saving the user configurations, and automating and scheduling the experiments. It also offers a Javascript Object Notation (JSON) based application programming interface (API) through WebSocket communication. This is mainly used to communicate with the user interface, however it also offers the possibility of automated control by an external software.

FPGA software

The on-board FPGA is responsible for generating the digital and analog output signals based on the microscope settings (Figure 2.9). To avoid having to calculate all the traces for a whole stack, the main software only calculates a few key parameters of the traces that are necessary to completely describe them. The FPGA then calculates the output signals in real time, and outputs them with microsecond precision.

To describe the traces, we define them as a concatenation of *sections*. Each section has 3 or 5 parameters, depending if their type is digital or analog. Both types have 3 common properties: `value`, `length`, and `type`. The analog sections additionally contain a `dValue` and a `ddValue` element describing the velocity and the acceleration of the signal. This allows us to generate piecewise functions made of second order polynomials.

The `type` element contains information on which value should be updated for the current section. Setting the lowest bit high will update the `value`, setting the second bit high will update the `dValue`, and setting the third bit high will update the `ddValue`. This feature allows to define smooth transitions between the sections, and also to define more complex signals, as long as they are periodic in the second derivative.

2.5 Results

After the design phase, all custom parts were manufactured the EMBL workshop, and microscope was assembled on a NewPort ”!!type!!” optical table (Fig. 2.10). To evaluate the performance of the microscope, we conducted various measurements, concerning the stability and the resolution of the system. The methods and results of these measurements will be presented in this section.

2.5.1 Stability of view switcher unit

As the view switcher unit is a custom designed solution for this microscope, it is necessary to evaluate the effect of the switching on the field of view. Because this is a moving unit, many mechanical imprecisions can introduce a drift in the final image.

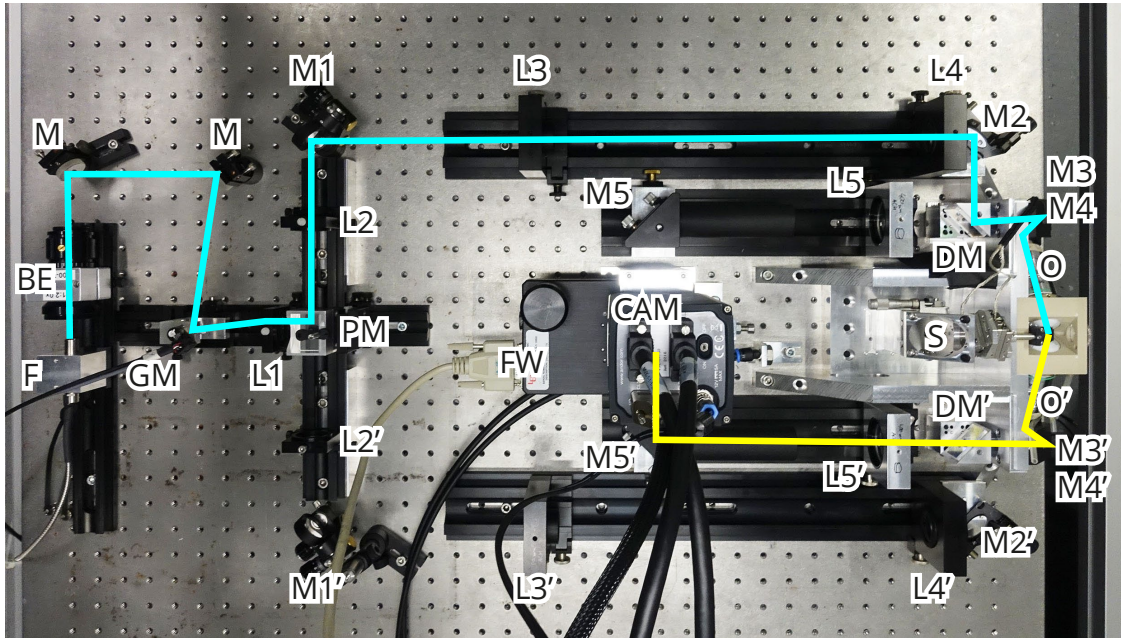
To assess the reproducibility in the movement of the detection branch switching unit, a long term stability test was conducted. To exclude all other factors (such as sample drift), we imaged the opening of two closed irises that were mounted on the detection

2. DUAL MOUSE-SPIM



(a) Front view of the SolidWorks design.

(b) Front view of the microscope.



(c) Top view of the microscope.

Figure 2.10: Completed DualMouse-SPIM. The excitation and emission light paths are depicted with blue and yellow lines respectively. Component numbering corresponds to Figure 2.5. Detection branch merging unit, and mirrors M6 and M6' are underneath the camera and filter wheel. BE – beam expander, CAM – camera, DM – dichroic mirror, F – fiber, FW – filter wheel, L – lens, M – mirror, O – objective, PM – prism mirror, S – stage

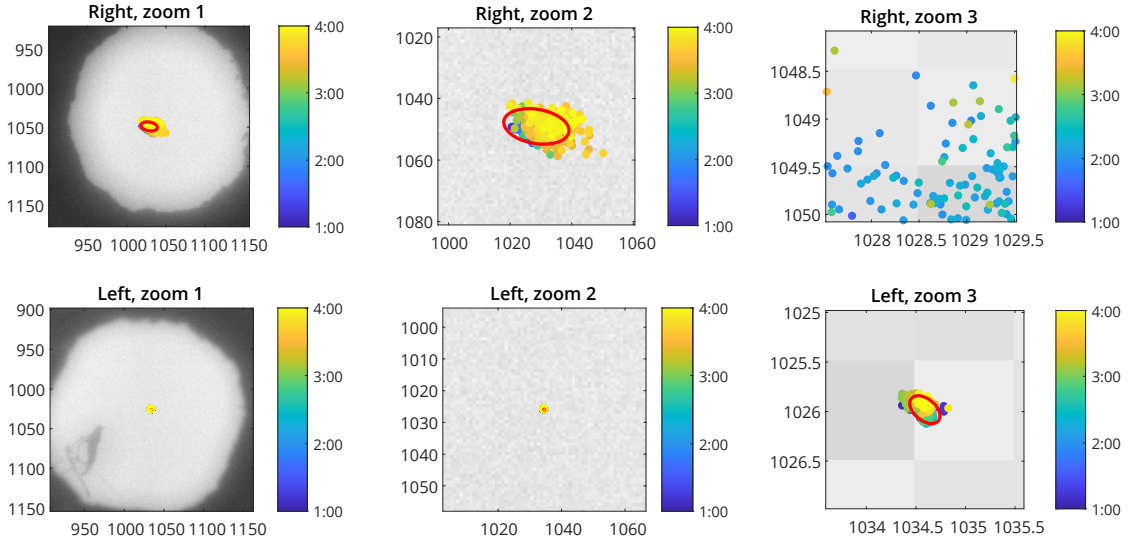


Figure 2.11: Stability measurements of view switcher unit. A closed aperture was imaged on the camera from both views, every 10s, for 4 h. The dot represent the center of each frame, color coded with the time. The red ellipse represents the 95% confidence interval of the measured positions based on principal component analysis. Standard deviations for right view: $\sigma_1 = 4.37 \text{ px}$, $\sigma_2 = 2.26 \text{ px}$; for left view: $\sigma_1 = 0.07 \text{ px}$, $\sigma_2 = 0.04 \text{ px}$.

optical rail. Image formation was done by two achromatic lenses ($f = 75 \text{ mm}$) positioned directly after mirrors M5 and M5'.

The apertures were imaged from both views every 10 seconds, for 4 h, for a total of 1440 images per view, and 2880 switches. The center of the aperture was segmented on all images using Matlab, and tracked to assess any drift occurring during the 4 h time lapse (Figure 2.11). To visualize the uncertainty of the aperture's position, we performed principal component analysis (PCA) on the positions and visualized the results by plotting the 95% confidence ellipse on the images. Although the right view had a significant spread with a standard deviation of 4.37 px and 2.26 px along the long and short axes respectively, the left view was extremely stable, and the standard deviation was only 0.07 px and 0.04 px for the long and short axes respectively. This result implies that there is no conceptual limitation in reaching sub-pixel reproducibility with the view switching unit, although some optimization is still needed for the right view to reach the same stability as the left view.

2.5.2 Characterizing the illumination profile

Since a Gaussian beam is used for illumination, it's intensity profile is dependent on the axial position (Equation 1.18). Although the total intensity at any cross section of the beam is constant, because of the divergent properties, the peak intensity varies. To assess any non-uniformities in the illumination pattern, we measured the illumination beam intensity for each view.

2. DUAL MOUSE-SPIM

To visualize the beam, the chamber was filled with a fluorescent solution (methylene blue solution in distilled water). In order to increase the signal to noise ratio of these images, a long exposure time of 200 ms were used, and 500 images of each beam was averaged, and the background subtracted (Figure 2.12). To determine the beam waist position, we measured the beam thickness (FWHM) for each column of the averaged images, and located the position of the minimal width. The beam width at the waist position for the left view was 3.70 μm , and for the right view it was 3.58 μm (Figure 2.12). We also measured the usable length of the beams (1.3.2). The distance between the points where the beam has expanded by a factor of $\sqrt{2}$ relative to the waist is 95.42 μm for the left view, and 90.35 μm for the right view. This corresponds well to the original requirement of a minimal field of view of 100 μm . Depending on the sample however, the practical field of view can be larger than this, as the camera sensor allows for a field of view of 266 μm .

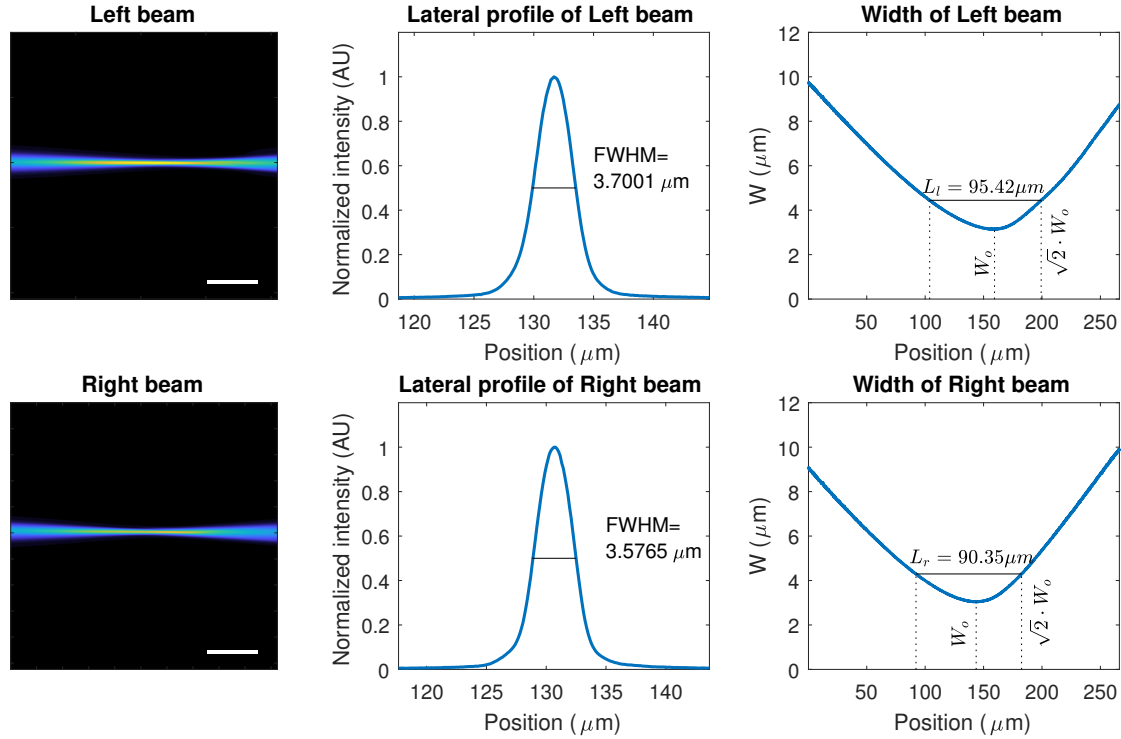


Figure 2.12: Illumination beam profile. Average of 500 stationary beam images for both left (top left) and right objectives (bottom left). Beam intensity profile along the waist of each beam is plotted in the center column. The right column shows the beam width profile of each beam ($1/e^2$).

2.5.3 Resolution and point spread function measurement

In order to establish an ideal, reference PSF, we simulated the theoretical PSF of the microscope with the Gibson-Lanni model [98], using the MicroscPSF Matlab implementation [99]. The advantage of this model is that it accounts for any differences between

2.5 Results

the experimental conditions and the design parameters of the objective, and thus it can simulate any possible aberrations that should arise. The adjustable parameters are the thicknesses (t) and refractive indices (n) of the immersion medium (i), coverslip (g), and sample (s). To simulate the reference PSF, we accounted for the slight mismatch in refractive index between the FEP foil ($n_g = 1.344$) and water ($n_i = 1.33$). The working distance of the objective is 2 mm, while the thickness of the foil is 50 microm.

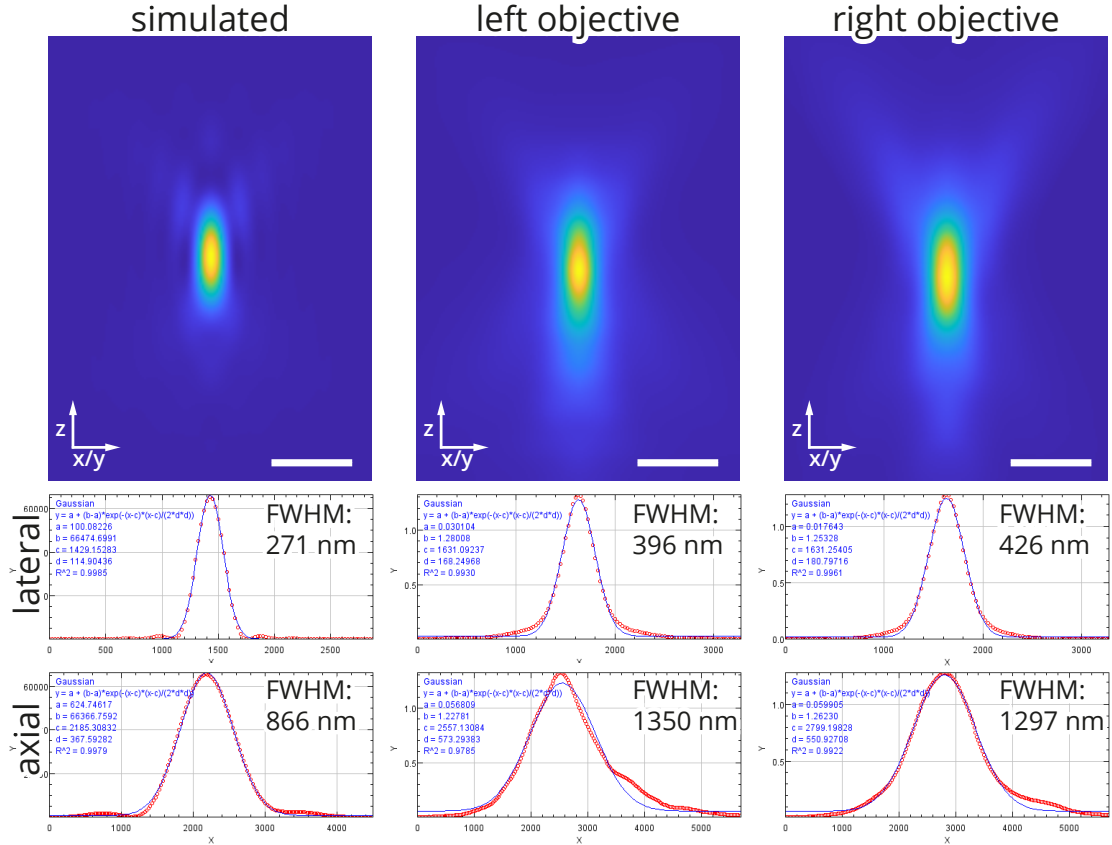


Figure 2.13: Simulated and measured PSF of Dual Mouse-SPIM. Top row: axial sections of simulated and measured point spread functions. Middle row: lateral intensity profile and Gaussian fit. Bottom row: Axial intensity profile and Gaussian fit. Simulations were performed based on the Gibson-Lanni model. Immersion medium and sample refractive index: 1.330, coverslip (FEP foil) refractive index: 1.344, coverslip distance: 1900 μm , coverslip thickness: 50 μm . Excitation wavelength: $\lambda_{ex} = 561 \text{ nm}$. Emission wavelength: $\lambda_{em} = 600 \text{ nm}$. Scale bar: 1 μm .

It is apparent from the simulations that even though the FEP refractive index is almost identical to the refractive index of water, a slight spherical aberration is still present even for the ideal case (Figure 2.13, left). The resolution measured as the FWHM of the intensity profile through the lateral and axial cross sections is 271 nm and 866 nm respectively.

To experimentally measure the resolution of the microscope, and characterize its optical performance, we measured the point spread function using fluorescently labeled beads (TetraSpeck 500 nm, ThermoFisher) suspended in 0.8% GelRite. The gel was loaded in

2. DUAL MOUSE-SPIM

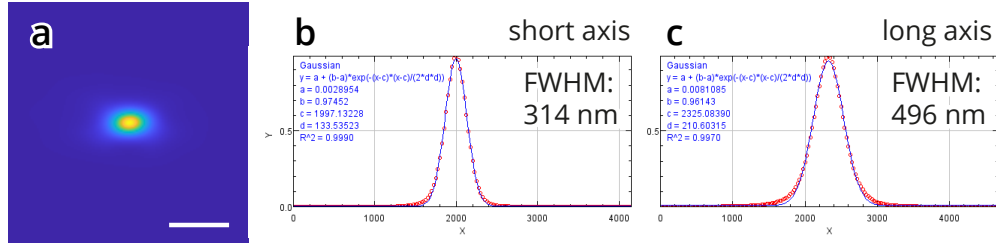


Figure 2.14: Combined PSF of 2 views. (a) The measured PSFs (Figure 2.13) were rotated to their corresponding orientations and multiplied. (b) Gaussian fit along the short axis of the combined PSF; FWHM=314 nm. (c) Gaussian fit along the long axis of the combined PSF; FWHM=496 nm.

glass capillaries and allowed to cool. After the gel solidified, a ~ 1 mm piece was cut off and placed in the microscope sample holder. The beads were imaged from both views using the 561 nm laser line with the 561 long-pass filter.

From both views 12 beads were averaged using Fiji and the 3D PSF estimator of the MOSAICsuite. In order to acquire a more accurate PSF, the averaged bead images were deconvolved with the ideal image of the bead. The results of the deconvolution are shown on Figure 2.13. Similarly to the simulation, we measured the axial and lateral resolutions on the experimental PSFs. For the left view, the measured resolutions were 386 nm in the lateral direction, and 1350 nm in the axial direction. For the right view the lateral resolution was 326 nm, and the axial was 1297 nm.

To estimate the achievable multi-view resolution of the system, we combined the two measured PSFs. First, the PSFs were rotated by $\pm 60^\circ$ to correspond to the objective orientations. The PSF images were then normalized by scaling the maximum to 1, and the two rotated and normalized PSFs were multiplied (Figure 2.14). Resolution of the combined PSF is much improved in all directions, along its shortest axis the FWHM is 314 nm, and along the longest axis the FWHM is 496 nm (Figure 2.14). Both are better than the corresponding resolutions for the single view, especially along the long axis, where the resolution is 2.67 times better. This is almost perfectly matching the theoretically expected increase in the axial direction (compare with subsection 2.1.2).

2.5.4 Resolution inside a *Drosophila melanogaster* embryo

Apart from measuring the point spread function and resolution in an ideal bead sample, we also wanted to know the resolution inside a biological sample, as the tissues usually introduce some aberrations to the light path. Although these aberrations highly depend on the sample, as a worst case scenario, we measured the point spread function inside a *Drosophila melanogaster* embryo. As this specimen is highly opaque and scattering, it gives a good estimate for the upper bound of the resolution.

Instead of the fluorescent beads, we imaged a *Drosophila* embryo expressing H2A-mCherry marking the nuclei, and ASL-YFP marking the centrosomes (Figure 2.15a). As

the centrosomal protein ASL is diffraction limited in size [100], its image gives a good estimate for the point spread function inside the specimen.

Similarly to the bead recordings, 15 centriole images were averaged with the 3D PSF tool of the MOSAIC plugin in Fiji (Figure 2.15c). On the averaged image we measured the resolution by fitting a Gaussian function on the lateral and axial intensity profiles (Figure 2.15d,e), and calculating the FWHM of the fitted Gaussian. The size of the averaged centrioles was 654 nm in the lateral, and 2739 nm in the axial direction.

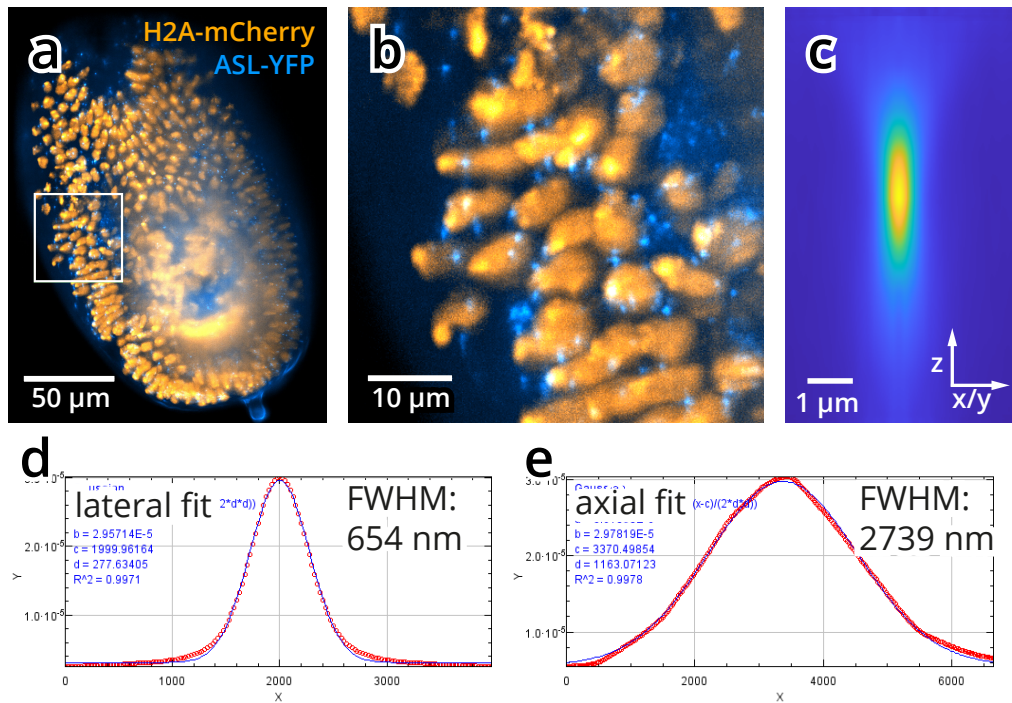


Figure 2.15: Maximum intensity projection of a *Drosophila melanogaster* embryo recording. Maximum intensity projection of a 30 μm thick substack. Orange: nuclei (H2A-mCherry), blue: centrioles (ASL-YFP). 50x magnification. (a) Overview of the embryo. (b) Zoomed in view to the region marked in (a). (c) Average image of 15 centrioles distributed evenly in the embryo. (d) Gaussian fit on the lateral intensity profile of the averaged centrioles; FWHM=654 nm. (e) Gaussian fit on the axial intensity profile of the averaged centrioles; FWHM=2739 nm.

2.5.5 Multi-view imaging of a mouse zygote

2.6 Methods

2.6.1 Bead imaging

For registration and resolution measurements we used TetraSpeck (ThermoFisher, T7279 and T7281) 0.1 μm and 0.5 μm diameter beads. The bead solutions were thoroughly vortexed and sonicated for 5 mins before diluting them 1:100 in distilled water. GelRite (Sigma-Aldrich, G1910) gel was prepared in distilled water at 0.8% concentration with

2. DUAL MOUSE-SPIM

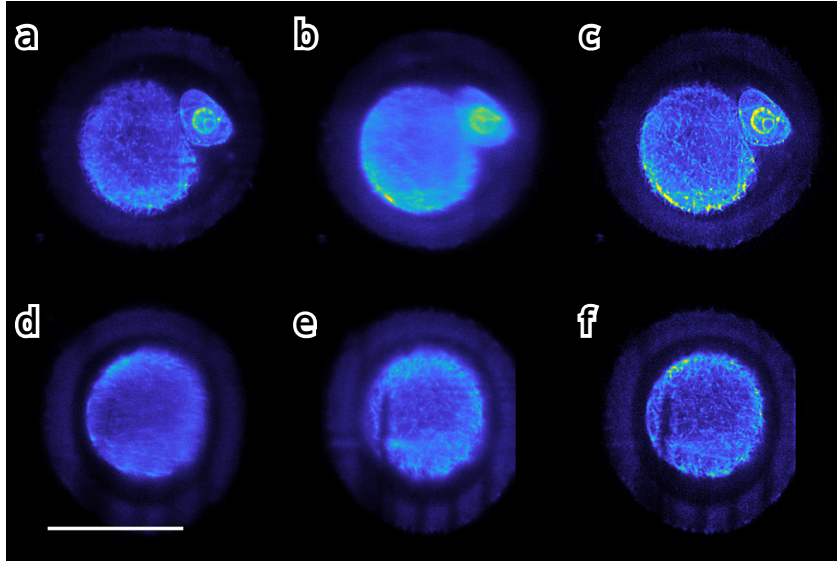


Figure 2.16: Multi-view recording of a mouse zygote. Dual-view imaging was performed on a fixed mouse zygote. Microtubules were stained with Alexa Fluor 488. Top row: view of Left objective. Bottom row: view of Right objective. (a) Raw image from left objective. (b) Rotated view of Right objective. (c) Multi-view deconvolution of stacks (a) and (b). (d) Rotated slice from left objective. (e) Raw image from right objective. (f) Multi-view deconvolution of stacks (d) and (e). Scale bar: 50 μm .

0.1% $\text{MgSO}_4 \cdot 7\text{H}_2\text{O}$ and kept at 70 °C until use.

2.6.2 Mouse zygote imaging

Fixed mouse zygotes labeled with Alexa-488 (microtubules) and Alexa-647 (kinetochores) were kindly provided by Judith Reichmann. Zygotes were transferred to the sample holder, and imaged in PBS. To allow for multi-view reconstruction, a fluorescent beads (TetraSpeck 0.5 μm suspended in GelRite) were placed next to the zygote in the sample holder. After imaging the zygote from both views, the beads were also recorded using the same stack definitions. After data acquisition, the multi-view datasets were registered and deconvolved in Fiji [101] using the Multiview Reconstruction Plugin [102, 103]. The deconvolution was based on a simulated PSF generated in Fiji using the PSF Generator plugin [104] using the Born-Wolf PSF model. $\text{NA}_{\text{ex}} = 0.1$, $\text{NA}_{\text{em}} = 1.1$, $n=1.33$, $\lambda_{\text{ex}} = 488 \text{ nm}$, $\lambda_{\text{em}} = 510 \text{ nm}$.

2.6.3 Drosophila embryo imaging

Drosophila melanogaster embryos expressing fluorescent nuclear (H2A-mCherry) and centriole (ASL-YFP) markers were collected on an agar juice plate and dechorionated in 50% bleach solution for 1 min. After rinsing the bleach with deionized water, the embryos were placed in the sample holder under PBS solution. A small piece of gel containing fluorescent beads were also placed next to the samples to aid in multi-view registration.

2.6.4 Drosophila salivary gland imaging

Salivary glands from third instar larvae expressing fluorescent nuclear (H2A-mCherry) and centriole (ASL-YFP) markers were kindly provided by Ulla-Maj Fiuza. The salivary glands were imaged in PBS, together with a small piece of gel with fluorescent beads.

2. DUAL MOUSE-SPIM

Chapter 3

Image processing for multi-view microscopy

When using any kind of microscopy in research, image processing is a crucial part of the workflow. This is especially true for light-sheet microscopy, since it's capable imaging the same specimen for multiple days, producing immense amounts of data. A single overnight experiment of *Drosophila* development (which is a very typical use-case for light-sheet) can produce multiple terabytes of data. To see the real scales, let's consider the following imaging conditions:

camera	Hamamatsu Orca Flash 4
image size	8 MB
1 stack = 250 planes	2 GB
2 views	4 GB
Time-lapse: 16 h @ 2/min	7.5 TB
n colors	$n \cdot 7.5$ TB

As it is apparent from this table,

3. IMAGE PROCESSING FOR MULTI-VIEW MICROSCOPY

3.1 Multi-view image fusion

3.1.1 Registration

Image based registration

Bead based registration

3.1.2 Transformation

Rigid

Affine

Elastic

3.1.3 Image fusion

Average

Sigmoidal weighted average

Fourier mixing

Huisken had something like this

Wavelet-based fusion

Multi-view deconvolution

[105] Uros thesis [106], [107] Spatially variant deconvolution

3.2 Image compression

Image compression is an important tool for everyday life, however it's rarely used in the context of scientific imaging because of fear of information loss. This preconception is mainly due to the famous blocking artifacts found in many highly compressed JPEG images, however not all image compression algorithms introduce artifacts, and in fact many lossless algorithms exist that would be suitable for such images. Nowadays, when data production is in an exponential growth compression is again in highlight, without it it would be extremely difficult to maintain many scientific projects that produce images at a high data rate.

In this paper I will review the basics of image compression based on Sayood's textbook, Introduction to Data Compression [108]. I will introduce some basics of information theory and entropy, followed by discussing two widely used entropy coding algorithms,

Huffman coding and arithmetic coding. Section 3 will be about transform coding, specifically Discrete Cosine Transform (DCT) and wavelet transform while also touching upon techniques based on differential pulse code modulation. Finally I will show how some of the most widely used image compression standards use these methods to achieve effective image compression.

3.2.1 Entropy coding

Information and Entropy

"For the purpose of data compression it is useful to quantify the amount of *information* contained within a piece of data. The first rigorous definition of information was presented in an extremely influential paper by Shannon, published in two parts in 1948 [109, 110]."

"First, let's define the amount of self-information contained in the outcome of a random experiment:"

$$I(A) = \log_b \frac{1}{P(A)} = -\log_b P(A) \quad (3.1)$$

2 independent events:

$$P(A, B) = P(A) \cdot P(B) \quad (3.2)$$

self-information is additive:

$$I(A, B) = \log_b \frac{1}{P(A, B)} \quad (3.3)$$

$$= \log_b \frac{1}{P(A) \cdot P(B)} \quad (3.4)$$

$$= \log_b \frac{1}{P(A)} + \log_b \frac{1}{P(B)} \quad (3.5)$$

entropy for random variable X average or expected self-information for the random variable

$$H(X) = \sum_i P(A_i)I(A_i) = -\sum_i P(A_i) \log_b P(A_i) \quad (3.6)$$

entropy rate for data source S average information output by the data source

Huffman coding

Huffman coding is a prefix-free, optimal code that is widely used in data compression. It was developed by David A. Huffman as a course assignment on the first ever course on information theory at MIT, and was published shortly afterwards [111]. It is a variable length binary code which assigns different length codewords to letters of different probabilities. It is able to achieve optimal compression, which means the total length of the coded sequence will be minimal.

3. IMAGE PROCESSING FOR MULTI-VIEW MICROSCOPY

Table 3.1: Examples of a random binary code (#1) and a prefix-free binary code (#2). Code #2 is uniquely decodable, while for code #1 it's necessary to introduce boundaries between codewords to be able to distinguish them.

Letter	Code #1	Code #2
a_1	0	10
a_2	11	11
a_3	00	00
a_4	10	010
a_5	111	011

Although it produces a variable length code which can introduce some issues with decoding, it is still uniquely decodable. It achieves this property by using prefix-free codewords, meaning that none of the codewords are prefixes of any other codewords. This property can be exploited when decoding the codeword, since during this procedure the number of bits for the next codeword can not be determined in advance. However if no codeword is a prefix of another codeword, by simply reading the successive bits one by one until we reach a valid codeword, it's possible to uniquely decode the message.

Let's take the example in Table 3.2. Five letters are coded in binary code by Code #1 and by Code #2. Code 1 is not a prefix code, and because of this when reading the encoded sequence we can not be sure when we reach the end of a codeword. Decoding the sequence 0000 for example could be interpreted as 4 letters of a_1 or 2 letters of a_3 .

The Huffman coding procedure is based on two observations regarding optimal and prefix-free codes:

1. For a letter with higher frequency the code should produce shorter codewords, and for letters with lower frequency it should produce longer codewords.
2. In an optimum code, the two least frequent codewords should have the same lengths.

From these statements the first is trivial to see that is correct. If the more frequent letters would have longer codewords than the less frequent letters, the average codeword length (weighted by the probabilities) would be larger than in the opposite case. Thus, more frequent letters must not have longer codewords than less frequent letter.

The second statement at first glance might not be so intuitive, so let's consider the following situation. The two least frequent codewords do not have the same lengths, that is the least frequent is longer. However, because this is a prefix code, the second longest codeword is not a prefix of the longest codeword. This means, if we truncate the longest codeword to the same length as the second longest, they will still be distinct codes and uniquely decodable. This way we have a new coding scheme which requires less space on average to code the same sequence as the original code, from which we can conclude the original code was not optimal. Therefore, for an optimal code, statement 2 must be true.

Table 3.2: Huffman code table.

Letter	Probability	Codeword
a_2	0.4	$c(a_2)$
a_1	0.2	$c(a_2)$
a_3	0.2	$c(a_2)$
a_4	0.1	$c(a_2)$
a_5	0.1	$c(a_2)$

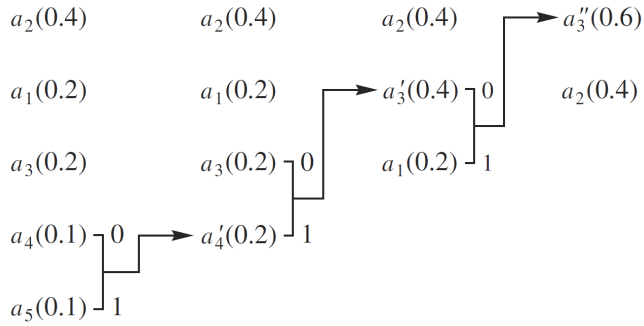


Figure 3.1: Building the binary Huffman tree. The letters are ordered by probability, these will be the final leave of the tree. To join the branches at every iteration we join the two nodes with the smallest probability, and create a new common node with the sum of the probabilities. This process is continued until all nodes are joined in a root node with probability of 1. Now, if we traverse down the tree to each leaf, the codeword will be defined by their position.

To construct such a code, the following iterative procedure can be used. Let's consider an alphabet with five letters $A = [a_1, a_2, a_3, a_4, a_5]$ with $P(a_1) = P(a_3) = 0.2$, $P(a_2) = 0.4$ and $P(a_4) = P(a_5) = 0.1$ (Table 3.2). "The entropy for this source is 2.122 bits/symbol." Let's order the letters by probability, and consider the two least frequent. Since the codewords assigned to these should have the same lengths, "we can assign their codewords as"

$$\begin{aligned} c(a_4) &= \alpha_1 * 0 \\ c(a_5) &= \alpha_1 * 1 \end{aligned}$$

where $c(a_i)$ is the assigned codeword for letter a_i and $*$ denotes concatenation. Now we define a new alphabet A' with only four letters a_1, a_2, a_3, a'_4 , where a'_4 is a merged letter for a_4 and a_5 with the probability $P(a'_4) = P(a_4) + P(a_5) = 0.2$. We can continue this process of merging the letters until all of them are merged and we have only one letter left. Since this contains all of the original letters, its probability is 1. We can represent the end result in a binary tree (see Figure 3.1), where the leaves are the letter of the alphabet, nodes are the merged letters, and the codewords are represented by the path from the root node to each leaf (compare with Table 3.3). "The average length of this

3. IMAGE PROCESSING FOR MULTI-VIEW MICROSCOPY

Table 3.3: Huffman code table.

Letter	Probability	Codeword
a_2	0.4	1
a_1	0.2	01
a_3	0.2	000
a_4	0.1	0010
a_5	0.1	0011

code is”

$$l = 0.4 \times 1 + 0.2 \times 2 + 0.2 \times 3 + 0.1 \times 4 + 0.1 \times 4 = 2.2 \text{ bits/symbol} \quad (3.7)$$

”A measure of the efficiency of this code is its redundancy—the difference between the entropy and the average length. In this case, the redundancy is 0.078 bits/symbol. The redundancy is zero when the probabilities are negative powers of two.”

Arithmetic coding

Although in this case the redundancy of the Huffman code is minimal, however in cases where a few symbols have vary high probability compared to the rest, the redundancy increases. This is simply because even for the most frequent letter the shortest codeword the Huffman code can produce is of length 1.

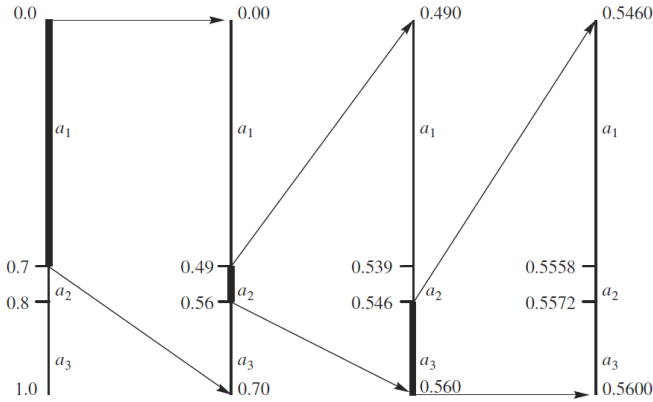
Let’s consider the following example: take alphabet $A = [a_1, a_2]$ with $P(a_1) = 0.95$ and $P(a_2) = 0.05$. The first order entropy for this source is $-0.95 \log 0.95 - 0.05 \log 0.05 = 0.2864$ bits/symbol, however if we assign the Huffman code we will have to use $c(a_1) = 0$ and $c(a_2) = 1$, which means the average length will be 1 bit/symbol. This means in order to code this sequence using a Huffman code, we will need more than 3 times the number of bits promised by the entropy.

To get around this fundamental limitation, a coding scheme must be used which does not use discrete codewords at all. Arithmetic coding is the most well-known example of such a scheme. The idea is due to Peter Elias. He developed it during the same course on information theory in which Huffman developed his coding method, but he never published it.

”In order to distinguish a sequence of symbols from another sequence of symbols we need to tag it with a unique identifier. One possible set of tags for representing sequences of symbols are the numbers in the unit interval $[0,1)$. Because the number of numbers in the unit interval is infinite, it should be possible to assign a unique tag to each distinct sequence of symbols. In order to do this, we need a function that will map sequences of symbols into the unit interval.”

Table 3.4: Example alphabet for arithmetic coding.

Letter	Probability
a_1	0.7
a_2	0.1
a_3	0.2


 Figure 3.2: Arithmetic coding scheme in practice with the alphabet from Table 3.4 on the sequence a_1, a_2, a_3 .

"A straightforward algorithm to arithmetically encode a given input string is the following: Partition the unit interval $[0, 1)$ into sub-intervals and assign one subinterval to each symbol in the input alphabet. The sizes of the sub-intervals are chosen to be proportional to the symbol frequencies. A string of symbols can be encoded by applying this process recursively: The sub-interval from the previous step is subdivided again using the same proportions. Figure 3.2. shows an example of arithmetic coding using the symbol frequencies given in Table 3.4."

This kind of coding although easy to understand, it's actually quite cumbersome to directly implement on a computer, where only a certain floating point precision can be achieved. For real life use this precision is often unsatisfactory, so some extra steps are involved in the coding.

Since after each step the next subinterval is a subset of the previous interval, if the coding interval after a certain number of steps is contained in either the upper or lower half of the unit interval it will remain there for the rest of the coding. We can exploit this fact by rescaling that interval to the unit interval and writing either a 0 or 1 bit to the output depending on the position of the subinterval. By continuing this scheme it's possible to reach arbitrary precision even using a computer.

The decoding process is analogous to encoding. The decoder keeps track of the current lower and upper bounds. It mimics the rescaling operations of the encoder based on the bits of the encoded binary number.

3. IMAGE PROCESSING FOR MULTI-VIEW MICROSCOPY

3.2.2 Transform coding

The methods outlined in the previous section are effective at compressing the data in an optimal way and reaching the first order entropy, however they assume nothing about the structure of the data. For image compression it's important to also consider this, since most images have a relatively high level of autocorrelation, meaning that neighboring values have a high chance of being similar, although not necessarily equal. Transform coding is a technique that by itself does not compress the data, however by exploiting some knowledge of the structure it transforms the data effectively reducing its first order entropy. When regular entropy coding is then performed on the transformed data, because of the reduced first-order entropy, these techniques can achieve a higher rate of compression. At decompression, after decoding the entropy coder, the reverse transformation is applied to reveal the original data. This section will introduce two of the most important algorithms for transform coding, Discrete Cosine Transform and Discrete Wavelet Transform.

Discrete Cosine Transform

Discrete Cosine Transform [112] is closely related to the well known Fourier transform. The main idea behind this is to represent a function by a weighted sum of different sine and cosine functions. This provides a different view, instead of looking at the data in the time domain, we gain information about the frequencies that compose the signal.

"Discrete Cosine Transform is a variant of the discrete Fourier transformation", however instead of making the signal periodic which can introduce large jumps at the edges, the signal is extended in a symmetric way. Since this will give a smooth transition even at the boundaries, the transform does not have to include so many high frequency components. Also, because of the symmetric extension, it's possible to represent the functions only by using the cosine bases, resulting in fewer coefficients. Overall, the DCT is much better suited for compression, than DFT.

The DCT base functions are defined in the following way:

$$c_{i,j} = s_i \cdot \cos \frac{(2j+1)i\pi}{2n} \quad \text{with } s_i = \begin{cases} \sqrt{\frac{1}{n}} & \text{if } i = 0 \\ \sqrt{\frac{2}{n}} & \text{otherwise} \end{cases} \quad (3.8)$$

"The scaling factors are chosen so that the L_2 norm of each basis vector is 1 and so the transform is orthonormal. The inverse transform can therefore be found by simply transposing the transform matrix."

Applying the DCT to two dimensional functions, i.e. images is very similar to the two dimensional Fourier transform. The base functions are the outer products of the 1D base functions (Figure 3.3.), and the transform can actually be performed separately for

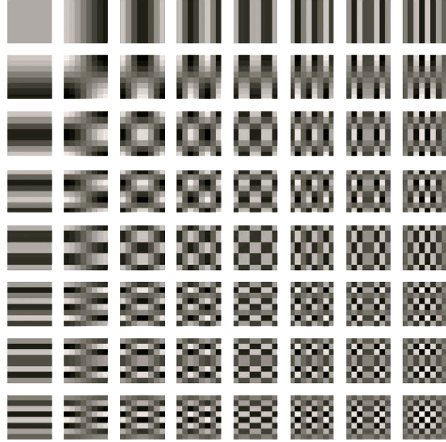


Figure 3.3: Basis functions of the 8×8 2D DCT, computed as the outer product of the 1D basis vectors..

each dimension.

Computation effort in a naive implementation is $O(n^2)$ but since DCT is based on the Fourier transform, an $O(n \log n)$ algorithm is also possible, analogous to the fast Fourier transform. This is still larger than a linear scaling with the data size, which can be very inconvenient. Therefore, in practice the DCT is usually applied to smaller blocks of the image, such as 4×4 , 8 or 16×16 .

Although DCT is an effective way of reducing the first-order entropy, it has a potential shortcoming by its use of floating point arithmetic. Because of the finite machine precision inherent rounding errors will occur, which means the reverse transformation can not generate the exact original data. For many application, such as photography, this still can be acceptable, but for scientific image data lossy compression is generally not accepted.

DCT-like integer-based variants in JPEG-XR, and H.264

Discrete Wavelet Transform

”!!CHANGE THIS!!Methods based on Fourier analysis, such as the DCT introduced in the previous section, give excellent localization in frequency space: They tell us exactly which frequencies occur in the data, which is very useful for data compression. However, they give no spatial localization: They do not tell us where in the signal these frequencies occur. Every DCT base function affect the whole image domain!!UNTIL HERE!!”, which means distinct local structures can have a global effect on the final outcome. In case of an edge for example, it’s necessary to include a high frequency component with a large coefficient, but since every DCT base function has an impact on the whole domain, this will have to be compensated on smoother regions by also increasing the coefficients of other factors. This can negatively impact compression performance.

A solution for this is to use different base functions, namely ones with finite support.

3. IMAGE PROCESSING FOR MULTI-VIEW MICROSCOPY

This way we will not only be able to get information about the frequency, but also about the localization of that frequency in some extent.

”!!!!One option for such a set of local basis functions, and certainly the most popular one, is the multi-resolution analysis based on wavelets. The term “multi-resolution analysis” in the context of wavelets was introduced in the late 1980s by Stéphane Mallat [113], though research on wavelets had been ongoing for several years before that.!!!!”

”The idea behind the wavelet multi-resolution analysis is to build a basis out of translated and scaled versions of one underlying function called the *mother wavelet* ψ . The mother wavelet is non-zero only in a small region, leading to the locality properties. It is translated to cover the whole domain. It also covers only a small frequency band, and is scaled to cover higher or lower frequencies. The family of translated and scaled functions $\psi_{l,i}$ is generated from according to”

$$\psi_{l,i}(t) = \sqrt{2^l} \psi(2^l t - i), \quad l, i \in \mathbb{Z} \quad (3.9)$$

”Incrementing l halves the width of the resulting function, which thus corresponds to a higher frequency band. Changing i moves the function along the x axis. The size of each step scales with the width of the function, defined by l . The normalization factor $\sqrt{2^l}$ is chosen so that the L_2 norm stays constant. The mother wavelet can be chosen so that the $\psi_{l,i}$ are pairwise orthogonal and thus form a basis of some function space. However, representing a function in this basis will generally require an infinite number of basis functions $\psi_{l,i}$: To represent a constant component, i.e. content of frequency zero, the wavelet must be infinitely scaled. To address this, it is necessary to introduce an additional scaling function ϕ which complements the wavelet. It is scaled and translated the same way as the mother wavelet.”

The oldest wavelets are the Haar wavelets, and because of their simplicity, they provide a good example on how wavelet transformation works. The Haar wavelet scaling ϕ and wavelet ψ functions are the following:

$$\phi(t) = \begin{cases} 1 & \text{if } 0 \leq t < 1 \\ 0 & \text{otherwise} \end{cases} \quad (3.10)$$

$$\psi(t) = \begin{cases} -1 & \text{if } 0 \leq t < \frac{1}{2} \\ 1 & \text{if } \frac{1}{2} \leq t < 1 \\ 0 & \text{otherwise} \end{cases} \quad (3.11)$$

”Clearly, all wavelet functions $\psi_{l,i}$ are orthogonal. Additionally, the scaling functions $\phi_{l,i}$ at a fixed level i are orthogonal. The scaling functions $\phi_{l,i}$ are also orthogonal to the wavelet functions $\psi_{k,i}$, $k \geq l$ at the same and all finer levels.”

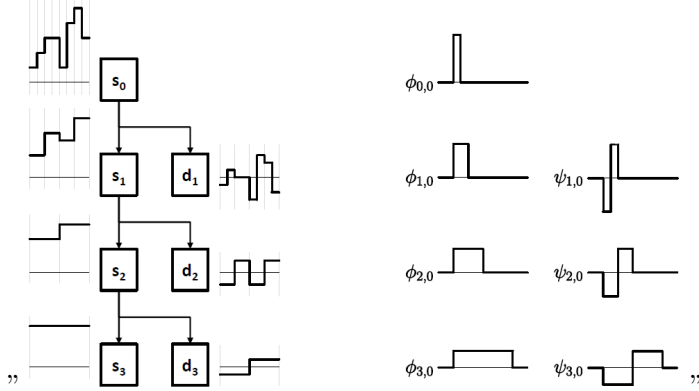


Figure 3.4: Multi-resolution wavelet decomposition, using the Haar wavelets as an example. Left: decomposition to multiple levels of low pass and high pass coefficients corresponding to the scaling and the wavelet functions respectively. Right: some of the base wavelet functions used for the decomposition.

"Figure 3.4. (left) schematically shows the decomposition of a signal into low-pass components corresponding to the scaling function, and high-pass components corresponding to the wavelet. The signal s_0 can be represented by the translated scaling function at a finer scale l_0 , "which can be decomposed to the sum of a coarser approximation s_1 corresponding to the scaling function and the detail part d_1 corresponding to the wavelet functions. This decomposition to a sum of coarser approximation and detail can be continued multiple times, thus resulting in the previously mentioned multi-resolution analysis.

Of course, for image compression applications, it is desirable to extend this transformation to a 2D version, that can be applied to the images before performing the arithmetic coding. Similarly to the DCT, the wavelet transform is also separable, and can be performed as a sequence of 1D transforms along different directions. Separable in a sense, that it does not matter in which order the individual 1D DWTs are applied to get the same 2D transformation.

JPEG [114], JPEG-LS [115] and JPEG2000 [116]

3. IMAGE PROCESSING FOR MULTI-VIEW MICROSCOPY

3.2.3 Differential pulse code modulation / LOCO-I?

3.3 Noise in light microscopy images

3.3.1 Photon shot noise

3.3.2 Camera noise

CCD

EM-CCD

sCMOS

3.3.3 Variance stabilization

Chapter 4

Real-time, GPU accelerated image processing pipeline

4.1 GPU architecture

CUDA [117]

4.2 Live fusion

4.2.1 MuVi-SPIM

4.2.2 Bead based registration

4.3 B³D image compression

B³D image compression high content screening [118–120] light-sheet (Sec. 1.3) single molecule localization microscopy [121–123] data handling is bottleneck [124–126] lossy compression not recommended for microscopy [127] KLB [128] jpeg compression so loss is not perceptible [108] big data viewer [129] Fiji [101]

FLIC [130] SFALIC [131] FELICS [132] Treib terrain editing [133] Treib turbulence [134] square root compression [135] noise and bias in square root compression [136] quantization [137] Anscombe [138] optimal inverse Anscombe [139, 140] optimal inverse generalized Anscombe [141]

4. REAL-TIME, GPU ACCELERATED IMAGE PROCESSING PIPELINE

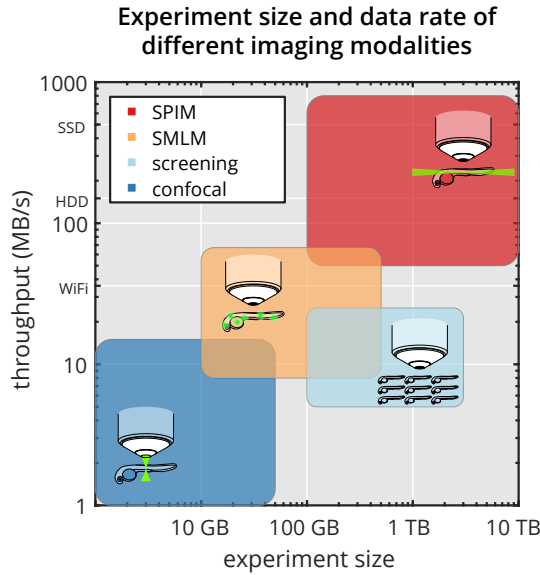


Figure 4.1: Experiment sizes and data rate of different imaging modalities. Comparison of single-plane illumination microscopy (SPIM, red rectangle), high-content screening (light blue), single molecule localization microscopy (SMLM, orange) and confocal microscopy (blue) by typical experiment size and data production rate (see also Table B1).

4.3.1 Data sizes in microscopy

4.3.2 Compression algorithm

4.3.3 Lossless compression performance

4.3.4 Swapping for WNL

4.3.5 Benchmarking

4.4 Noise dependent lossy compression

4.5 Methods

Compression benchmarking

For all presented benchmarks, TIFF and JPEG2000 performance was measured through MATLAB's imwrite and imread functions, while KLB and B³D performance was measured in C++. All benchmarks were run on a computer featuring 32 processing cores (2×Intel Xeon E5-2620 v4), 128 GB RAM and an NVIDIA GeForce GTX 970 graphics processing unit. Read and write measurements were performed in RAM to minimize I/O overhead, and are an average of 5 runs.

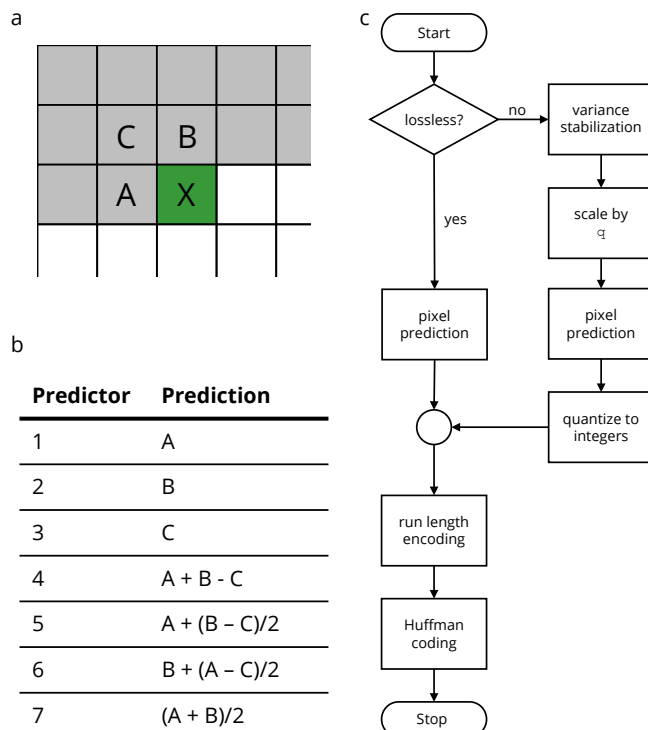


Figure 4.2: B³D algorithm schematics. (a) Prediction context for pixel X, the next sample to be encoded. Three neighboring pixels are considered: left (A), top (B) and top left (C) neighbors. (b) Lossless JPEG predictors for X, based on the context showed in (a). The first three predictors are one-dimensional, while the rest are two-dimensional. Using a two dimensional predictor while increases complexity slightly, also increases the achievable compression ratio. We found that for fluorescence microscopy images predictor 7 performs best, hence its inclusion in the B³D algorithm. (c) Complete algorithm flowchart depicting the main stages of the compression. First, if the result should be lossless, pixel prediction is performed on the original image values. If within noise level mode is selected, the image noise is stabilized first (see "Supplementary Note"), which is then scaled by the quantization step q. Prediction is performed, and the prediction errors are rounded to the nearest integer. The prediction errors for both lossless and lossy modes are then run-length encoded, and finally Huffman coding is applied to effectively reduce data size. The output of the Huffman coder is saved as the compressed file.

4. REAL-TIME, GPU ACCELERATED IMAGE PROCESSING PIPELINE

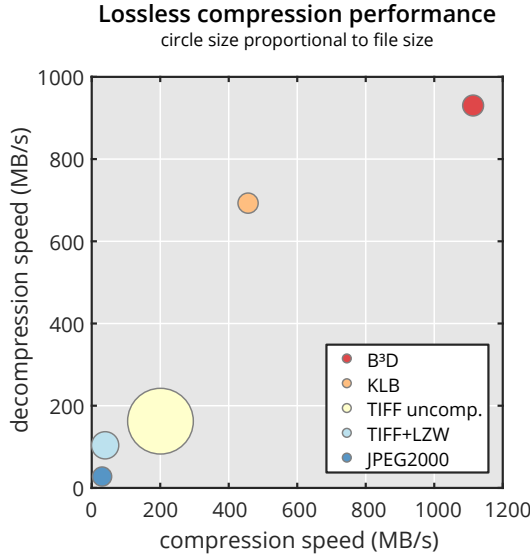


Figure 4.3: Lossless compression performance. Performance comparison of our B³D B³D compression algorithm (red circle) vs. KLB (orange), uncompressed TIFF (light yellow), LZW compressed TIFF (light blue) and JPEG2000 (blue) regarding write speed (horizontal axis), read speed (vertical axis) and file size (circle size). (see also Table B2).

Light-sheet imaging

Drosophila embryos were imaged in our MuVi-SPIM setup [45] using the electronic confocal slit detection (eCSD) [75]. Embryos were collected on an agar juice plate, and dechorionated in 50% bleach solution for 1 min. The embryos were then mounted in a shortened glass capillary (Brand 100 µl) filled with 0.8% GelRite (Sigma-Aldrich), and pushed out of the capillary to be supported only by the gel.

3D nucleus segmentation

3D nucleus segmentation of *Drosophila* embryos was performed using Ilastik [142]. The original dataset was compressed at different quantization levels, then upsampled in z to obtain isotropic resolution. To identify the nuclei, we used the pixel classification workflow, and trained it on the uncompressed dataset. This training was then used to segment the compressed datasets as well. Segmentation overlap was calculated in Matlab ("Supplementary Code") using the Sørensen–Dice index [143, 144]:

$$QS = 2 |A \cap B| / (|A| + |B|) \quad (4.1)$$

where the sets A and B represent the pixels included in two different segmentations.

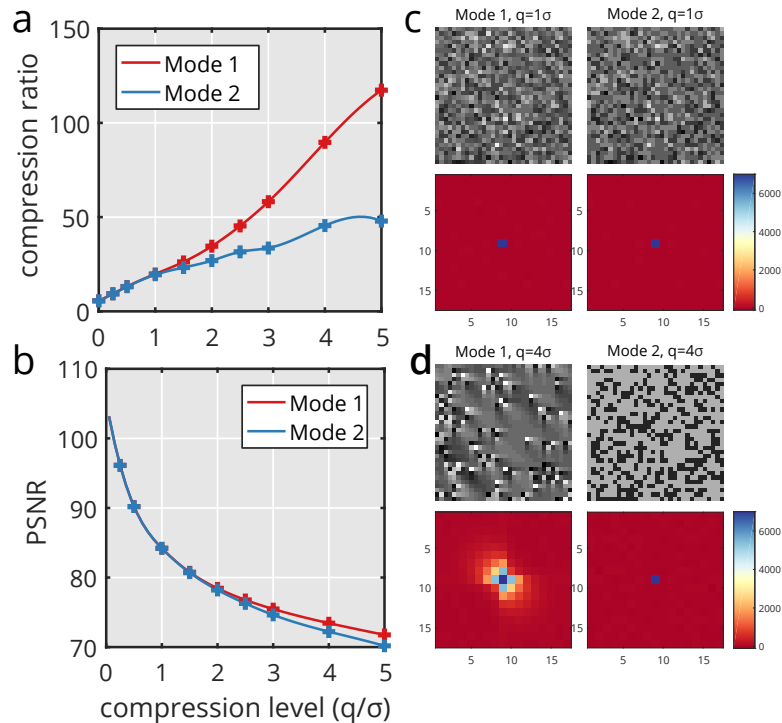


Figure 4.4: Options for noise dependent lossy compression. Comparing Mode 1 (prediction then quantization) and Mode 2 (quantization then prediction) of noise dependent lossy compression in terms of compression ratio, peak signal to noise ratio (PSNR) and spatial correlations introduced to random noise. (a) Compression ratio as a function of the quantization step for Mode 1 and Mode 2. (b) PSNR as a function of the quantization step for Mode 1 and Mode 2. (c, d) Random noise was compressed at various quantization steps both for Mode 1 and Mode 2. Autocorrelation was calculated for the compressed images to see whether the compression introduces any spatial correlation between the pixels. For $q=1\sigma$ both modes are free of correlation (c, top: compressed images, bottom: autocorrelation), however, for $q=2\sigma$ Mode 1 exhibits a correlation pattern (d, top left: compressed image, bottom left: autocorrelation) that is not present in Mode 2 (d, top right compressed image, bottom right: autocorrelation). For more discussion, see “Supplementary Note”.

4. REAL-TIME, GPU ACCELERATED IMAGE PROCESSING PIPELINE

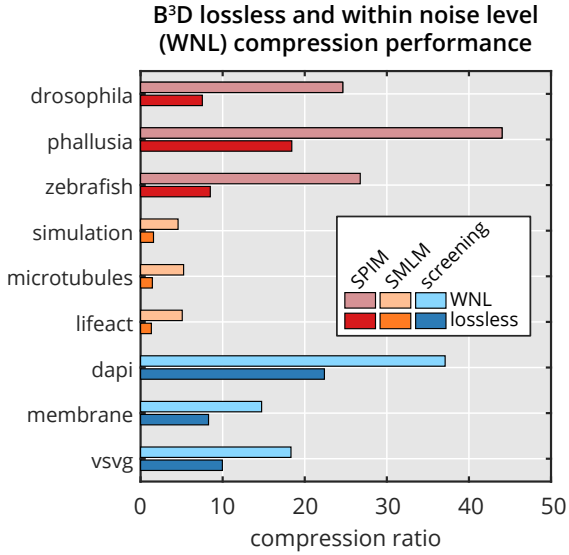


Figure 4.5: Within noise level compression performance. WNL compression performance compared with lossless performance for 9 different dataset representing 3 imaging modalities (SPIM, SMLM, screening). Compression ratio = original size / compressed size. For description of datasets see Table B3 in Appendix B.

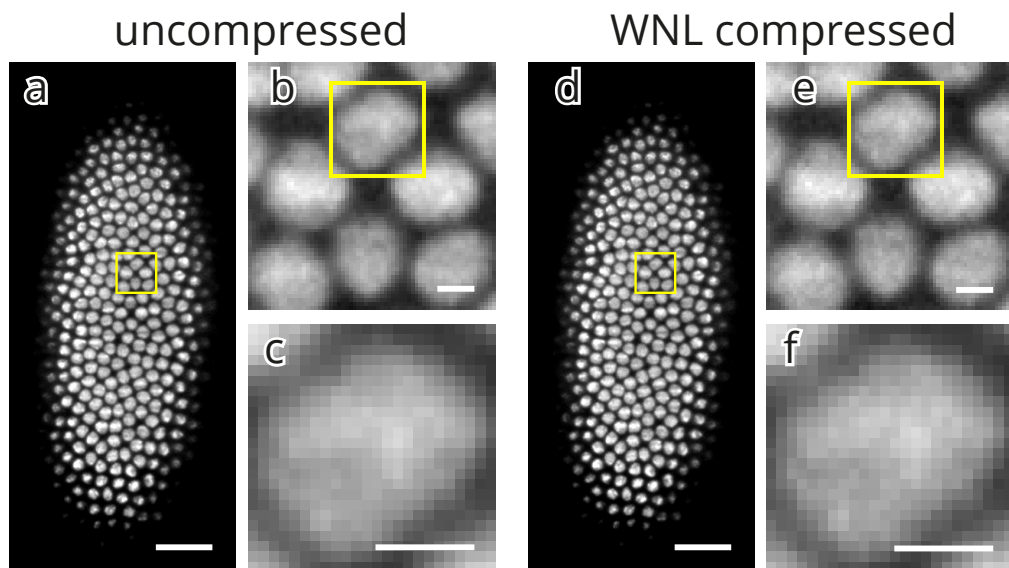


Figure 4.6: Image quality of a WNL compressed dataset. WNL compression performance compared with lossless performance for 9 different dataset representing 3 imaging modalities (SPIM, SMLM, screening). Compression ratio = original size / compressed size. For description of datasets see Table B3.

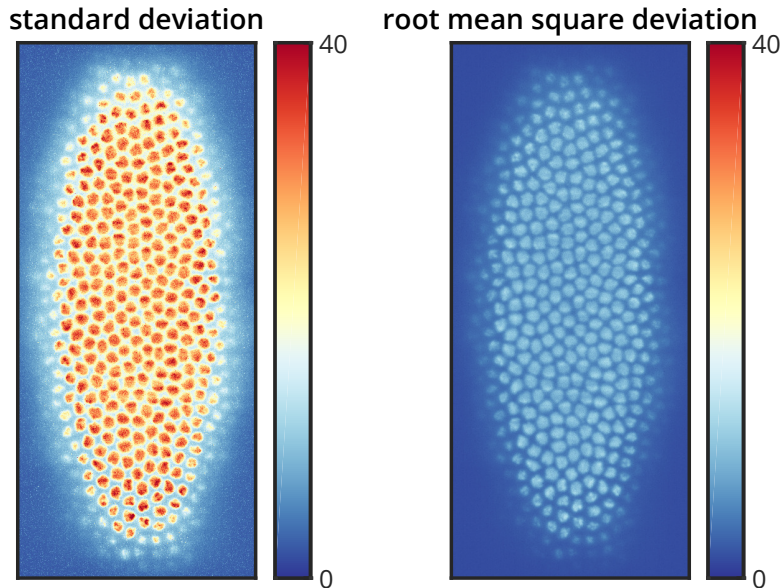


Figure 4.7: Compression error compared to image noise. To compare the difference arising from WNL compression to image noise, we imaged a single plane 100 times in a *Drosophila melanogaster* embryo expressing H2Av-mCherry nuclear marker at 38 ms intervals. The whole acquisition took 3.8 s, for which the sample can be considered stationary. To visualize image noise, the standard deviation was calculated for the uncompressed images (left). All images were then WNL compressed, and the root mean square deviation was calculated compared to the uncompressed images (right). The root mean square deviation on average is 3.18 times smaller than the standard deviation of the uncompressed images.

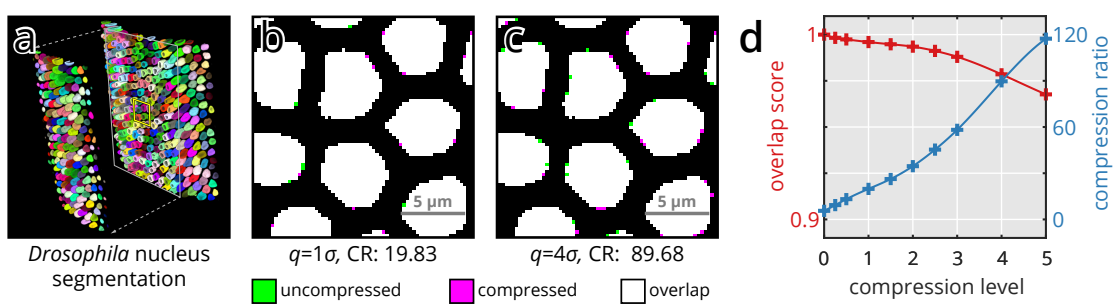


Figure 4.8: Influence of noise dependent lossy compression on 3D nucleus segmentation. A *Drosophila melanogaster* embryo expressing H2Av-mCherry nuclear marker was imaged in MuVi-SPIM [45], and 3D nucleus segmentation was performed ("Online Methods") (a). The raw data was subsequently compressed at increasingly higher compression levels, and segmented based on the training of the uncompressed data. To visualize segmentation mismatch, the results of the uncompressed (green) and compressed (magenta) datasets are overlaid in a single image (b, c; overlap in white). Representative compression levels were chosen at two different multiples of the photon shot noise, at $q=1\sigma$ (b) and $q=4\sigma$ (c). For all compression levels the segmentation overlap score ("Online Methods") was calculated and is plotted in (g) along with the achieved compression ratios.

4. REAL-TIME, GPU ACCELERATED IMAGE PROCESSING PIPELINE

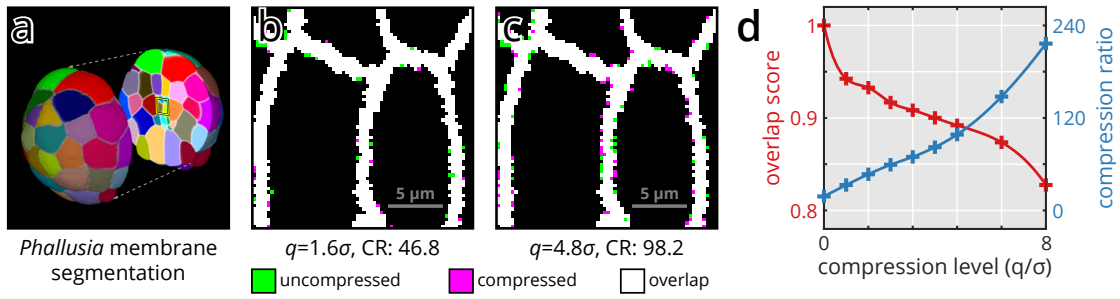


Figure 4.9: Influence of noise dependent lossy compression on 3D membrane segmentation. A *Phallusia mammillata* embryo expressing PH-citrine membrane marker was imaged in MuVi-SPIM [45], and 3D membrane segmentation was performed (“Supplementary Methods”) (a). The raw data was subsequently compressed at increasingly higher compression levels, and segmented using the same settings as the uncompressed data. To visualize segmentation mismatch, the results of the uncompressed (green) and compressed (magenta) datasets are overlaid in a single image (b, c; overlap in white). Representative compression levels were chosen at two different multiples of the photon shot noise, at $q=1.6\sigma$ (b) and $q=4.8\sigma$ (c). For all compression levels the segmentation overlap score (“Supplementary Methods”) was calculated and is plotted in (d) along with the achieved compression ratios.

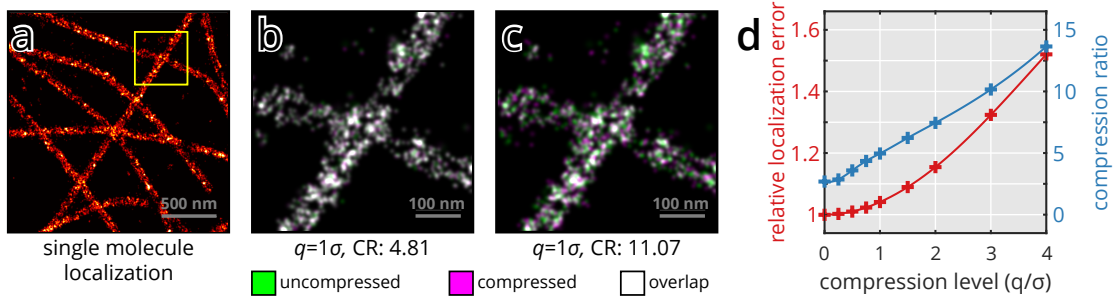


Figure 4.10: Influence of noise dependent lossy compression on single-molecule localization. Microtubules, immunolabeled with Alexa Fluor 647 were imaged by SMLM (a). The raw data was compressed at increasingly higher compression levels, and localized using the same settings as the uncompressed data. To visualize localization mismatch, the results of the uncompressed (green) and compressed (magenta) datasets are overlaid in a single image (b, c; overlap in white). Two representative compression levels were chosen at $q=1\sigma$ (b) and $q=4\sigma$ (c). To assess the effects of compression on localization precision, a simulated dataset with known emitter positions was compressed at various levels. For all compression levels the relative localization error (normalized to the Cramér–Rao lower bound) was calculated and is plotted in (d) along with the achieved compression factors.

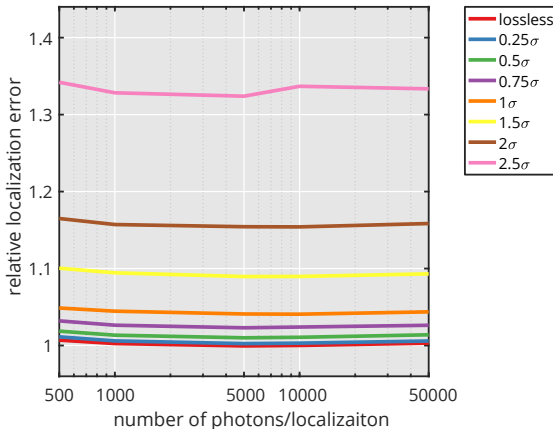


Figure 4.11: Change in localization error only depends on selected quantization step. We simulated multiple datasets (“Supplementary Methods”) with different average photon numbers per localization. Background was kept at a constant average of 20 photons/pixel. Datasets were compressed at multiple compression levels (see legend), and localization error relative to the Cramér-Rao lower bound was calculated. The relative localization error only depends on the compression level, and not on the signal to background illumination ratio.

3D membrane segmentation

Raw MuVi-SPIM recordings of *Phallusia mammillata* embryos expressing PH-citrine membrane marker were kindly provided by Ulla-Maj Fiura (EMBL, Heidelberg). Each recording consisted of 4 views at 90 degree rotations. The views were fused using an image based registration algorithm followed by a sigmoidal blending of the 4 views. The fused stack was then segmented using the MARS algorithm [145] with an hmin parameter of 10. The raw data (all 4 views) was compressed at different levels, and segmented using the same pipeline. Segmentation results were then processed in Matlab to calculate the overlap score for the membranes using the Sørensen–Dice index (“Supplementary Code”).

Single-molecule localization imaging

In order to visualize microtubules, U2OS cells were treated as in [146] and imaged in a dSTORM buffer [147]. In brief, the cells were permeabilized and fixed with glutaraldehyde, washed, then incubated with primary tubulin antibodies and finally stained with Alexa Fluor 647 coupled secondary antibodies. The images were recorded on a home-built microscope previously described [146], in its 2D single-channel mode.

Single-molecule localization data analysis

Analysis of single-molecule localization data was performed on a custom-written MATLAB software as in [148]. Pixel values were converted to photon counts according to measured offset and calibrated gain of the camera (EMCCD iXon, Andor). The back-

4. REAL-TIME, GPU ACCELERATED IMAGE PROCESSING PIPELINE

ground was estimated with a wavelet filter [149], background-subtracted images were thresholded and local maxima were detected on the same images. 7-pixel ROIs around the detected local maxima were extracted from the raw images and fitted with a GPU based MLE fitter [150]. Drift correction was performed based on cross-correlation. Finally, images were reconstructed by filtering out localizations with a high uncertainty ($>30\text{ nm}$ and large PSF ($>150\text{ nm}$) and Gaussian rendering.

Simulation of single-molecule localization data

Single molecule localization data was simulated in Matlab ("Supplementary Code") by generating a grid of pixelated Gaussian spots with standard deviation of 1 pixel. With a pixel size of a 100 nm, this corresponds to a FWHM of 235.48 nm. The center of each spot was slightly offset from the pixel grid at 0.1 pixel increments in both x and y directions. To this ground truth image a constant value was added for illumination background, and finally Poisson noise was applied to the image. This process was repeated 10000 times to obtain enough images for adequate accuracy.

Code availability

Code used for analyzing data, B³D source code and compiled binaries, including a filter plugin for HDF5, is available for download at <https://git.embl.de/balazs/B3D>.

Chapter 5

Discussion

5.1 New scientific results

Thesis I. *I have designed and constructed a new light-sheet microscope suitable for high sensitivity imaging of delicate samples. A novel arrangement of two high numerical aperture objectives in 120 degrees allows for near isotropic resolution while increasing light collection efficiency by a factor of two.*

Corresponding publications: [J3], [J2], [J1]

Live imaging of light sensitive specimens, such as a developing mouse embryo is a challenging task

Thesis II. *I have developed a GPU-based image processing pipeline for multi-view light-sheet microscopy that enables real time fusion of opposing views.*

Corresponding publications: [C1], [C2], [C3]

Thesis III. *I have developed a new image compression algorithm that enables noise dependent lossy compression of light microscopy images, and can reach a compression ratio of 100 fold while preserving the results of downstream data analysis steps.*

Corresponding publications: [J4], [C1], [C2], [C3]

All microscopy images contain inherent noise, that is

Thesis IV. *I have developed a new GPU-based image compression library, B^3D , that implements the algorithm described in Thesis III, and allows for real time compression of microscopy images with a throughput of up to 1 GB/s.*

Corresponding publications: [J4], [C1], [C2], [C3]

B^3D is an efficient, GPU-based image compression library allowing lossless and noise dependent lossy compression of microscopy images. Since many high-speed microscopy

5. DISCUSSION

methods generate immense amounts of data, easily reaching terabytes per experiment, image compression is especially important to efficiently deal with such datasets.

Acknowledgements

ACKNOWLEDGEMENTS

Appendix A

Bill of materials

Bill of Materials

Optical components

- Lenses
 - 2×Nikon CFI75 Apo LWD 25x/1.10w water dipping objectives
 - 2×Nikon ITL200 200 mm tube lens
 - 2×200 mm x 25 mm Dia. achromatic lens (Edmunds Optics, #47-645)
 - 2×400 mm x 40 mm Dia. achromatic lens (Edmunds Optics, #49-281)
 - 3×75 mm x 25 mm Dia. achromatic lens (Edmunds Optics, #47-639)
 - SILL 112751 1:2 beam expander
- Filters
 - 2×BrightLine quad-edge dichroic beam splitter (Semrock, Di03-R405/488/561/635-t3-25x36)
 - EdgeBasic 488 nm long pass filter (Semrock, BLP01-488R-25)
 - BrightLine 525/50 band pass filter (Semrock, FF03-525/50-25)
 - EdgeBasic 561 nm long pass filter (Semrock, BLP02-561R-25)
 - RazorEdge 647 nm long pass filter (Semrock, LP02-647RU-25)
- Mirrors
 - 6×1” Broadband Dielectric Elliptical Mirror (Thorlabs, BBE1-E03)
 - 2×30 mm Broadband 1/10λ Mirror (OptoSigma, TFMS-30C05-4/11)
 - 10 Pack of 1” Protected Silver Mirrors (Thorlabs, PF10-03-P01-10)
 - Knife-Edge Right-Angle Prism Dielectric Mirror (Thorlabs, MRAK25-E02)

Mechanical components

- 40 mm travel range pneumatic cylinder (Airtac, HM-10-040)
- 5/2-way electric valve (Airtac, M-20-510-HN)
- 2×25 mm extended contact bearing steel stage (OptoSigma, TSDH-251C)
- 30x90 mm stainless steel slide (OptoSigma, IPWS-F3090)
- close proximity gimbal mirror mount (Thorlabs, GMB1/M)
- 30 mm cage elliptical mirror mount (Thorlabs, KCB1E)

APPENDIX A

Custom parts

All parts are (anodized) aluminium, unless stated otherwise.

- 2×mirror holder block
- Front plate for objective, chamber and mirror mounting
- Imaging chamber (PEEK)
- Wedge ring and matching threaded ring to fasten objectives
- Camera bridge
- Illumination splitter unit
- adapter plates to mount stages

Electronics

- Embedded system (National Instruments, cRIO-9068) equipped with:
 - 2×C series digital I/O card (NI 9401)
 - 1×C Series 100 kS/s 4-channel Voltage Output Module (NI 9263)
 - 1×C Series 25 kS/s 16-channel Voltage Output Module (NI 9264)
- Omicron SOLE-3 laser combiner, with 488, 561 and 638 nm laser lines
- Andor Zyla 4.2 sCMOS Camera
- Galvanometric scanner mirror (Cambridge Technology, 6210B)
- 6 position filter wheel (Ludl Electronic Products, 96A361)
- Filter wheel controller unit (Ludl Electronic Products, MAC5000)
- 2 piezoelectric stages (Nanos Instruments, LPS-30-30-1-V2_61-S-N)
- 2 stage controller boards (Nanos Instruments, BMC101)

Appendix B

Appendix B

Data sizes in microscopy

Lossless compression performnace

Benchmarking datasets

APPENDIX B

	imaging device	image size	frame rate	data rate	data size
SPIM	2x sCMOS camera (e.g. Hamamatsu ORCA Flash4.0)	2048x2048	50/s	800 MB/s	10 TB
SMLM	2x EMCCD camera (e.g. Andor iXon Ultra 897)	512x512	56/s	56 MB/s	500 GB
screening	CCD camera (e.g. Hamamatsu ORCA-R2)	1344x1024	8.5s/	22 MB/s	5 TB
confocal	Zeiss LSM 880, 10 channels	512x512	5/s	12.5 MB/s	50 GB

Table B1: Data sizes in microscopy. Typical devices used for confocal microscopy, high-content screening, single-molecule localization microscopy and light-sheet microscopy and their data production characteristics. Data visualized on Figure 4.1

	write speed	read speed	CR	file size
B³D	1,115.08 MB/s	928.97 MB/s	9.861	100%
KLB	283.19 MB/s	619.95 MB/s	10.571	93.28%
JPEG2000	31.94 MB/s	26.38 MB/s	11.782	83.69%
JPEG2000	202.32 MB/s	161.08 MB/s	1.00	986.1%
TIFF + LZW	40.85 MB/s	102.37 MB/s	5.822	169.37%

Table B2: Lossless compression performance. B³D is compared with various popular lossless image compression methods regarding write speed, read speed and compression ratio (original size / compressed size). Data visualized on Figure 4.3.

Dataset name	Imaging modality	Description	Size (MB)
drosophila	SPIM	dataset acquired in MuVi-SPIM of a Drosophila melanogaster embryo expressing H2Av-mCherry nuclear marker	494.53
zebrafish	SPIM	dataset acquired in MuVi-SPIM of a zebrafish embryo expressing b-actin::GCaMP6f calcium sensor	2,408.00
phallusia	SPIM	dataset acquired in MuVi-SPIM of a Phallusia mammillata embryo expressing PH-citrine membrane marker	1,323.88
simulation	SMLM	MT0.N1.LD-2D simulated dataset of microtubules labeled with Alexa Fluor 647 from SMLMS 2016 challenge	156.22
microtubules	SMLM	microtubules immuno-labeled with Alexa Fluor 674-bound antibodies in U2OS cells	1,643.86
lifeact	SMLM	actin network labeled with LifeAct-tdEOS in U2OS cells	3,316.15
dapi	screening	wide field fluorescence images of DAPI stained HeLa Kyoto cells [151]	1,005.38
vsvg	screening	wide field fluorescence images of CFP-tsO45G proteins in HeLa Kyoto cells [151]	1,005.38
membrane	screening	wide field fluorescence images of membrane localized CFP-tsO45G proteins labeled with AlexaFluor647 in HeLa Kyoto cells [151]	1,005.38

Table B3: Datasets used for benchmarking compression performance.

APPENDIX B

References

The author's publications

- [J1] Patrick Hoyer et al. “Breaking the diffraction limit of light-sheet fluorescence microscopy by RESOLFT”. *Proceedings of the National Academy of Sciences* 113.13 (Mar. 2016), pp. 3442–3446. DOI: [10.1073/pnas.1522292113](https://doi.org/10.1073/pnas.1522292113) (cit. on pp. 16, 17, 77).
- [J2] Petr Strnad et al. “Inverted light-sheet microscope for imaging mouse pre-implantation development”. *Nature Methods* 13.2 (Feb. 2016), pp. 139–142. DOI: [10.1038/nmeth.3690](https://doi.org/10.1038/nmeth.3690) (cit. on pp. 16, 23, 24, 29, 77).
- [J3] Gustavo de Medeiros, Bálint Balázs, and Lars Hufnagel. “Light-sheet imaging of mammalian development”. *Seminars in Cell & Developmental Biology. Mammalian development* 55 (July 2016), pp. 148–155. DOI: [10.1016/j.semcdb.2015.11.001](https://doi.org/10.1016/j.semcdb.2015.11.001) (cit. on pp. 16, 77).
- [J4] Balint Balazs, Joran Deschamps, Marvin Albert, Jonas Ries, and Lars Hufnagel. “A real-time compression library for microscopy images”. *bioRxiv* (July 2017), p. 164624. DOI: [10.1101/164624](https://doi.org/10.1101/164624) (cit. on p. 77).

The author's others publications

- [J5] Zoltán Jakus, Edina Simon, Bálint Balázs, and Attila Mócsai. “Genetic deficiency of Syk protects mice from autoantibody-induced arthritis”. *Arthritis and Rheumatism* 62.7 (July 2010), pp. 1899–1910. DOI: [10.1002/art.27438](https://doi.org/10.1002/art.27438).
- [J6] Balázs Győrffy et al. “RecurrenceOnline: an online analysis tool to determine breast cancer recurrence and hormone receptor status using microarray data”. *Breast Cancer Research and Treatment* (July 2011). DOI: [10.1007/s10549-011-1676-y](https://doi.org/10.1007/s10549-011-1676-y).

References cited in the thesis

- [J7] Weiwei Shi et al. “Combined analysis of gene expression, DNA copy number, and mutation profiling data to display biological process anomalies in individual breast cancers”. *Breast Cancer Research and Treatment* 144.3 (Mar. 2014), pp. 561–568. DOI: 10.1007/s10549-014-2904-z.

The author’s conference presentations

- [C1] Bálint Balázs, Marvin Albert, and Lars Hufnagel. “GPU-based image processing for multiview microscopy data”. *Light Sheet Fluorescence Microscopy International Conference*. Sheffield, UK, Sept. 2016 (cit. on p. 77).
- [C2] Bálint Balázs, Marvin Albert, and Lars Hufnagel. “GPU-based image processing for multi-view microscopy data”. *Focus on Microscopy*. Taipei, Taiwan, Mar. 2016 (cit. on p. 77).
- [C3] Bálint Balázs, Marvin Albert, and Lars Hufnagel. “GPU-based image processing for multi-view microscopy data”. *Focus on Microscopy*. Bordeaux, France, Apr. 2017 (cit. on p. 77).

References cited in the thesis

- [1] Scott F. Gilbert. *Developmental Biology*. 10th. Sinauer Associates, 2013 (cit. on p. 3).
- [2] Alberto Diaspro. *Optical Fluorescence Microscopy: From the Spectral to the Nano Dimension*. 1st ed. Springer-Verlag Berlin Heidelberg, 2011 (cit. on pp. 3, 4).
- [3] Philipp J Keller and Ernst HK Stelzer. “Quantitative in vivo imaging of entire embryos with Digital Scanned Laser Light Sheet Fluorescence Microscopy”. *Current Opinion in Neurobiology* 18.6 (Dec. 2008). review, pp. 624–632. DOI: 10.1016/j.conb.2009.03.008 (cit. on p. 3).
- [4] Jan Huisken and Didier Y. R. Stainier. “Selective plane illumination microscopy techniques in developmental biology”. *Development* 136.12 (June 2009), pp. 1963–1975. DOI: 10.1242/dev.022426 (cit. on pp. 3, 16).
- [5] Michael Weber and Jan Huisken. “Light sheet microscopy for real-time developmental biology”. *Current Opinion in Genetics & Development* 21.5 (2011), pp. 566–572. DOI: 10.1016/j.gde.2011.09.009 (cit. on p. 3).

- [6] Raju Tomer, Khaled Khairy, and Philipp J Keller. “Shedding light on the system: studying embryonic development with light sheet microscopy”. *Current Opinion in Genetics & Development*. Developmental mechanisms, patterning and evolution 21.5 (Oct. 2011). Review from 2011, pp. 558–565. DOI: [10.1016/j.gde.2011.07.003](https://doi.org/10.1016/j.gde.2011.07.003) (cit. on p. 3).
- [7] Hans-Ulrich Dodt et al. “Ultramicroscopy: three-dimensional visualization of neuronal networks in the whole mouse brain”. *Nature Methods* 4.4 (Mar. 2007), pp. 331–336. DOI: [10.1038/nmeth1036](https://doi.org/10.1038/nmeth1036) (cit. on pp. 3, 16, 27).
- [8] Bi-Chang Chen et al. “Lattice light-sheet microscopy: Imaging molecules to embryos at high spatiotemporal resolution”. *Science* 346.6208 (Oct. 2014), p. 1257998. DOI: [10.1126/science.1257998](https://doi.org/10.1126/science.1257998) (cit. on pp. 3, 17).
- [9] P. Philippe Laissue, Rana A. Alghamdi, Pavel Tomancak, Emmanuel G. Reynaud, and Hari Shroff. “Assessing phototoxicity in live fluorescence imaging”. *Nature Methods* 14.7 (July 2017), pp. 657–661. DOI: [10.1038/nmeth.4344](https://doi.org/10.1038/nmeth.4344) (cit. on pp. 3, 4).
- [10] Jeff W. Lichtman and José-Angel Conchello. “Fluorescence microscopy”. *Nature Methods* 2.12 (Dec. 2005), pp. 910–919. DOI: [10.1038/nmeth817](https://doi.org/10.1038/nmeth817) (cit. on p. 4).
- [11] G. G. Stokes. “On the Change of Refrangibility of Light”. *Philosophical Transactions of the Royal Society of London* 142 (Jan. 1852), pp. 463–562. DOI: [10.1098/rstl.1852.0022](https://doi.org/10.1098/rstl.1852.0022) (cit. on p. 4).
- [12] *Spectra Viewer*. Text (cit. on p. 5).
- [13] Robert Bacallao, Morgane Bomsel, Ernst H. K. Stelzer, and Jan De Mey. “Guiding Principles of Specimen Preservation for Confocal Fluorescence Microscopy”. *Handbook of Biological Confocal Microscopy*. DOI: [10.1007/978-1-4615-7133-9_18](https://doi.org/10.1007/978-1-4615-7133-9_18). Springer, Boston, MA, 1990, pp. 197–205 (cit. on p. 5).
- [14] O. Shimomura, F. H. Johnson, and Y. Saiga. “Extraction, purification and properties of aequorin, a bioluminescent protein from the luminous hydromedusan, Aequorea”. *Journal of Cellular and Comparative Physiology* 59 (June 1962). first purification of GFP from jellyfish, pp. 223–239 (cit. on p. 5).
- [15] Douglas C. Prasher, Virginia K. Eckenrode, William W. Ward, Frank G. Prendergast, and Milton J. Cormier. “Primary structure of the Aequorea victoria green-fluorescent protein”. *Gene* 111.2 (Feb. 1992). cloning GFP cDNA, pp. 229–233. DOI: [10.1016/0378-1119\(92\)90691-H](https://doi.org/10.1016/0378-1119(92)90691-H) (cit. on p. 5).

References cited in the thesis

- [16] M. Chalfie, Y. Tu, G. Euskirchen, W. W. Ward, and D. C. Prasher. “Green fluorescent protein as a marker for gene expression”. *Science* 263.5148 (Feb. 1994). GFP in *c. elegans* / nematodes, pp. 802–805. DOI: [10.1126/science.8303295](https://doi.org/10.1126/science.8303295) (cit. on p. 5).
- [17] Adam Amsterdam, Shuo Lin, and Nancy Hopkins. “The *Aequorea victoria* Green Fluorescent Protein Can Be Used as a Reporter in Live Zebrafish Embryos”. *Developmental Biology* 171.1 (Sept. 1995). first GFP zebrafish, pp. 123–129. DOI: [10.1006/dbio.1995.1265](https://doi.org/10.1006/dbio.1995.1265) (cit. on p. 5).
- [18] Masaru Okabe, Masahito Ikawa, Katsuya Kominami, Tomoko Nakanishi, and Yoshitake Nishimune. “‘Green mice’ as a source of ubiquitous green cells”. *FEBS Letters* 407.3 (May 1997). first EGFP mouse, pp. 313–319. DOI: [10.1016/S0014-5793\(97\)00313-X](https://doi.org/10.1016/S0014-5793(97)00313-X) (cit. on p. 5).
- [19] R Heim, D C Prasher, and R Y Tsien. “Wavelength mutations and posttranslational autoxidation of green fluorescent protein.” *Proceedings of the National Academy of Sciences of the United States of America* 91.26 (Dec. 1994), pp. 12501–12504 (cit. on p. 5).
- [20] Roger Heim and Roger Y Tsien. “Engineering green fluorescent protein for improved brightness, longer wavelengths and fluorescence resonance energy transfer”. *Current Biology* 6.2 (Feb. 1996), pp. 178–182. DOI: [10.1016/S0960-9822\(02\)00450-5](https://doi.org/10.1016/S0960-9822(02)00450-5) (cit. on p. 5).
- [21] Brendan P. Cormack, Raphael H. Valdivia, and Stanley Falkow. “FACS-optimized mutants of the green fluorescent protein (GFP)”. *Gene. Flourescent Proteins and Applications* 173.1 (1996), pp. 33–38. DOI: [10.1016/0378-1119\(95\)00685-0](https://doi.org/10.1016/0378-1119(95)00685-0) (cit. on p. 5).
- [22] Robert F. Service. “Three Scientists Bask in Prize’s Fluorescent Glow”. *Science* 322.5900 (Oct. 2008), pp. 361–361. DOI: [10.1126/science.322.5900.361](https://doi.org/10.1126/science.322.5900.361) (cit. on p. 5).
- [23] E. Abbe. “Beiträge zur Theorie des Mikroskops und der mikroskopischen Wahrnehmung”. *Archiv für mikroskopische Anatomie* 9.1 (1873), pp. 413–418. DOI: [10.1007/BF02956173](https://doi.org/10.1007/BF02956173) (cit. on p. 8).
- [24] Max Born and Emil Wolf. *Principles of Optics: Electromagnetic Theory of Propagation, Interference and Diffraction of Light*. Elsevier, June 2013 (cit. on pp. 8, 9).
- [25] C. J. R. Sheppard and H. J. Matthews. “Imaging in high-aperture optical systems”. *JOSA A* 4.8 (Aug. 1987), pp. 1354–1360. DOI: [10.1364/JOSAA.4.001354](https://doi.org/10.1364/JOSAA.4.001354) (cit. on p. 8).

- [26] Lord Rayleigh F.R.S. “XXXI. Investigations in optics, with special reference to the spectroscope”. *Philosophical Magazine* 8.49 (Oct. 1879), pp. 261–274. DOI: 10.1080/14786447908639684 (cit. on p. 9).
- [27] Jim Swoger, Jan Huisken, and Ernst H. K. Stelzer. “Multiple imaging axis microscopy improves resolution for thick-sample applications”. *Optics Letters* 28.18 (Sept. 2003), p. 1654. DOI: 10.1364/OL.28.001654 (cit. on p. 11).
- [28] Jim Swoger, Peter Verveer, Klaus Greger, Jan Huisken, and Ernst H. K. Stelzer. “Multi-view image fusion improves resolution in three-dimensional microscopy”. *Optics Express* 15.13 (2007), p. 8029. DOI: 10.1364/OE.15.008029 (cit. on p. 11).
- [29] Marvin Minsky. “Microscopy apparatus”. US3013467 A. U.S. Classification 356/432, 359/389, 348/79, 250/215; International Classification G02B21/00; Cooperative Classification G02B21/0024, G02B21/002; European Classification G02B21/00M4A, G02B21/00M4. Dec. 1961 (cit. on p. 12).
- [30] Paul Davidovits and M. David Egger. “Scanning Laser Microscope”. *Nature* 223.5208 (Aug. 1969), pp. 831–831. DOI: 10.1038/223831a0 (cit. on p. 12).
- [31] Ernst H.K. Stelzer and Steffen Lindek. “Fundamental reduction of the observation volume in far-field light microscopy by detection orthogonal to the illumination axis: confocal theta microscopy”. *Optics Communications* 111.5–6 (Oct. 1994), pp. 536–547. DOI: 10.1016/0030-4018(94)90533-9 (cit. on p. 13).
- [32] Silvia Aldaz, Luis M. Escudero, and Matthew Freeman. “Live Imaging of Drosophila Imaginal Disc Development”. *Proceedings of the National Academy of Sciences* 107.32 (Aug. 2010), pp. 14217–14222. DOI: 10.1073/pnas.1008623107 (cit. on p. 14).
- [33] Jean-Léon Maître et al. “Asymmetric division of contractile domains couples cell positioning and fate specification”. *Nature* 536.7616 (Aug. 2016), pp. 344–348. DOI: 10.1038/nature18958 (cit. on pp. 14, 22).
- [34] Emmanuel G. Reynaud, Uroš Kržič, Klaus Greger, and Ernst H.K. Stelzer. “Light sheet-based fluorescence microscopy: more dimensions, more photons, and less photodamage”. *HFSP Journal* 2.5 (Oct. 2008), pp. 266–275. DOI: 10.2976/1.2974980 (cit. on p. 14).
- [35] Stelzer. “Contrast, resolution, pixelation, dynamic range and signal-to-noise ratio: fundamental limits to resolution in fluorescence light microscopy”. *Journal of Microscopy* 189.1 (Jan. 1998). This is also the reason why it is sufficient to store the square root of the count rate. That number will contain all the available information., pp. 15–24. DOI: 10.1046/j.1365-2818.1998.00290.x (cit. on p. 14).

References cited in the thesis

- [36] H. Siedentopf and R. Zsigmondy. “Über Sichtbarmachung und Größenbestimmung ultramikroskopischer Teilchen, mit besonderer Anwendung auf Goldrubiingläser”. *Annalen der Physik* 315.1 (1902), pp. 1–39. DOI: 10.1002/andp.19023150102 (cit. on p. 15).
- [37] A H Voie, D H Burns, and F A Spelman. “Orthogonal-plane fluorescence optical sectioning: three-dimensional imaging of macroscopic biological specimens”. *Journal of Microscopy* 170.Pt 3 (June 1993), pp. 229–36. DOI: 8371260 (cit. on p. 15).
- [38] Arne H. Voie and Francis A. Spelman. “Three-dimensional reconstruction of the cochlea from two-dimensional images of optical sections”. *Computerized Medical Imaging and Graphics* 19.5 (Sept. 1995), pp. 377–384. DOI: 10.1016/0895-6111(95)00034-8 (cit. on p. 15).
- [39] Eran Fuchs, Jules S. Jaffe, Richard A. Long, and Farooq Azam. “Thin laser light sheet microscope for microbial oceanography”. *Optics Express* 10.2 (Jan. 2002), pp. 145–154. DOI: 10.1364/OE.10.000145 (cit. on p. 15).
- [40] Jan Huisken, Jim Swoger, Filippo Del Bene, Joachim Wittbrodt, and Ernst H. K Stelzer. “Optical Sectioning Deep Inside Live Embryos by Selective Plane Illumination Microscopy”. *Science* 305.5686 (2004), pp. 1007–1009 (cit. on pp. 16, 17).
- [41] Jérémie Capoulade, Malte Wachsmuth, Lars Hufnagel, and Michael Knop. “Quantitative fluorescence imaging of protein diffusion and interaction in living cells”. *Nature Biotechnology* 29.9 (Sept. 2011), pp. 835–839. DOI: 10.1038/nbt.1928 (cit. on p. 16).
- [42] Yicong Wu et al. “Inverted selective plane illumination microscopy (iSPIM) enables coupled cell identity lineage and neurodevelopmental imaging in *Caenorhabditis elegans*”. *Proceedings of the National Academy of Sciences* 108.43 (Oct. 2011). iSPIM, tracking c. elegnas nuclei, pp. 17708–17713. DOI: 10.1073/pnas.1108494108 (cit. on p. 16).
- [43] Yicong Wu et al. “Spatially isotropic four-dimensional imaging with dual-view plane illumination microscopy”. *Nature Biotechnology* 31.11 (Nov. 2013), pp. 1032–1038. DOI: 10.1038/nbt.2713 (cit. on pp. 16, 29).
- [44] Jan Huisken and Didier Y. R. Stainier. “Even fluorescence excitation by multidirectional selective plane illumination microscopy (mSPIM)”. *Optics Letters* 32.17 (2007), pp. 2608–2610. DOI: 10.1364/OL.32.002608 (cit. on pp. 16, 17, 21).

- [45] Uros Krzic, Stefan Gunther, Timothy E. Saunders, Sebastian J. Streichan, and Lars Hufnagel. “Multiview light-sheet microscope for rapid *in toto* imaging”. *Nature Methods* 9.7 (July 2012). MuVi-SPIM, pp. 730–733. DOI: 10.1038/nmeth.2064 (cit. on pp. 16, 17, 70, 73, 74).
- [46] Raju Tomer, Khaled Khairy, Fernando Amat, and Philipp J. Keller. “Quantitative high-speed imaging of entire developing embryos with simultaneous multiview light-sheet microscopy”. *Nature Methods* 9.7 (July 2012). SimView, pp. 755–763. DOI: 10.1038/nmeth.2062 (cit. on pp. 16, 17).
- [47] Benjamin Schmid et al. “High-speed panoramic light-sheet microscopy reveals global endodermal cell dynamics”. *Nature Communications* 4 (July 2013). zebrafish sphere projection + FEP tube. DOI: 10.1038/ncomms3207 (cit. on pp. 16, 17).
- [48] Raghav K. Chhetri et al. “Whole-animal functional and developmental imaging with isotropic spatial resolution”. *Nature Methods* 12.12 (Dec. 2015), pp. 1171–1178. DOI: 10.1038/nmeth.3632 (cit. on pp. 16, 17).
- [49] Philipp J. Keller, Annette D. Schmidt, Joachim Wittbrodt, and Ernst H. K. Stelzer. “Reconstruction of Zebrafish Early Embryonic Development by Scanned Light Sheet Microscopy”. *Science* 322.5904 (Nov. 2008), pp. 1065–1069. DOI: 10.1126/science.1162493 (cit. on pp. 16, 17, 21).
- [50] Takehiko Ichikawa et al. “Live Imaging of Whole Mouse Embryos during Gastrulation: Migration Analyses of Epiblast and Mesodermal Cells”. *PLoS ONE* 8.7 (July 2013). post implantation, e64506. DOI: 10.1371/journal.pone.0064506 (cit. on pp. 16, 25, 26).
- [51] Ryan S. Udan, Victor G. Piazza, Chih-wei Hsu, Anna-Katerina Hadjantonakis, and Mary E. Dickinson. “Quantitative imaging of cell dynamics in mouse embryos using light-sheet microscopy”. *Development* (Oct. 2014). post implantation, dev.111021. DOI: 10.1242/dev.111021 (cit. on pp. 16, 25).
- [52] Abhishek Kumar et al. “Dual-view plane illumination microscopy for rapid and spatially isotropic imaging”. *Nature Protocols* 9.11 (Nov. 2014). diSPIM, pp. 2555–2573. DOI: 10.1038/nprot.2014.172 (cit. on p. 17).
- [53] Francesca Cella Zanacchi et al. “Live-cell 3D super-resolution imaging in thick biological samples”. *Nature Methods* 8.12 (Dec. 2011), pp. 1047–1049. DOI: 10.1038/nmeth.1744 (cit. on p. 17).
- [54] Mike Friedrich, Qiang Gan, Vladimir Ermolayev, and Gregory S. Harms. “STED-SPIM: Stimulated Emission Depletion Improves Sheet Illumination Microscopy

References cited in the thesis

- Resolution”. *Biophysical Journal* 100.8 (Apr. 2011), pp. L43–L45. DOI: 10.1016/j.bpj.2010.12.3748 (cit. on p. 17).
- [55] Philipp J. Keller et al. “Fast, high-contrast imaging of animal development with scanned light sheet-based structured-illumination microscopy”. *Nature Methods* 7.8 (Aug. 2010). light-sheet structured illumination, pp. 637–642. DOI: 10.1038/nmeth.1476 (cit. on p. 17).
- [56] Bo-Jui Chang, Victor Didier Perez Meza, and Ernst H. K. Stelzer. “csILSFM combines light-sheet fluorescence microscopy and coherent structured illumination for a lateral resolution below 100 nm”. *Proceedings of the National Academy of Sciences* 114.19 (May 2017), pp. 4869–4874. DOI: 10.1073/pnas.1609278114 (cit. on p. 17).
- [57] K. Greger, J. Swoger, and E. H. K. Stelzer. “Basic building units and properties of a fluorescence single plane illumination microscope”. *Review of Scientific Instruments* 78.2 (Feb. 2007), pp. 023705–023705–7. DOI: doi:10.1063/1.2428277 (cit. on p. 18).
- [58] Bahaa E. A. Saleh and Malvin Carl Teich. *Fundamentals of Photonics*. John Wiley & Sons, Mar. 2007 (cit. on p. 19).
- [59] David M. Shotton. “Confocal scanning optical microscopy and its applications for biological specimens”. *Journal of Cell Science* 94.2 (Oct. 1989), pp. 175–206 (cit. on p. 22).
- [60] Ralph Gräf, Jens Rietdorf, and Timo Zimmermann. “Live Cell Spinning Disk Microscopy”. *Microscopy Techniques. Advances in Biochemical Engineering*. DOI: 10.1007/b102210. Springer, Berlin, Heidelberg, 2005, pp. 57–75 (cit. on p. 22).
- [61] James Jonkman and Claire M. Brown. “Any Way You Slice It—A Comparison of Confocal Microscopy Techniques”. *Journal of Biomolecular Techniques : JBT* 26.2 (July 2015), pp. 54–65. DOI: 10.7171/jbt.15-2602-003 (cit. on p. 22).
- [62] G. S. Kino. “Intermediate Optics in Nipkow Disk Microscopes”. *Handbook of Biological Confocal Microscopy*. DOI: 10.1007/978-1-4615-7133-9_10. Springer, Boston, MA, 1990, pp. 105–111 (cit. on p. 22).
- [63] Akihiko Nakano. “Spinning-disk Confocal Microscopy — A Cutting-Edge Tool for Imaging of Membrane Traffic”. *Cell Structure and Function* 27.5 (2002), pp. 349–355. DOI: 10.1247/csf.27.349 (cit. on p. 22).
- [64] Ekaterina Korotkevich et al. “The Apical Domain Is Required and Sufficient for the First Lineage Segregation in the Mouse Embryo”. *Developmental Cell* 40.3 (2017), 235–247.e7. DOI: <http://dx.doi.org/10.1016/j.devcel.2017.01.006> (cit. on p. 22).

- [65] Jean-Léon Maître, Ritsuya Niwayama, Hervé Turlier, François Nédélec, and Takashi Hiiragi. “Pulsatile cell-autonomous contractility drives compaction in the mouse embryo”. *Nature Cell Biology* 17.7 (July 2015), pp. 849–855. DOI: 10.1038/ncb3185 (cit. on p. 22).
- [66] Jens-Erik Dietrich et al. “Venus trap in the mouse embryo reveals distinct molecular dynamics underlying specification of first embryonic lineages”. *EMBO reports* 16.8 (Aug. 2015), pp. 1005–1021. DOI: 10.15252/embr.201540162 (cit. on p. 22).
- [67] Sonja Nowotschin, Anna Ferrer-Vaquer, and Anna-Katerina Hadjantonakis. “Chapter 20 - Imaging Mouse Development with Confocal Time-Lapse Microscopy”. *Methods in Enzymology*. Ed. by Paul M. Wassarman and Philippe M. Soriano. Vol. 476. Guide to Techniques in Mouse Development, Part A: Mice, Embryos, and Cells, 2nd Edition. Academic Press, 2010, pp. 351–377 (cit. on p. 22).
- [68] Lewis Wolpert. *Principles of Development*. OUP Oxford, Jan. 2011 (cit. on p. 22).
- [69] Adam S. Doherty and Richard M. Schultz. “Culture of Preimplantation Mouse Embryos”. *Developmental Biology Protocols*. Methods in Molecular Biology™. DOI: 10.1385/1-59259-685-1:47. Humana Press, 2000, pp. 47–52 (cit. on p. 23).
- [70] Jens-Erik Dietrich and Takashi Hiiragi. “Stochastic patterning in the mouse pre-implantation embryo”. *Development* 134.23 (Dec. 2007), pp. 4219–4231. DOI: 10.1242/dev.003798 (cit. on p. 23).
- [71] W. Denk, J. H. Strickler, and W. W. Webb. “Two-photon laser scanning fluorescence microscopy”. *Science* 248.4951 (Apr. 1990), pp. 73–76. DOI: 10.1126/science.2321027 (cit. on p. 23).
- [72] Jayne M. Squirrell, David L. Wokosin, John G. White, and Barry D. Bavisser. “Long-term two-photon fluorescence imaging of mammalian embryos without compromising viability”. *Nature Biotechnology* 17.8 (Aug. 1999). low damage live-cell imaging with two-photon caser scanning hamster, pp. 763–767. DOI: 10.1038/11698 (cit. on p. 23).
- [73] Katie McDole, Yuan Xiong, Pablo A. Iglesias, and Yixian Zheng. “Lineage mapping the pre-implantation mouse embryo by two-photon microscopy, new insights into the segregation of cell fates”. *Developmental Biology* 355.2 (July 2011), pp. 239–249. DOI: 10.1016/j.ydbio.2011.04.024 (cit. on p. 23).
- [74] Kazuo Yamagata, Rinako Suetsugu, and Teruhiko Wakayama. “Long-Term, Six-Dimensional Live-Cell Imaging for the Mouse Preimplantation Embryo That Does Not Affect Full-Term Development”. *Journal of Reproduction and Development* 55.3 (2009), pp. 343–350. DOI: 10.1262/jrd.20166 (cit. on p. 23).

References cited in the thesis

- [75] Gustavo de Medeiros et al. “Confocal multiview light-sheet microscopy”. *Nature Communications* 6 (Nov. 2015), p. 8881. DOI: 10.1038/ncomms9881 (cit. on pp. 25, 26, 70).
- [76] Laura Panavaite et al. “3D-geec: a method for studying mouse peri-implantation development”. *Mechanisms of Development*. 18th International Congress of Developmental Biology 18-22 June, University Cultural Centre, National University of Singapore 145. Supplement (July 2017), S78–S79. DOI: 10.1016/j.mod.2017.04.189 (cit. on p. 24).
- [77] Yu-Chih Hsu. “In vitro development of individually cultured whole mouse embryos from blastocyst to early somite stage”. *Developmental Biology* 68.2 (Feb. 1979). post-implantation culture, pp. 453–461. DOI: 10.1016/0012-1606(79)90217-3 (cit. on p. 25).
- [78] Fu-Jen Huang, Tsung-Chieh J. Wu, and Meng-Yin Tsai. “Effect of retinoic acid on implantation and post-implantation development of mouse embryos in vitro”. *Human Reproduction* 16.10 (Oct. 2001). post-implantation culture, pp. 2171–2176. DOI: 10.1093/humrep/16.10.2171 (cit. on p. 25).
- [79] Sonja Nowotschin and Anna-Katerina Hadjantonakis. “Cellular dynamics in the early mouse embryo: from axis formation to gastrulation”. *Current Opinion in Genetics & Development*. Developmental mechanisms, patterning and evolution 20.4 (Aug. 2010), pp. 420–427. DOI: 10.1016/j.gde.2010.05.008 (cit. on p. 25).
- [80] Monica D. Garcia, Ryan S. Udan, Anna-Katerina Hadjantonakis, and Mary E. Dickinson. “Live Imaging of Mouse Embryos”. *Cold Spring Harbor Protocols* 2011.4 (Apr. 2011), pdb.top104. DOI: 10.1101/pdb.top104 (cit. on p. 25).
- [81] Alessandro Bria and Giulio Iannello. “TeraStitcher - A tool for fast automatic 3D-stitching of teravoxel-sized microscopy images”. *BMC Bioinformatics* 13 (Nov. 2012), p. 316. DOI: 10.1186/1471-2105-13-316 (cit. on p. 26).
- [82] Gergely Katona et al. “Fast two-photon in vivo imaging with three-dimensional random-access scanning in large tissue volumes”. *Nature Methods* 9.2 (Feb. 2012), pp. 201–208. DOI: 10.1038/nmeth.1851 (cit. on p. 26).
- [83] Hiroshi Hama et al. “Scale: a chemical approach for fluorescence imaging and reconstruction of transparent mouse brain”. *Nature Neuroscience* 14.11 (Nov. 2011), pp. 1481–1488. DOI: 10.1038/nn.2928 (cit. on p. 27).
- [84] Ali Ertürk et al. “Three-dimensional imaging of solvent-cleared organs using 3DISCO”. *Nature Protocols* 7.11 (Nov. 2012), pp. 1983–1995. DOI: 10.1038/nprot.2012.119 (cit. on p. 27).

- [85] Ali Ertürk et al. “Three-dimensional imaging of the unsectioned adult spinal cord to assess axon regeneration and glial responses after injury”. *Nature Medicine* 18.1 (Jan. 2012), pp. 166–171. DOI: [10.1038/nm.2600](https://doi.org/10.1038/nm.2600) (cit. on p. 27).
- [86] Takaaki Kuwajima et al. “ClearT: a detergent- and solvent-free clearing method for neuronal and non-neuronal tissue”. *Development* 140.6 (Mar. 2013), pp. 1364–1368. DOI: [10.1242/dev.091844](https://doi.org/10.1242/dev.091844) (cit. on p. 27).
- [87] Meng-Tsen Ke, Satoshi Fujimoto, and Takeshi Imai. “SeeDB: a simple and morphology-preserving optical clearing agent for neuronal circuit reconstruction”. *Nature Neuroscience* 16.8 (Aug. 2013), pp. 1154–1161. DOI: [10.1038/nn.3447](https://doi.org/10.1038/nn.3447) (cit. on p. 27).
- [88] Kwanghun Chung and Karl Deisseroth. “CLARITY for mapping the nervous system”. *Nature Methods* 10.6 (June 2013), pp. 508–513. DOI: [10.1038/nmeth.2481](https://doi.org/10.1038/nmeth.2481) (cit. on p. 27).
- [89] Raju Tomer, Li Ye, Brian Hsueh, and Karl Deisseroth. “Advanced CLARITY for rapid and high-resolution imaging of intact tissues”. *Nature Protocols* 9.7 (July 2014), pp. 1682–1697. DOI: [10.1038/nprot.2014.123](https://doi.org/10.1038/nprot.2014.123) (cit. on p. 27).
- [90] Etsuo A. Susaki et al. “Whole-Brain Imaging with Single-Cell Resolution Using Chemical Cocktails and Computational Analysis”. *Cell* 157.3 (Apr. 2014), pp. 726–739. DOI: [10.1016/j.cell.2014.03.042](https://doi.org/10.1016/j.cell.2014.03.042) (cit. on p. 27).
- [91] Nicolas Renier et al. “iDISCO: A Simple, Rapid Method to Immunolabel Large Tissue Samples for Volume Imaging”. *Cell* 159.4 (Nov. 2014), pp. 896–910. DOI: [10.1016/j.cell.2014.10.010](https://doi.org/10.1016/j.cell.2014.10.010) (cit. on p. 27).
- [92] Kazuki Tainaka et al. “Whole-Body Imaging with Single-Cell Resolution by Tissue Decolorization”. *Cell* 159.4 (Nov. 2014), pp. 911–924. DOI: [10.1016/j.cell.2014.10.034](https://doi.org/10.1016/j.cell.2014.10.034) (cit. on p. 28).
- [93] Tongcang Li et al. “Axial Plane Optical Microscopy”. *Scientific Reports* 4 (Dec. 2014). DOI: [10.1038/srep07253](https://doi.org/10.1038/srep07253) (cit. on p. 28).
- [94] Matthew B. Bouchard et al. “Swept confocally-aligned planar excitation (SCAPE) microscopy for high-speed volumetric imaging of behaving organisms”. *Nature Photonics* 9.2 (Feb. 2015), pp. 113–119. DOI: [10.1038/nphoton.2014.323](https://doi.org/10.1038/nphoton.2014.323) (cit. on p. 28).
- [95] Bálint Balázs. “Development of a symmetric single-plane illumination microscope”. Master’s Thesis. Hungary: Pázmány Péter Catholic University, 2013 (cit. on pp. 29, 43).

References cited in the thesis

- [96] Gerald Donnert, Christian Eggeling, and Stefan W. Hell. “Major signal increase in fluorescence microscopy through dark-state relaxation”. *Nature Methods* 4.1 (Jan. 2007). peak intensity more important than average, pp. 81–86. DOI: 10.1038/nmeth986 (cit. on p. 29).
- [97] Na Ji, Jeffrey C. Magee, and Eric Betzig. “High-speed, low-photodamage nonlinear imaging using passive pulse splitters”. *Nature Methods* 5.2 (Feb. 2008). TPE, pulse splitter, peak intensity more important than average, pp. 197–202. DOI: 10.1038/nmeth.1175 (cit. on p. 29).
- [98] Sarah Frisken Gibson and Frederick Lanni. “Experimental test of an analytical model of aberration in an oil-immersion objective lens used in three-dimensional light microscopy”. *JOSA A* 9.1 (Jan. 1992), pp. 154–166. DOI: 10.1364/JOSAA.9.000154 (cit. on p. 48).
- [99] Jizhou Li, Feng Xue, and Thierry Blu. “Fast and accurate three-dimensional point spread function computation for fluorescence microscopy”. *JOSA A* 34.6 (June 2017), pp. 1029–1034. DOI: 10.1364/JOSAA.34.001029 (cit. on p. 48).
- [100] Pierre Gönczy. “Towards a molecular architecture of centriole assembly”. *Nature Reviews Molecular Cell Biology* 13 (2012). DOI: 10.1038/nrm3373 (cit. on p. 51).
- [101] Johannes Schindelin et al. “Fiji: an open-source platform for biological-image analysis”. *Nature Methods* 9.7 (July 2012), pp. 676–682. DOI: 10.1038/nmeth.2019 (cit. on pp. 52, 67).
- [102] Stephan Preibisch, Stephan Saalfeld, Johannes Schindelin, and Pavel Tomancak. “Software for bead-based registration of selective plane illumination microscopy data”. *Nature Methods* 7.6 (June 2010), pp. 418–419. DOI: 10.1038/nmeth0610-418 (cit. on p. 52).
- [103] Stephan Preibisch et al. “Efficient Bayesian-based multiview deconvolution”. *Nature Methods* 11.6 (June 2014), pp. 645–648. DOI: 10.1038/nmeth.2929 (cit. on p. 52).
- [104] H. Kirshner, D. Sage, and M. Unser. “3D PSF Models for Fluorescence Microscopy in ImageJ”. *Proceedings of the Twelfth International Conference on Methods and Applications of Fluorescence Spectroscopy, Imaging and Probes (MAF’11)*. ImageJ PSF generator. Strasbourg, French Republic, Sept. 2011, p. 154 (cit. on p. 52).
- [105] Uroš Kržič. “Multiple-view microscopy with light-sheet based fluorescence microscope”. PhD thesis. Germany: Ruperto-Carola University of Heidelberg, 2009 (cit. on p. 56).

- [106] M. Temerinac-Ott et al. “Multiview Deblurring for 3-D Images from Light-Sheet-Based Fluorescence Microscopy”. *IEEE Transactions on Image Processing* 21.4 (Apr. 2012), pp. 1863–1873. DOI: 10.1109/TIP.2011.2181528 (cit. on p. 56).
- [107] M. Temerinac-Ott, O. Ronneberger, R. Nitschke, W. Driever, and H. Burkhardt. “Spatially-variant Lucy-Richardson deconvolution for multiview fusion of microscopical 3D images”. *2011 IEEE International Symposium on Biomedical Imaging: From Nano to Macro*. Mar. 2011, pp. 899–904. DOI: 10.1109/ISBI.2011.5872549 (cit. on p. 56).
- [108] Khalid Sayood. *Introduction to Data Compression, Fourth Edition*. 4th ed. The Morgan Kaufmann Series in Multimedia Information and Systems. Morgan Kaufmann, 2012 (cit. on pp. 56, 67).
- [109] Claude E. Shannon. “A mathematical theory of communication”. *The Bell System Technical Journal* 27.4 (Oct. 1948), pp. 623–656. DOI: 10.1002/j.1538-7305.1948.tb00917.x (cit. on p. 57).
- [110] Claude E. Shannon. “A mathematical theory of communication”. *The Bell System Technical Journal* 27.3 (July 1948), pp. 379–423. DOI: 10.1002/j.1538-7305.1948.tb01338.x (cit. on p. 57).
- [111] David A. Huffman. “A Method for the Construction of Minimum-Redundancy Codes”. *Proceedings of the IRE* 40.9 (Sept. 1952), pp. 1098–1101. DOI: 10.1109/JRPROC.1952.273898 (cit. on p. 57).
- [112] N. Ahmed, T. Natarajan, and K. R. Rao. “Discrete Cosine Transform”. *IEEE Transactions on Computers* C-23.1 (Jan. 1974), pp. 90–93. DOI: 10.1109/T-C.1974.223784 (cit. on p. 62).
- [113] Stephane G. Mallat. “A theory for multiresolution signal decomposition : the wavelet representation”. *IEEE Transaction on Pattern Analysis and Machine Intelligence* (1989) (cit. on p. 64).
- [114] William B. Pennebaker and Joan L. Mitchell. *JPEG: Still Image Data Compression Standard*. Springer Science & Business Media, Dec. 1992 (cit. on p. 65).
- [115] M.J. Weinberger, G. Seroussi, and G. Sapiro. “The LOCO-I lossless image compression algorithm: principles and standardization into JPEG-LS”. *IEEE Transactions on Image Processing* 9.8 (Aug. 2000), pp. 1309–1324. DOI: 10.1109/83.855427 (cit. on p. 65).
- [116] Michael D. Adams. *The JPEG-2000 still image compression standard*. 2001 (cit. on p. 65).

References cited in the thesis

- [117] John Nickolls, Ian Buck, Michael Garland, and Kevin Skadron. “Scalable Parallel Programming with CUDA”. *Queue* 6.2 (Mar. 2008), pp. 40–53. DOI: [10.1145/1365490.1365500](https://doi.org/10.1145/1365490.1365500) (cit. on p. 67).
- [118] Anne E. Carpenter and David M. Sabatini. “Systematic genome-wide screens of gene function”. *Nature Reviews Genetics* 5.1 (Jan. 2004), pp. 11–22. DOI: [10.1038/nrg1248](https://doi.org/10.1038/nrg1248) (cit. on p. 67).
- [119] Christophe J. Echeverri and Norbert Perrimon. “High-throughput RNAi screening in cultured cells: a user’s guide”. *Nature Reviews Genetics* 7.5 (May 2006), pp. 373–384. DOI: [10.1038/nrg1836](https://doi.org/10.1038/nrg1836) (cit. on p. 67).
- [120] Rainer Pepperkok and Jan Ellenberg. “High-throughput fluorescence microscopy for systems biology”. *Nature Reviews Molecular Cell Biology* 7.9 (Sept. 2006), pp. 690–696. DOI: [10.1038/nrm1979](https://doi.org/10.1038/nrm1979) (cit. on p. 67).
- [121] Eric Betzig et al. “Imaging Intracellular Fluorescent Proteins at Nanometer Resolution”. *Science* 313.5793 (Sept. 2006), pp. 1642–1645. DOI: [10.1126/science.1127344](https://doi.org/10.1126/science.1127344) (cit. on p. 67).
- [122] Samuel T. Hess, Thanan P. K. Girirajan, and Michael D. Mason. “Ultra-High Resolution Imaging by Fluorescence Photoactivation Localization Microscopy”. *Biophysical Journal* 91.11 (Dec. 2006), pp. 4258–4272. DOI: [10.1529/biophysj.106.091116](https://doi.org/10.1529/biophysj.106.091116) (cit. on p. 67).
- [123] Michael J. Rust, Mark Bates, and Xiaowei Zhuang. “Sub-diffraction-limit imaging by stochastic optical reconstruction microscopy (STORM)”. *Nature Methods* 3.10 (Oct. 2006), pp. 793–796. DOI: [10.1038/nmeth929](https://doi.org/10.1038/nmeth929) (cit. on p. 67).
- [124] Roy Wollman and Nico Stuurman. “High throughput microscopy: from raw images to discoveries”. *Journal of Cell Science* 120.21 (Nov. 2007), pp. 3715–3722. DOI: [10.1242/jcs.013623](https://doi.org/10.1242/jcs.013623) (cit. on p. 67).
- [125] Emmanuel G. Reynaud, Jan Peychl, Jan Huisken, and Pavel Tomancak. “Guide to light-sheet microscopy for adventurous biologists”. *Nature Methods* 12.1 (Jan. 2015), pp. 30–34. DOI: [10.1038/nmeth.3222](https://doi.org/10.1038/nmeth.3222) (cit. on p. 67).
- [126] Jeffrey M. Perkel. “The struggle with image glut”. *Nature* 533.7601 (Apr. 2016), pp. 131–132. DOI: [10.1038/533131a](https://doi.org/10.1038/533131a) (cit. on p. 67).
- [127] Douglas W. Cromeley. “Digital Images Are Data: And Should Be Treated as Such”. *Methods in molecular biology (Clifton, N.J.)* 931 (2013), pp. 1–27. DOI: [10.1007/978-1-62703-056-4_1](https://doi.org/10.1007/978-1-62703-056-4_1) (cit. on p. 67).
- [128] Fernando Amat et al. “Efficient processing and analysis of large-scale light-sheet microscopy data”. *Nature Protocols* 10.11 (Nov. 2015), pp. 1679–1696. DOI: [10.1038/nprot.2015.111](https://doi.org/10.1038/nprot.2015.111) (cit. on p. 67).

- [129] Tobias Pietzsch, Stephan Saalfeld, Stephan Preibisch, and Pavel Tomancak. “Big-DataViewer: visualization and processing for large image data sets”. *Nature Methods* 12.6 (June 2015), pp. 481–483. DOI: [10.1038/nmeth.3392](https://doi.org/10.1038/nmeth.3392) (cit. on p. 67).
- [130] Z. Wang, M. Klaiber, Y. Gera, S. Simon, and T. Richter. “Fast lossless image compression with 2D Golomb parameter adaptation based on JPEG-LS”. *Signal Processing Conference (EUSIPCO), 2012 Proceedings of the 20th European*. Aug. 2012, pp. 1920–1924 (cit. on p. 67).
- [131] Roman Starosolski. “Simple fast and adaptive lossless image compression algorithm”. *Software: Practice and Experience* 37.1 (Jan. 2007), pp. 65–91. DOI: [10.1002/spe.746](https://doi.org/10.1002/spe.746) (cit. on p. 67).
- [132] P. G. Howard and J. S. Vitter. “Fast and efficient lossless image compression”. *[Proceedings] DCC ‘93: Data Compression Conference*. 1993, pp. 351–360. DOI: [10.1109/DCC.1993.253114](https://doi.org/10.1109/DCC.1993.253114) (cit. on p. 67).
- [133] Marc Treib, Florian Reichl, Stefan Auer, and Rüdiger Westermann. “Interactive Editing of GigaSample Terrain Fields”. *Computer Graphics Forum* 31.2pt2 (May 2012), pp. 383–392. DOI: [10.1111/j.1467-8659.2012.03017.x](https://doi.org/10.1111/j.1467-8659.2012.03017.x) (cit. on p. 67).
- [134] M. Treib et al. “Turbulence Visualization at the Terascale on Desktop PCs”. *IEEE Transactions on Visualization and Computer Graphics* 18.12 (Dec. 2012), pp. 2169–2177. DOI: [10.1109/TVCG.2012.274](https://doi.org/10.1109/TVCG.2012.274) (cit. on p. 67).
- [135] Robert A. Gowen and Alan Smith. “Square root data compression”. *Review of Scientific Instruments* 74.8 (Aug. 2003), pp. 3853–3861. DOI: [10.1063/1.1593811](https://doi.org/10.1063/1.1593811) (cit. on p. 67).
- [136] Gary M. Bernstein et al. “Noise and bias in square-root compression schemes”. *Publications of the Astronomical Society of the Pacific* 122.889 (Mar. 2010). arXiv: 0910.4571, pp. 336–346. DOI: [10.1086/651281](https://doi.org/10.1086/651281) (cit. on p. 67).
- [137] R. M. Gray and D. L. Neuhoff. “Quantization”. *IEEE Transactions on Information Theory* 44.6 (Oct. 1998), pp. 2325–2383. DOI: [10.1109/18.720541](https://doi.org/10.1109/18.720541) (cit. on p. 67).
- [138] F. J. Anscombe. “The Transformation of Poisson, Binomial and Negative-Binomial Data”. *Biometrika* 35.3-4 (Dec. 1948), pp. 246–254. DOI: [10.1093/biomet/35.3-4.246](https://doi.org/10.1093/biomet/35.3-4.246) (cit. on p. 67).
- [139] M. Makitalo and A. Foi. “Optimal Inversion of the Anscombe Transformation in Low-Count Poisson Image Denoising”. *IEEE Transactions on Image Processing* 20.1 (Jan. 2011), pp. 99–109. DOI: [10.1109/TIP.2010.2056693](https://doi.org/10.1109/TIP.2010.2056693) (cit. on p. 67).

References cited in the thesis

- [140] M. Makitalo and A. Foi. “A Closed-Form Approximation of the Exact Unbiased Inverse of the Anscombe Variance-Stabilizing Transformation”. *IEEE Transactions on Image Processing* 20.9 (Sept. 2011), pp. 2697–2698. DOI: [10.1109/TIP.2011.2121085](https://doi.org/10.1109/TIP.2011.2121085) (cit. on p. 67).
- [141] M. Makitalo and A. Foi. “Optimal Inversion of the Generalized Anscombe Transformation for Poisson-Gaussian Noise”. *IEEE Transactions on Image Processing* 22.1 (Jan. 2013), pp. 91–103. DOI: [10.1109/TIP.2012.2202675](https://doi.org/10.1109/TIP.2012.2202675) (cit. on p. 67).
- [142] C. Sommer, C. Straehle, U. Köthe, and F. A. Hamprecht. “Ilastik: Interactive learning and segmentation toolkit”. *2011 IEEE International Symposium on Biomedical Imaging: From Nano to Macro*. Mar. 2011, pp. 230–233. DOI: [10.1109/ISBI.2011.5872394](https://doi.org/10.1109/ISBI.2011.5872394) (cit. on p. 70).
- [143] Thorvald Julius Sørensen. *A method of establishing groups of equal amplitude in plant sociology based on similarity of species content and its application to analyses of the vegetation on Danish commons*. København: I kommission hos E. Munksgaard, 1948 (cit. on p. 70).
- [144] Lee R. Dice. “Measures of the Amount of Ecologic Association Between Species”. *Ecology* 26.3 (July 1945), pp. 297–302. DOI: [10.2307/1932409](https://doi.org/10.2307/1932409) (cit. on p. 70).
- [145] Romain Fernandez et al. “Imaging plant growth in 4D: robust tissue reconstruction and lineaging at cell resolution”. *Nature Methods* 7.7 (July 2010), pp. 547–553. DOI: [10.1038/nmeth.1472](https://doi.org/10.1038/nmeth.1472) (cit. on p. 75).
- [146] Joran Deschamps, Markus Mund, and Jonas Ries. “3D superresolution microscopy by supercritical angle detection”. *Optics Express* 22.23 (Nov. 2014), pp. 29081–29091 (cit. on p. 75).
- [147] Mike Heilemann et al. “Subdiffraction-Resolution Fluorescence Imaging with Conventional Fluorescent Probes”. *Angewandte Chemie International Edition* 47.33 (Aug. 2008), pp. 6172–6176. DOI: [10.1002/anie.200802376](https://doi.org/10.1002/anie.200802376) (cit. on p. 75).
- [148] Joran Deschamps, Andreas Rowald, and Jonas Ries. “Efficient homogeneous illumination and optical sectioning for quantitative single-molecule localization microscopy”. *Optics Express* 24.24 (Nov. 2016), pp. 28080–28090. DOI: [10.1364/OE.24.028080](https://doi.org/10.1364/OE.24.028080) (cit. on p. 75).
- [149] I. Izeddin et al. “Wavelet analysis for single molecule localization microscopy”. *Optics Express* 20.3 (Jan. 2012), pp. 2081–2095 (cit. on p. 76).
- [150] Carlas S. Smith, Nikolai Joseph, Bernd Rieger, and Keith A. Lidke. “Fast, single-molecule localization that achieves theoretically minimum uncertainty”. *Nature Methods* 7.5 (May 2010), pp. 373–375. DOI: [10.1038/nmeth.1449](https://doi.org/10.1038/nmeth.1449) (cit. on p. 76).

-
- [151] Jeremy C. Simpson et al. “Genome-wide RNAi screening identifies human proteins with a regulatory function in the early secretory pathway”. *Nature Cell Biology* 14.7 (July 2012), pp. 764–774. DOI: 10.1038/ncb2510 (cit. on p. 85).